

# **Spatially detailed analysis of drill core samples with Laser-Induced Breakdown Spectroscopy: Detection, classification, and quantification of rare earth elements and lithium**

Von der Naturwissenschaftlichen Fakultät der  
Gottfried Wilhelm Leibniz Universität Hannover

zur Erlangung des Grades  
Doktor der Naturwissenschaften (Dr. rer. nat.)

genehmigte Dissertation  
von  
Simon Arne Müller, M.Sc.

2023

**Referent:** Prof. Dr. rer. nat. Francois Holtz

**Korreferent:** Prof. Dr. rer. nat. Torsten Graupner

**Tag der Promotion:** 23.05.2023

## Acknowledgements

This thesis would not exist without the support of many different people. At first, I would like to thank my supervisors Jeannet Meima and Francois Holtz. Without Jeannets excessive support and inspiration, I would not have thought about pursuing a PhD in the first place. She ignited my interest in the LIBS technology and gave me the freedom to investigate the wide variety of different geological data sets based on my own ideas. Furthermore, she always had an open door for questions and significantly improved my scientific thinking and writing with her persistent help during the creation of all three publications. I am very grateful for Francois uncomplicated and friendly nature, as well as his interest in new technologies and methods, without which this PhD project would not have been possible.

Furthermore, I thank Dieter Rammlmair for his creativity and visionary ideas, which were very inspiring. He always supported new and unconventional ideas of everyone in the working group. I also want to thank Dominic Goericke, who accompanied every measurement campaign with his presence and his technological knowledge of the instruments. His relaxed nature helped a lot during stressful times. I thank Hans-Eike Gäbler for the LA-ICP-TOFMS measurements and his insights into the instruments underlying technique. He put a lot of effort into the third publication and supported its creation with new ideas and fruitful discussions. I thank Christian Wöhrl and Simon Goldmann for the microprobe measurements and Martin Schodlok for the discussions on REE distributions in the investigated Storkwitz samples. Additionally, I am very grateful for all people who were, and still are part of my old working group at BGR. Especially Khulan Berkh, Wilhelm Nikonow, Marko Hornschuh, Marleen Künker, Guillaume Jacque, Sören Henning and Torsten Graupner enlightened my working hours, and the daily lunchbreaks as well as the interesting discussions created an atmosphere that I remember with pleasure.

Several external partners also influenced this PhD project greatly. I want to thank all former and current staff members of LTB Berlin, who were involved in building and maintaining the drill core scanner used. I especially thank David Mory, Sven Merk, Lutz Pfeifer, Dominik Schiller and Tino Seger, who quickly fixed any problems with the LIBS system or supported my measurements in their own laboratories. I thank the whole T-REX consortium for the frequent discussions and the pleasant atmosphere during the project. Furthermore, I want to thank Dr. Lapp and the Geological Survey of Saxony (LfULG) for providing a wide variety of drill cores for the GeoLIBScanner project, as well as Pentii Grönholm and Keliber Oy, who provided the drill core samples for the T-REX project.

Finally, I want to thank my friends and family for their support, as well as the wonderful times after work. I am especially grateful for my flatmates in Berlin, without whom the COVID-19 pandemic and the related lockdowns would have been increasingly more difficult to endure. I sincerely thank my parents, who always supported me financially and mentally. They never questioned any of my educational choices and encouraged me to pursue a career solely based on my own interests. I thank Veronika for her support, her time, and the wonderful years up to now. She had to live through stressful afternoons and faced all discussions about algorithms, spectra and rocks with endless patience and sincere interest.

## Abstract

In the transformation towards climate neutral consumption, electric alternatives rise in favour of fossil energy sources in a variety of different fields. Lithium and several elements from the group of Rare Earth Elements (REEs) are of particular importance for modern battery production and the supply of green energy, and therefore play a crucial role for this transformation. Their demand has increased constantly over the last years and an ongoing trend is expected for the future. New instruments and analytical methods for the geochemical investigation of drill cores can support mineral exploration and active mining and thereby help to cope with the growing demand.

Laser-Induced Breakdown Spectroscopy (LIBS) is an analytical technique with many advantages for the analysis of drill core material. It has a high measurement speed, no sample preparation is needed, and major, minor as well as trace elements can be detected in a single spectrum under atmospheric conditions. Nevertheless, physical and chemical matrix effects prevent a straightforward analysis of heterogeneous material, which is especially relevant for spatially resolved investigations of drill core samples. This work displays novel methods that enable the analysis of LIBS mappings of large REE- and Li-bearing drill core samples by overcoming the problematic matrix effects with different un- semi- and supervised machine learning algorithms.

In the first application, drill core samples of brecciated carbonatites were spatially investigated with LIBS to establish an intensity limit for La using the k-means clustering algorithm. Based on this intensity limit, REE enrichments were detected in the investigated sample. Afterwards, the REE content of the sample was estimated with mass balance calculations.

For the second application, different Li-bearing drill core samples were mapped in high resolution with LIBS and a new classification model was developed. It combines Linear Discriminant Analysis (LDA) and One-Class Support Vector Machines (OC-SVM) to enable the classification of minerals that were covered by a train set, while also identifying LIBS matrices that are unknown to the model.

The third application combined Laser Ablation – Inductively Coupled Plasma – Time of Flight Mass Spectrometry (LA-ICP-TOFMS) with LIBS measurements of the same sample. After image registration, this reference sample was used to create a Least-Square Support Vector Machine (LS-SVM) quantification model, which can be employed to convert LIBS intensities of similar material into element concentrations. The model allows a pixel-specific, spatially resolved quantification of multiple minerals with a single model.

Each application displays possible solutions to minimize the influence of physical and chemical matrix effects on the spatial analysis of LIBS mappings of large drill core samples, which enables different kinds of analysis. Thereby, the great potential but also the challenges of LIBS as an analytical tool in geology and mining are highlighted.

**Keywords:** laser-induced breakdown spectroscopy, drill core scanner, machine learning, spodumene pegmatite, storkwitz carbonatite



## Zusammenfassung

Durch die Transformation zu klimaneutralem Konsum gewinnen elektrische Alternativen gegenüber fossilen Energiequellen an immer größerer Bedeutung in einer Vielzahl verschiedener Bereiche. Lithium und diverse Elemente der seltenen Erden (REEs) spielen eine besonders wichtige Rolle in der Produktion moderner Batterien und der Herstellung grüner Energie, weshalb sie für diese Transformation unabdingbar sind. Entsprechend ist ihre Nachfrage in den vergangenen Jahren konstant gestiegen und ein gleichbleibender Trend wird auch für die Zukunft erwartet. Neue Instrumente und Methoden können die geochemische Untersuchung von Bohrkernen während der Exploration und des Abbaus unterstützen und so dabei helfen, den wachsenden Bedarf zu decken.

Laserinduzierte Plasmaspektroskopie (LIBS) ist eine analytische Methode, die für die Untersuchung von Bohrkernmaterial viele Vorteile bietet. Es ist keine Probenvorbereitung erforderlich und Haupt-, Neben- und Spurenelemente können in einem einzigen Spektrum mit hoher Messgeschwindigkeit unter atmosphärischen Bedingungen nachgewiesen werden. Nichtsdestotrotz ist die Untersuchung von komplexem Material mit LIBS herausfordernd, da verschiedene physische und chemische Matrixeffekte eine unkomplizierte Auswertung erschweren. Dies ist besonders bei der räumlich aufgelösten Analyse von heterogenen Bohrkernen relevant. In dieser Arbeit werden neu entwickelte Methoden präsentiert, die den Einsatz von LIBS zur räumlich hochaufgelösten Untersuchung von großen REE- und Li-haltigen Bohrkernproben ermöglichen. Dabei wurden verschiedene unüberwachte, semi-überwachte und überwachte Algorithmen des maschinellen Lernens verwendet, um die problematischen Matrixeffekte zu überwinden.

In der ersten Anwendung wurden brekziierte Karbonatit-Bohrkerne flächendeckend mit LIBS analysiert, um Intensitätsgrenzen für La mit Hilfe des k-means Clusteralgorithmus zu bestimmen. Mit Hilfe dieser Intensitätsgrenze konnten REE-Anreicherungen erkannt werden, bevor darauf aufbauend die REE-Gehalte der Probe mit Hilfe von Massenbilanzierung berechnet wurden.

Für die zweite Anwendung wurden mehrere Li-haltige Bohrkernproben in hoher räumlicher Auflösung mit LIBS gemessen. Anschließend wurde ein neues Klassifizierungsmodell entwickelt, das auf einer Kombination von Linear Discriminant Analysis (LDA) und One-Class Support Vector Machines (OC-SVM) beruht. Das Modell erlaubt sowohl die Klassifizierung der vom Trainingsdatensatz abgebildeten Minerale als auch die Identifikation unbekannter LIBS-Matrix, die nicht durch das Modell abgedeckt sind.

In einer dritten Anwendung wurden Laser Ablation – Inductively Coupled Plasma – Time of Flight Mass Spectrometry (LA-ICP-TOFMS) Messungen und LIBS-Messungen derselben Gesteinsprobe kombiniert. Auf Basis dieser Referenzprobe wurde ein Least-Square Support Vector Machines (LS-SVM) Quantifizierungsmodell erstellt, mit dessen Hilfe die LIBS-Intensitäten ähnlichen Materials in Elementkonzentrationen umgewandelt werden können. Dadurch ermöglicht das Modell eine ortsaufgelöste, pixelgenaue Quantifizierung mehrerer Minerale mit einem einzigen Modell.

Jede Anwendung zeigt dabei Lösungen, um den Einfluss physischer und chemischer Matrixeffekte in räumlich hochaufgelösten LIBS Mappings zu minimieren und so verschiedene Arten der Auswertung zu ermöglichen. Dabei werden das große Potential aber auch die bestehenden Herausforderungen der LIBS-Technologie als Analysetool in der Geologie und der Bergbauindustrie verdeutlicht.

**Schlagwörter:** Laserinduzierte Plasmaspektroskopie, Bohrkernscanner, maschinelles Lernen, Spodumen Pegmatit, Storkwitz Karbonatit

# Table of Contents

<b>i. Acknowledgements</b> .....	i
<b>ii. Abstract</b> .....	ii
<b>ii. Zusammenfassung</b> .....	ii
<b>iii. List of Abbreviations</b> .....	iii
<b>1. Introduction and Background</b> .....	7
1.1 The importance of Rare Earth Elements and Lithium – LIBS as a promising technique for their spatial detection in drill core samples.....	7
1.2 Laser-Induced Breakdown Spectroscopy (LIBS) – fundamentals and history.....	8
1.3 LIBS in geology, from point measurements to imaging analysis.....	11
1.4 State-of-the-art for LIBS-based analysis of REEs and Li.....	11
1.5 Challenges of spatial LIBS analysis and new contributions of this work.....	12
1.6 LIBS instrumentation used in this work.....	13
1.7 Reference measurements.....	14
1.7.1 Electron microprobe.....	14
1.7.2 Laser ablation-inductively coupled plasma-time of flight mass spectrometer (LA-ICP-TOFMS) .....	15
1.7.3 Energy dispersive X-ray fluorescence ( $\mu$ -EDXRF).....	15
<b>2. Detecting REE-rich areas in heterogeneous drill cores from Storkwitz using LIBS and a combination of k-means clustering and spatial raster analysis</b> .....	22
<b>3. Mineral classification of lithium-bearing pegmatites based on laser-induced breakdown spectroscopy: Application of semi-supervised learning to detect known minerals and unknown material</b> .....	39
<b>4. Improving spatially-resolved Lithium quantification in drill core samples of spodumene pegmatite by using laser-induced breakdown spectroscopy and pixel-matched reference samples</b> .....	55
<b>5. Summary and Outlook</b> .....	75
5.1 Developed applications and their combination.....	75
5.2 Instrument specific challenges.....	76
5.3 Software and algorithm specific challenges.....	77
5.4 Future potential of LIBS for geological applications.....	77

## Curriculum Vitae

## Publications

## List of Abbreviations

---

<b>Abbreviation</b>	<b>Definition</b>
BGR	Federal Institute for Geosciences and Natural Resources
BSE	back scattered electron
CCD	charge-coupled device
CF-LIBS	calibration free-laser-induced breakdown spectroscopy
CM	calibration material
cps	counts per second
ICPMS	inductively coupled plasma mass spectrometry
LA-ICP-TOFMS	laser ablation-inductively coupled plasma-time of flight mass spectrometry
LDA	linear discriminant analysis
LIBS	laser-induced breakdown spectroscopy
LOD	limit of detection
LS-SVM	least square-support vector machines
LTB	Lasertechnik Berlin
$\mu$ -EDXRF	energy dispersive X-ray fluorescence
OC-SVM	one class-support vector machines
PCA	principal component analysis
PLSR	partial least square regression
REEs	rare earth elements
RMSE	root mean square error
ROI	region of interest
SAM	spectral angle mapper
SVD	singular value decomposition
XRF	X-ray fluorescence

# 1. Introduction and Background

## 1.1 The importance of Rare Earth Elements and Lithium – LIBS as a promising technique for their spatial detection in drill core samples

Modern climate change is a critical thread for us and future generations. In the “Paris Agreement,” 2015, 196 nations signed a legally binding international treaty on climate change with the goal to keep global warming below 2 °C. Thereto, most states, their industry sectors as well as their inhabitants must reduce their greenhouse gas emissions until 2030, and an increasing number of countries are claiming progress towards carbon free consumption. Several high-emitting sectors started the transformation process towards net-zero emissions until 2050 (World Economic Forum, 2022), and in this context, the mobility sector is focusing on its electrification as well. To continue with this trend, specific elements are crucial. Especially Li and the so-called Rare Earth Elements (REEs) are urgently needed for this transformation. Numerous publications assess their future demand. They all agree that, despite a growing interest in recycling, active mining and ongoing exploration campaigns will be needed to fully cover the consumption of REEs and Li in the future (for REEs: e.g. Ganguli and Cook, 2018; Goodenough et al., 2018; Charalampides et al., 2015; for Li: e.g. Kushnir and Sandén, 2012; Martin et al., 2017; Maxwell, 2014; Xu et al., 2020).

In most geological definitions, REEs cover the elements Y as well as the lanthanides (La, Ce, Pr, Nd, Sm, Eu, Gd, Tb, Dy, Ho, Er, Tm, Yb and Lu). The lanthanides from La to Eu are conventionally termed light REEs (LREE), whereas the remaining lanthanides and Y are called heavy REEs (HREE). Variations in this classification exist, since some authors define an additional class of mid REEs (MREE) or label Eu as heavy (Chakhmouradian and Wall, 2012; Hatch, 2012). Due to their characteristic properties, REEs are used in modern technology for various products (Charalampides et al., 2015), predominantly for magnets and catalysts (Goodenough et al., 2018). Electric vehicles and wind turbines heavily rely on REE magnets, making them crucial for climate neutral locomotion and the production of green electricity. Especially Ce, Nd and La are of high interest for a variety of applications (Alonso et al., 2012; Christmann, 2014), and, as a result, their demand is expected to grow in the next decades (Alonso et al., 2012). Contrary to the demand, only few countries operate feasible REE mining (Ganguli and Cook, 2018) and high supply risks are presented. Therefore, the European Commission has classified REEs as a critical material for the European Union (Romppanen et al., 2017).

Although REEs are relatively abundant in the Earth’s crust, their concentration often not exceeds the feasibility limits for mining (Balaram, 2019). The existing deposits are divided into primary deposits connected to magmatic, hydrothermal and/or metamorphic processes, and secondary deposits formed by weathering and erosion. Primary REE deposits are often bound to carbonatites, which include many of the most important REE-bearing minerals (Balaram, 2019). Despite the vast number of Rare Earth Minerals found in primary deposits, only few can be processed to yield a marketable product (Chakhmouradian and Wall, 2012). REEs are often considered green elements due to their importance for energy transition, but mining and processing propose environmental problems. Chemicals used to leech the elements are often toxic, and by-products can be radioactive due to potential Th and U abundances in the same ore (Balaram, 2019; Schulz et al., 2017).

Lithium is also crucial for a wide variety of modern products. Most importantly, Li is needed for lithium-ion batteries, which, up to today, are irreplaceable for electric vehicles and other electronic gadgets of today’s society (Scrosati and Garche, 2010). Especially the former led to an increasing Li consumption

in the last years, and although the prediction of its future demand is difficult and forecasts from different years expect varying growths in production and consumption, no publication expects a reversing trend in the future (e.g. Kushnir and Sandén, 2012; Sonoc and Jeswiet, 2014; Greim et al., 2020; Xu et al., 2020).

First companies investigate the possible extraction of Li as a by-product of geothermal energy (Goldberg et al., 2022) and an increasing effort is put into the recycling of lithium-ion batteries (Gaines et al., 2018; Wu et al., 2022). Nevertheless, most of today's Li is mined from two primary geological sources, evaporative brines and pegmatites, and corresponding deposits are found in various countries (Kesler et al., 2012). The Li-bearing pegmatites are mostly granitic and often incorporate a variety of economically interesting metals, including REEs. Spodumene is the most important Li-bearing mineral in pegmatites, although petalite, eucryptite and lepidolite rarely occur as well (Kesler et al., 2012).

During exploration and mining, extensive drilling campaigns are necessary to detect the relevant areas that show element enrichments. Thereby, spatial analysis of drill core samples could offer crucial information on elemental distributions and a wide variety of machine learning models could be employed to extract additional information like mineral assemblages or element concentrations. This could enhance the precision in mining, support a targeted processing, and, thus, reduce cost, emission, and the ecological impact.

Different analytical techniques allow the spatial analysis of geological samples, but their reliable use in exploration and mining requires further research.

So far, hyperspectral imaging, energy dispersive X-ray fluorescence ( $\mu$ -EDXRF), Raman, laser ablation-inductively coupled plasma-time of flight mass spectrometry (LA-ICP-TOFMS) and laser-induced breakdown spectroscopy (LIBS) are already used to spatially analyse rocks and ore with different resolutions (e.g. Berkh and Rammlmair, 2022; Booysen et al., 2022; Chew et al., 2021; Neff et al., 2020; Nikonow et al., 2019). Every technique offers specific (dis-)advantages, and for the profitable use of spatially resolved analysis of REE- and Li-bearing drill core samples, important requirements are only met by few analytical techniques. LIBS shows several advantages for drill core measurements and allows a detailed spatial analysis of large samples or complete drill core meters (e.g. Kuhn et al., 2016; Meima et al., 2022; Rifai et al., 2020). It is therefore especially promising for mining and exploration (e.g. Kuhn and Meima, 2019; Rifai et al., 2018). As an emerging analytical technique in the field of geology, further research is needed to promote its use.

### 1.2 Laser-Induced Breakdown Spectroscopy (LIBS) – fundamentals and history

LIBS is an analytical technique that uses laser-generated plasma to vaporize, atomize and excite the investigated samples (Noll, 2012). Figure 1 displays the theoretical procedure of a LIBS measurement. A short but powerful laser-beam is focused onto the samples surface, which can be solid, liquid or even gaseous. The submitted energy heats the surface and transfers minor amounts of the sample into a plasma that contains the elemental information of the evaporated area. Small volumes of solid surfaces are ablated during this process. The plasma cools rapidly, emitting specific radiation that is collected with two connected optical instruments: a spectrometer and a detector. In the resulting spectral information, elements show peak intensities at element specific wavelengths, which allows the detection of multiple elements within a single spectrum (Cremers and Radziemski, 2013). In addition to element specific intensity peaks, molecular emission can be measured as well (Cremers

and Radziemski, 2013). This can be exploited for elements that are difficult to detect under normal circumstances (e.g. in Gaft et al., 2014; Labutin et al., 2016; Vogt et al., 2020).

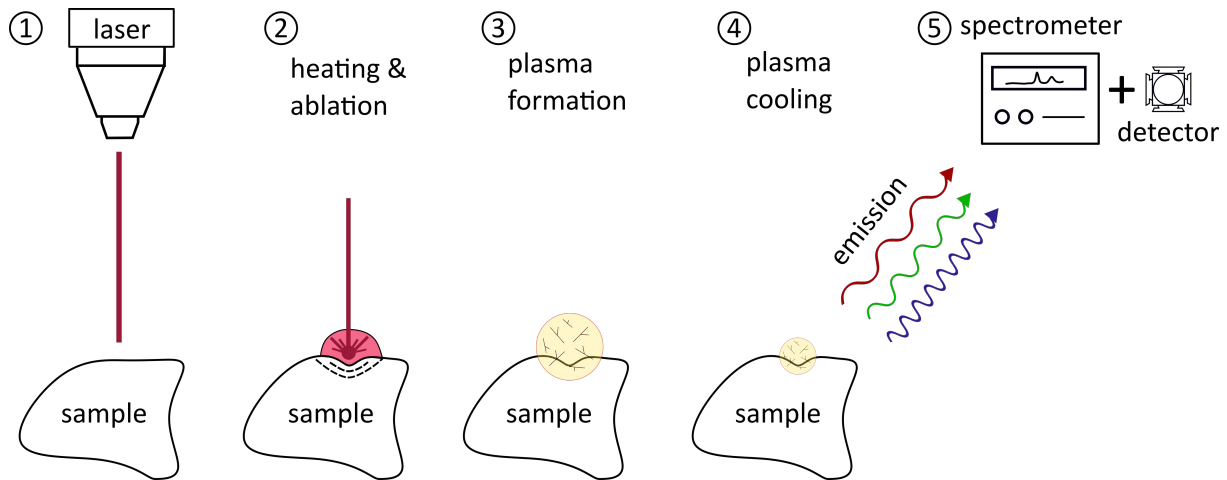


Figure 1: Theoretical procedure of a typical LIBS measurement. After laser ablation and heating, the created plasma cools rapidly and emits the elemental and molecular information in the form of light. The resulting emission is measured by a spectrometer and a detector.

The fundamental principles, laser-induced plasma and optically-induced breakdown, have been observed shortly after the first working laser was invented in 1960 (Radziemski and Cremers, 2013). In 1963, LIBS was analytically used for the first time, but it took nearly 20 years until research was intensified at the Los Alamos National Laboratory. The extended knowledge proved the distinct advantages of LIBS and made the method applicable to a wide variety of different fields (Noll, 2012; Radziemski and Cremers, 2013). Up to now, LIBS applications continuously increased, which is reflected in the steady growth of LIBS-related publications in peer-review journals displayed in Figure 2a.

Correlated with the increasing use for different applications, LIBS-based instruments were commercially accessible (Radziemski and Cremers, 2013). Nevertheless, each instrument is still mostly adapted to its specific area of operation until today, although the main components of every LIBS setup are identical. They always include a laser, a spectrometer able to monitor specific regions of the spectrum, a detector to collect the spectrally emitted light, and a computer to save and analyse the results (Noll, 2012). This general composition has not changed throughout the years, although great improvements in price and quality have been made for laser, spectrometer, detector, and computer, respectively. First handheld devices were developed in the mid 1990's, but it took several years until they became commercially available (Rakovský et al., 2014).

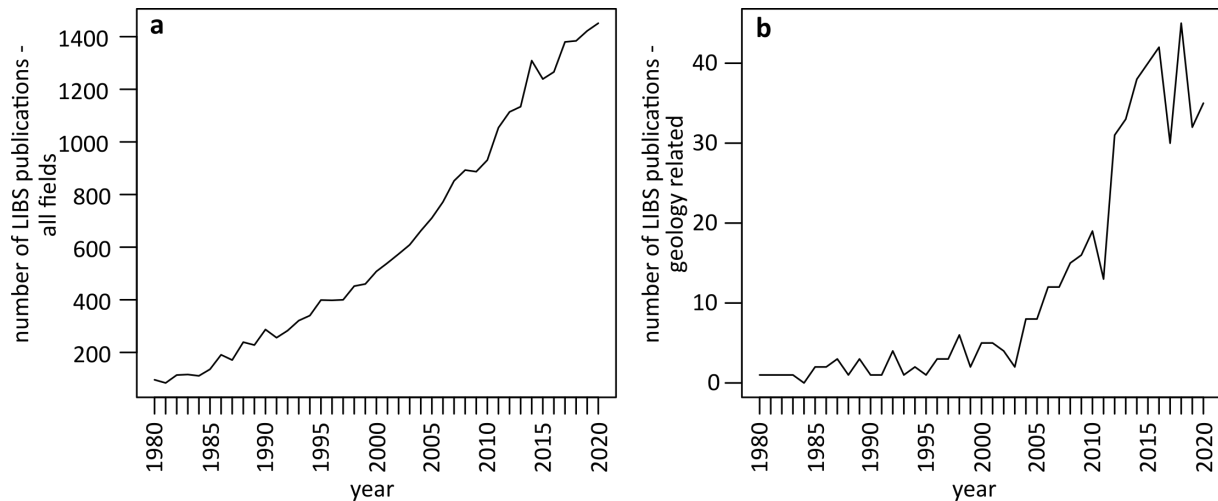


Figure 2: Number of LIBS related articles published in peer-reviewed journals from 1980 onwards. Figure 2a shows publications for all fields that LIBS was used in; Figure 2b only displays geology related publications. The number of publications was determined using the adjusted search results from <https://www.semanticscholar.org> (25.01.2022).

LIBS offers several advantages for many distinct applications (Noll, 2012), summarized in Table 1. It allows fast measurements of samples of all states of aggregation, in-situ and under atmospheric conditions. No sample treatment is required, and measurements can be performed remotely, which enables the use of LIBS even in areas not accessible by humans, e.g. melting furnaces or remote planets of our solar system (Myakalwar et al., 2021; Sirven et al., 2007; Wiens et al., 2013). Major, minor and trace elements can be detected at the same time within a single spectrum and even light elements like Li can be measured, which is especially challenging for many other analytical techniques (Fabre, 2020). Contrary to the numerous advantages, physical and chemical matrix effects propose severe challenges for the analysis of LIBS measurements, especially for complex heterogeneous material like drill core samples.

Table 1: Advantages and challenges of LIBS analytics. The bold points are especially important for geological applications.

Advantages	Challenges
Fast	<b>Physical matrix effects</b>
In-situ measurements possible	<b>Chemical matrix effects</b>
Measurements under atmospheric conditions	No transferability between different LIBS systems possible yet
Remote control possible	
Solid, liquid and gas can be measured	
<b>No sample treatment required</b>	
<b>Multi-element analysis</b>	
<b>Light elements can be detected</b>	

Physical matrix effects arise from the physical properties of the investigated sample, which influence the amount of material that is ablated by each laser pulse. Consequently, differences in e.g. surface structure or roughness, density, material hardness, transparency or even colour can alter the laser-induced plasma and therefore the resulting spectrum. Chemical matrix effects are a result of elements

interfering with the emission behaviour of other elements in the same plasma. Therefore, equal concentrations of the same element in different samples can lead to varying LIBS emission intensities (Harmon and Senesi, 2021; Tucker et al., 2010). These matrix effects usually prevent a straightforward analysis of heterogeneous material (Harmon and Senesi, 2021). This particularly applies to drill cores, since they include a variety of rocks, which themselves comprise a wide variety of different minerals.

### 1.3 LIBS in geology, from point measurements to imaging analysis

Several advantages are specifically important for geological applications (highlighted in Table 1 in **bold**) and one of the reasons for the increasing interest in LIBS for geological analytics (Figure 2b). First applications of LIBS in geology were published in the early 1990's, where the associated disadvantages, i.e. challenges concerning matrix effects, were already pointed out (Fabre, 2020). Since then, LIBS has seen an increasing interest in the geological community for element and mineral detection, as well as (semi-)quantitative analysis. The most famous application is the successful extra-terrestrial employment of LIBS in space, more specifically on Mars on board of the Curiosity rover (Wiens et al., 2013).

Continuous improvements in laser spot size and laser energy, as well as the development of fast and sensitive detectors enabled the use of LIBS for precise mappings of large geological samples. To create an elemental image with LIBS, a sample has to be scanned continuously, by moving either the sample or the laser after every single measurement. Thereto, the measurements can be performed “on-the-fly”, or with a short stop at each measurement position. The latter allows the use of cleaning shots, which can remove dust or unwanted debris from the sample, whereas the former allows a significantly faster measurement speed. The chosen step size determines the resolution of the resulting image (Jolivet et al., 2019). The first elemental mappings of geological material were published in 1998, where 5 x 5 cm large granite samples and manganese nodules were scanned (Yoon et al., 1997). Ten years later, Novotný et al., 2008 used LIBS imaging to create element maps of 2 x 2 cm large areas of a granitic samples, before Ma et al., 2010 presented multi-element maps using LIBS on an area covering 0.6 x 1.2 cm.

With improvements in technology, LIBS imaging of geological samples became more frequent, providing valuable information on the structure and the elemental distribution (Fabre, 2020; Jolivet et al., 2019). As a result, publications providing accurate maps of LIBS-based element distributions for various geological material and polymetallic ore in the size of up to 2.5 x 2.5 cm increased during the last decade (e.g. El Haddad et al., 2019; Fabre et al., 2018; Klus et al., 2016; Meima and Rammlmair, 2020; Nardecchia et al., 2020; Novotný et al., 2014; Rifai et al., 2018; Xu et al., 2016). Additionally, the first LIBS mapping of a complete drill core meter was performed on mine waste (Kuhn et al., 2016). Due to the size of the sample (100 x 1 cm), the measurements step size was set to 400 µm at a spot size of 200 µm.

The advances in LIBS instrumentation and computing power enabled a complex, multivariate analysis of the mappings. Different unsupervised and supervised methods were applied, and in addition to element imaging, first spatial results for mineralogical analysis were published in the last years (El Haddad et al., 2019; Fabre et al., 2018; Meima and Rammlmair, 2020; Nardecchia et al., 2020).

### 1.4 State-of-the-art for LIBS-based analysis of REEs and Li

Overall, only few publications analysed REEs with LIBS. Most REEs show only small intensity peaks in LIBS spectra of natural, unprocessed material under atmospheric conditions. As a consequence, a



common approach is to use powder, pellets or synthetic materials to detect or quantify the REE content or establish a theoretical LOD (e.g. Bhatt et al., 2020, 2018, 2017; Labutin et al., 2016; Martin et al., 2015; Rethfeldt et al., 2021; Wang et al., 2013). In 2017, Romppanen et al. presented the first measurement of a natural REE-bearing rock sample with LIBS. They were able to detect Y in a 1.5 x 1.5 cm LIBS-based mapping of grennaite ore from Sweden and perform mineral classification on the measured data. Two years later, Gaft et al., 2019 used a specialized LIBS setup with a very small laser spot size of approximately 15  $\mu\text{m}$  to measure different REE-bearing minerals. They were the first to present intensity peaks for molecular lines of LaO and YO and display imaging results for Ce and La in LIBS measurements of single mineral samples covering 0.1 x 0.15 cm in size.

Compared to REEs, Li is highly emissive and even small amounts can be traced in LIBS measurements of geological material (Fabre, 2020). The first paper on Li detection in natural minerals was published by Fabre et al., 2002. They accurately quantified single measurement points of LIBS on homogeneous Li-bearing minerals with univariate calibration curves that were obtained with synthetic glasses, lepidolite and muscovite. In the last year, LIBS-based quantification of Li in homogeneous minerals has also been provided for a handheld device (Fabre et al., 2022), as well as crushed spodumene ore (Rifai et al., 2022). Both publications used bulk- and inductively coupled plasma mass spectrometry (ICP-MS) analysis of complementary material as references to build the univariate calibration curve.

Additionally, other possible methods for the quantification of Li with LIBS have been investigated for different and more complex mineral and rock samples with a variety of approaches. Calibration-free LIBS (CF-LIBS) was applied to quantify Li in different gemstones (Rossi et al., 2014). Since emission lines of Li can show significant amounts of self-absorption during LIBS measurements, this approach was not successful. In the investigations of Sweetapple and Tassios, 2015, matrix-effects and self-absorption prevented an accurate LIBS-based Li quantification of the first 0.5 x 0.5 cm mapping of a hydrothermally altered spodumene pegmatite. They used synthetic glasses and whole-rock analysis of natural samples as reference samples, which resulted in semi-quantitative Li distribution maps. Several years later, Li concentrations could be provided indirectly for 1.2 x 1.3 cm mappings of granitic samples (Janovszky et al., 2021). Here, the ablated volume was used to calculate the Li concentrations of each measurement point. By comparing a handheld LIBS instrument with a laboratory setup, Ferreira et al., 2022 predicted the Li content of complete drill core meters using ICP-MS measurements as reference. Non-linear algorithms could produce semi-quantitative results for the laboratory instrument, whereas linear models performed significantly worse. For the more complex material, none of the publications were able to accurately quantify Li directly from the measured LIBS intensities. They showed that an accurate spatial quantification of heterogeneous rock samples with LIBS remains challenging due to matrix effects and saturation.

### 1.5 Challenges of spatial LIBS analysis and new contributions of this work

Despite the increasing interest in LIBS as an imaging tool in geosciences, the enormous amount of existing minerals, their varying colours, densities, structures, transparencies, and crystal sizes, as well as the variety of elemental compositions result in numerous physical and chemical matrix effects. These effects are especially prominent in LIBS measurements of large, heterogeneous drill core samples, and, depending on the investigated material, even the imaging of element distributions can remain challenging. As a result, most spatially resolved LIBS measurements of REE- or Li-bearing rocks cover only smaller parts of a complete sample or include single minerals larger than the laser spot size.

This work expands the existing scientific research concerning LIBS measurements of natural, REE- or Li-bearing rock samples with spatially resolved LIBS analysis of large and heterogeneous drill core samples from REE- and Li-bearing deposits. Thereby, the size of the presented LIBS mappings exceeds those of existing publications, and due to their heterogeneity and the variety of minerals involved, severe matrix effects were observed. To overcome these matrix effects, novel machine learning methods had to be implemented and new methods were developed to enable different kinds of spatially resolved LIBS analysis of large, heterogeneous drill core samples.

So far, LIBS imaging of REE-bearing material did not exceed the size of thin sections, and in the two existing publications on natural REE-bearing rocks (Gaft et al., 2019; Rompanen et al., 2017), the spot size of the LIBS instrument was smaller than the crystal size of the minerals. Detecting areas enriched in REEs in large mappings composed of small minerals remains challenging due to different matrix effects. In chapter 2, novel methods are employed to overcome these effects and enable the detection of La in large drill core samples of brecciated material, although the REE-bearing minerals are significantly smaller than the laser spot size and loosely distributed in the rock matrix. Spatially detailed LIBS mappings of heterogeneous drill core samples often include large numbers of different LIBS matrices in the form of minerals or areas problematic for the focus-dependant LIBS analysis, e.g. micro- or macro-porosities. To ensure the credibility of element detection, mineral classification or quantification, the detection of new LIBS matrices is an important addition to LIBS-based mineral classification of drill core samples. In chapter 3, a new classification model is developed, which allows the classification of minerals while also detecting unknown LIBS matrices. LIBS-based quantification of Li has successfully been performed for single or averaged shots of minerals surfaces. Nevertheless, matrix effects prevented a pixel-specific quantification of large mappings that include a variety of different minerals. Chapter 4 displays a novel approach for an accurate and spatially resolved LIBS-based quantification of large LIBS measurements.

### 1.6 LIBS instrumentation used in this work

All measurements for this dissertation were performed using a LIBS drill core scanner prototype at the Federal Institute of Geosciences and Natural Resources (BGR), developed by Lasertechnik Berlin (LTB) in 2011. The instrument is displayed in Figure 3. It operates under atmospheric conditions with a Q-switch Nd:YAG laser (20 Hz, 11 ns repetition rate at 1064 nm, 35 mJ energy, 200  $\mu$ m spot size), an Echelle spectrometer (285–964 nm spectral range, 0.029–0.096 nm resolution) and a charge-coupled device (CCD)-detector. To enable consecutive profile measurements of complete drill cores and mappings of coherent areas, the laser can move up to 100 cm in X- and 2.5 cm in Y-direction, while the sample stays in place. The instrument stops for every laser shot, before moving a desired distance in X or Y. This way, cleaning shots can be applied before the actual measurement is performed.

The sample chamber allows the measurement of drill cores with up to 1 m length in a single run. If the width of a mapping exceeds 2.5 cm, the sample is moved by hand parallel to the stage after the first area of the sample is measured. To avoid cross-crater contamination and the ionization of small dust particles between sample and laser head, a suction is mounted, moving alongside the laser. An optical camera is mounted on the X-axis of the movable rail to record an optical imaging of the analysed sample before or after the measurement.

The emitted light is collected with an optical fibre and transported to the Echelle spectrometer and the CCD-detector. The duration of large mappings can exceed several hours, potentially causing small temperature changes in the laboratory. To avoid spectral shifts due to the changes in temperature, the

spectrometer as well as the CCD-detector are consistently held at 27 °C. The software allows manual adaptations of measurement settings, which are optimized according to the measured material. Optimal values for the measurement parameters may change, depending on the main mineralogy of the sample. Therefore, the specific adjustments are explained in detail in every publication.

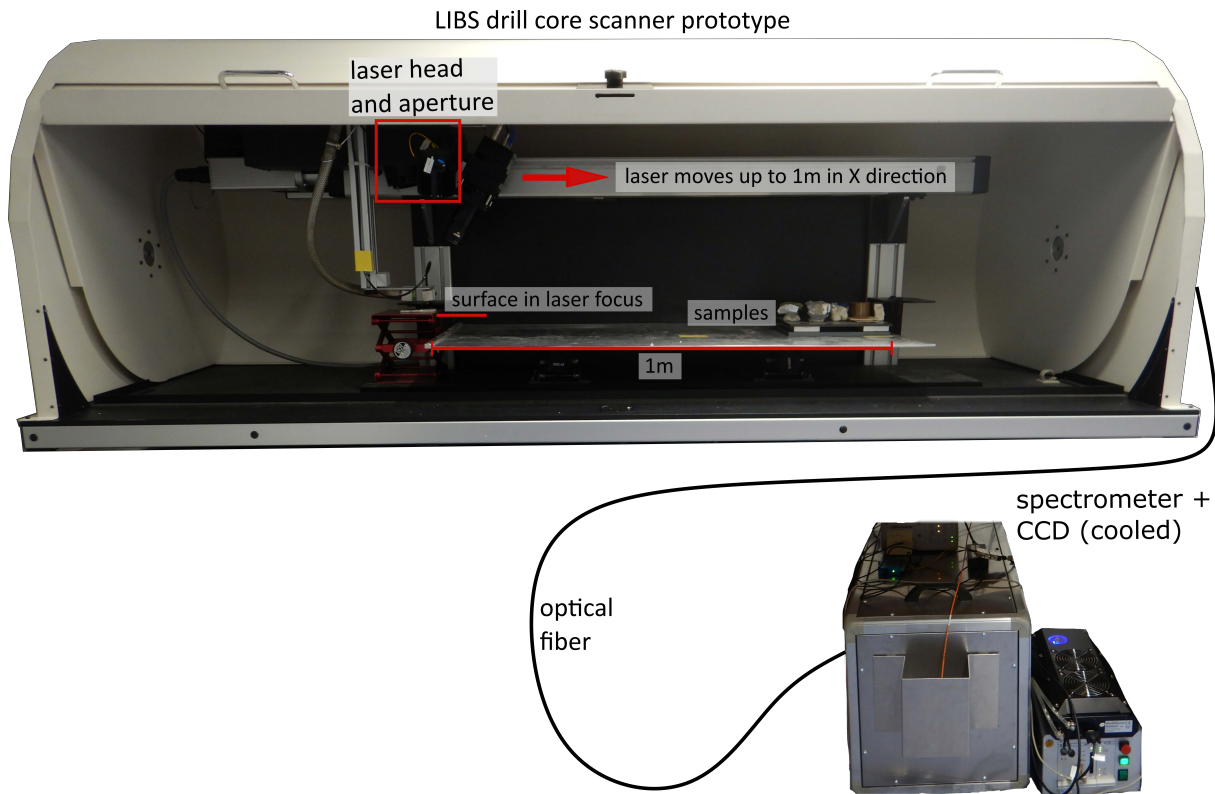


Figure 3: LIBS drill core scanner prototype used for all LIBS measurements performed in this work. The movable laser head allows measurements and mappings of complete drill core meters.

## 1.7 Reference measurements

The evaluation of LIBS measurements can be difficult, especially for large mappings, since only few instruments are able to provide adequate spatially resolved reference measurements. Nevertheless, validation measurements are crucial, and a variety of different methods have been used throughout the different publications, and a detailed description of the distinct instruments, as well as the measurement setups can be found therein. This chapter introduces the theoretical background of every method used for validation.

### 1.7.1 Electron microprobe

An electron microprobe is a well-established instrument to quantify even small concentrations of most elements accurately (Llovet, 2018). The sample is inserted into a chamber and a strong vacuum is created. Accordingly, the sample size is restricted in width and height, making sample preparation of drill core samples inevitable. Often, thin sections are created and coated with carbon, before they are inserted into an electron microprobe. To measure the material, a beam of electrons is fired at the sample surface, where it interacts with electrons of different atomic shells of each element present in the sample. As a result, X-rays are emitted with characteristic frequencies that are detected by the instrument (Llovet, 2018). To quantify the chemical composition of the investigated spot, element specific X-rays are compared to standardized materials.

The results obtained with an electron microprobe are very accurate, but the spot sizes are significantly smaller than those of the LIBS instrument used, only covering few  $\mu\text{m}$  in size. Since the measurement time is relatively high, mappings of large areas are not feasible. Electron microprobe measurements were therefore used in the first publication to proof the occurrences of REEs in the sample, to estimate the limit of detection (LOD) for La that can be achieved with the LIBS drill core scanner, and to estimate REE-oxide concentrations based on mass balance calculations.

### 1.7.2 Laser ablation-inductively coupled plasma-time of flight mass spectrometer (LA-ICP-TOFMS)

LA-ICP-TOFMS is an analytical technique that, like LIBS, is also based on laser ablation. Contrary to LIBS, the laser is not directly used as an excitation source, and instead, a carrier gas transports the ablated material to the ICP. While passing the high-energy ICP, it is atomized and ionized, before it is transferred to the time of flight mass analyser. There, the ion signal intensity of all elements of interest can be measured (Kendra, 2017). The signal strength corresponds to the abundance of the specific element in the sample. For quantification, known standards are measured and used to calibrate the instrument (Gundlach-Graham et al., 2015; Sylvester and Jackson, 2016).

LA-ICP-TOFMS generates quantitative mappings of small samples in a short amount of time. These spatially resolved element concentration maps were used in the third paper as a pixel-matched reference sample for LIBS measurements. Thereto, the same surface must be mapped with LIBS as well, and both datasets have to be matched pixel perfect. A detailed explanation of this procedure is given in chapter 4. Since the sample chamber limits the sample size of LA-ICP-TOFMS measurements, only a combination with LIBS enables the quantification of large drill core samples.

### 1.7.3 Energy dispersive X-ray fluorescence ( $\mu$ -EDXRF)

Contrary to the more common X-ray fluorescence (XRF) analysis,  $\mu$ -EDXRF is a non-destructive technique that is able to determine element distributions (semi-)quantitatively on a spatial level. Thereto, an X-ray from a primary X-ray source is shot onto the sample surface. Upon interaction, the primary X-ray ejects electrons from an inner shell of the targeted atom. When the empty spot is filled, a secondary, name-giving fluorescent X-ray is emitted. Contrary to XRF, an energy dispersive detection system directly measures the different energies of the X-rays emitted from the excited sample, instead of physically separating the X-rays by their distinct wavelengths. As a result,  $\mu$ -EDXRF can be used to detect multiple elements within a single spectrum, but its quantification accuracy is limited.

$\mu$ -EDXRF can be used for geological applications to create distribution maps of large samples for most elements (Nikonow and Rammlair, 2016), and it was therefore applied to validate the LIBS mappings qualitatively. Like LIBS, quantitative analysis directly from the spectrum is difficult, and the  $\mu$ -EDXRF results were not used as quantitative references.

## References

- Alonso, E., Sherman, A.M., Wallington, T.J., Everson, M.P., Field, F.R., Roth, R., Kirchain, R.E., 2012. Evaluating Rare Earth Element Availability: A Case with Revolutionary Demand from Clean Technologies. *Environ. Sci. Technol.* 46, 3406–3414. <https://doi.org/10.1021/es203518d>

- Balaram, V., 2019. Rare earth elements: A review of applications, occurrence, exploration, analysis, recycling, and environmental impact. *Geoscience Frontiers* 10, 1285–1303. <https://doi.org/10.1016/j.gsf.2018.12.005>
- Berkh, K., Rammlmair, D., 2022. The effect of Co substitution on the Raman spectra of pyrite: potential as an assaying tool. *European Journal of Mineralogy* 34, 259–274. <https://doi.org/10.5194/ejm-34-259-2022>
- Bhatt, C.R., Hartzler, D., Jain, J.C., McIntyre, D.L., 2020. Evaluation of analytical performance of double pulse laser-induced breakdown spectroscopy for the detection of rare earth elements. *Optics & Laser Technology* 126, 106110. <https://doi.org/10.1016/j.optlastec.2020.106110>
- Bhatt, C.R., Jain, J.C., Goueguel, C.L., McIntyre, D.L., Singh, J.P., 2018. Determination of Rare Earth Elements in Geological Samples Using Laser-Induced Breakdown Spectroscopy (LIBS). *Appl Spectrosc* 72, 114–121. <https://doi.org/10.1177/0003702817734854>
- Bhatt, C.R., Yueh, F.Y., Singh, J.P., 2017. Univariate and multivariate analyses of rare earth elements by laser-induced breakdown spectroscopy. *Appl. Opt.* 56, 2280–2287. <https://doi.org/10.1364/AO.56.002280>
- Booyesen, R., Lorenz, S., Thiele, S.T., Fuchsloch, W.C., Marais, T., Nex, P.A.M., Gloaguen, R., 2022. Accurate hyperspectral imaging of mineralised outcrops: An example from lithium-bearing pegmatites at Uis, Namibia. *Remote Sensing of Environment* 269, 112790. <https://doi.org/10.1016/j.rse.2021.112790>
- Chakhmouradian, A.R., Wall, F., 2012. Rare Earth Elements: Minerals, Mines, Magnets (and More). *Elements* 8, 333–340. <https://doi.org/10.2113/gselements.8.5.333>
- Charalampides, G., Vatalis, K.I., Apostoplos, B., Ploutarch-Nikolas, B., 2015. Rare Earth Elements: Industrial Applications and Economic Dependency of Europe. *Procedia Economics and Finance* 24, 126–135. [https://doi.org/10.1016/S2212-5671\(15\)00630-9](https://doi.org/10.1016/S2212-5671(15)00630-9)
- Chew, D., Drost, K., Marsh, J.H., Petrus, J.A., 2021. LA-ICP-MS imaging in the geosciences and its applications to geochronology. *Chemical Geology* 559, 119917. <https://doi.org/10.1016/j.chemgeo.2020.119917>
- Christmann, P., 2014. A Forward Look into Rare Earth Supply and Demand: A Role for Sedimentary Phosphate Deposits? *Procedia Engineering* 83, 19–26. <https://doi.org/10.1016/j.proeng.2014.09.005>
- Cremers, D., Radziemski, L., 2013. Handbook of Laser-Induced Breakdown Spectroscopy: Second Edition. *Handbook of Laser-Induced Breakdown Spectroscopy: Second Edition*. <https://doi.org/10.1002/9781118567371>
- El Haddad, J., de Lima Filho, E.S., Vanier, F., Harhira, A., Padioleau, C., Sabsabi, M., Wilkie, G., Blouin, A., 2019. Multiphase mineral identification and quantification by laser-induced breakdown spectroscopy. *Minerals Engineering* 134, 281–290. <https://doi.org/10.1016/j.mineng.2019.02.025>
- Fabre, C., 2020. Advances in Laser-Induced Breakdown Spectroscopy analysis for geology: A critical review. *Spectrochimica Acta Part B: Atomic Spectroscopy* 166, 105799. <https://doi.org/10.1016/j.sab.2020.105799>
- Fabre, C., Boiron, M.-C., Dubessy, J., Chabiron, A., Charoy, B., Martin Crespo, T., 2002. Advances in lithium analysis in solids by means of laser-induced breakdown spectroscopy: an exploratory study. *Geochimica et Cosmochimica Acta* 66, 1401–1407. [https://doi.org/10.1016/S0016-7037\(01\)00858-4](https://doi.org/10.1016/S0016-7037(01)00858-4)
- Fabre, C., Devismes, D., Moncayo, S., Pelascini, F., Trichard, F., Lecomte, A., Bousquet, B., Cauzid, J., Motto-Ros, V., 2018. Elemental imaging by laser-induced breakdown spectroscopy for the

- geological characterization of minerals. *J. Anal. At. Spectrom.* 33, 1345–1353. <https://doi.org/10.1039/C8JA00048D>
- Fabre, C., Ourti, N.E., Ballouard, C., Mercadier, J., Cauzid, J., 2022. Handheld LIBS analysis for in situ quantification of Li and detection of the trace elements (Be, Rb and Cs). *Journal of Geochemical Exploration* 236, 106979. <https://doi.org/10.1016/j.gexplo.2022.106979>
- Ferreira, M.F.S., Capela, D., Silva, N.A., Gonçalves, F., Lima, A., Guimarães, D., Jorge, P.A.S., 2022. Comprehensive comparison of linear and non-linear methodologies for lithium quantification in geological samples using LIBS. *Spectrochimica Acta Part B: Atomic Spectroscopy* 195, 106504. <https://doi.org/10.1016/j.sab.2022.106504>
- Gaft, M., Nagli, L., Eliezer, N., Groisman, Y., Forni, O., 2014. Elemental analysis of halogens using molecular emission by laser-induced breakdown spectroscopy in air. *Spectrochimica Acta Part B: Atomic Spectroscopy* 98, 39–47. <https://doi.org/10.1016/j.sab.2014.05.011>
- Gaft, M., Raichlin, Y., Pelascini, F., Panzer, G., Motto Ros, V., 2019. Imaging rare-earth elements in minerals by laser-induced plasma spectroscopy: Molecular emission and plasma-induced luminescence. *Spectrochimica Acta Part B: Atomic Spectroscopy* 151, 12–19. <https://doi.org/10.1016/j.sab.2018.11.003>
- Gaines, L., Richa, K., Spangenberg, J., 2018. Key issues for Li-ion battery recycling. *MRS Energy & Sustainability* 5, 12. <https://doi.org/10.1557/mre.2018.13>
- Ganguli, R., Cook, D.R., 2018. Rare earths: A review of the landscape. *MRS energy sustain.* 5, E9. <https://doi.org/10.1557/mre.2018.7>
- Goldberg, V., Kluge, T., Nitschke, F., 2022. Herausforderungen und Chancen für die Lithiumgewinnung aus geothermalen Systemen in Deutschland – Teil 1: Literaturvergleich bestehender Extraktionstechnologien. *Grundwasser - Zeitschrift der Fachsektion Hydrogeologie* 27, 239–259. <https://doi.org/10.1007/s00767-022-00522-5>
- Goodenough, K.M., Wall, F., Merriman, D., 2018. The Rare Earth Elements: Demand, Global Resources, and Challenges for Resourcing Future Generations. *Nat Resour Res* 27, 201–216. <https://doi.org/10.1007/s11053-017-9336-5>
- Greim, P., Solomon, A.A., Breyer, C., 2020. Assessment of lithium criticality in the global energy transition and addressing policy gaps in transportation. *Nat Commun* 11, 4570. <https://doi.org/10.1038/s41467-020-18402-y>
- Gundlach-Graham, A., Burger, M., Allner, S., Schwarz, G., Wang, H.A.O., Gyr, L., Grolimund, D., Hattendorf, B., Günther, D., 2015. High-Speed, High-Resolution, Multielemental Laser Ablation-Inductively Coupled Plasma-Time-of-Flight Mass Spectrometry Imaging: Part I. Instrumentation and Two-Dimensional Imaging of Geological Samples. *Anal. Chem.* 87, 8250–8258. <https://doi.org/10.1021/acs.analchem.5b01196>
- Harmon, R.S., Senesi, G.S., 2021. Laser-Induced Breakdown Spectroscopy – A geochemical tool for the 21st century. *Applied Geochemistry* 128, 104929. <https://doi.org/10.1016/j.apgeochem.2021.104929>
- Hatch, G.P., 2012. Dynamics in the Global Market for Rare Earths. *Elements* 8, 341–346. <https://doi.org/10.2113/gselements.8.5.341>
- Janovszky, P., Jancsek, K., Palásti, D.J., Kopniczky, J., Hopp, B., M. Tóth, T., Galbács, G., 2021. Classification of minerals and the assessment of lithium and beryllium content in granitoid rocks by laser-induced breakdown spectroscopy. *J. Anal. At. Spectrom.* 36, 813–823. <https://doi.org/10.1039/D1JA00032B>

- Jolivet, L., Leprince, M., Moncayo, S., Sorbier, L., Lienemann, C.-P., Motto-Ros, V., 2019. Review of the recent advances and applications of LIBS-based imaging. *Spectrochimica Acta Part B: Atomic Spectroscopy* 151, 41–53. <https://doi.org/10.1016/j.sab.2018.11.008>
- Kendra, 2017. What is Laser Ablation ICP-MS Imaging? [WWW Document]. TOFWERK. URL <https://www.tofwerk.com/laser-ablation-icp-ms-imaging/> (accessed 1.10.23).
- Kesler, S.E., Gruber, P.W., Medina, P.A., Keoleian, G.A., Everson, M.P., Wallington, T.J., 2012. Global lithium resources: Relative importance of pegmatite, brine and other deposits. *Ore Geology Reviews* 48, 55–69. <https://doi.org/10.1016/j.oregeorev.2012.05.006>
- Klus, J., Mikysek, P., Prochazka, D., Pořízka, P., Prochazková, P., Novotný, J., Trojek, T., Novotný, K., Slobodník, M., Kaiser, J., 2016. Multivariate approach to the chemical mapping of uranium in sandstone-hosted uranium ores analyzed using double pulse Laser-Induced Breakdown Spectroscopy. *Spectrochimica Acta Part B: Atomic Spectroscopy* 123, 143–149. <https://doi.org/10.1016/j.sab.2016.08.014>
- Kuhn, K., Meima, J.A., 2019. Characterization and Economic Potential of Historic Tailings from Gravity Separation: Implications from a Mine Waste Dump (Pb-Ag) in the Harz Mountains Mining District, Germany. *Minerals* 9, 303. <https://doi.org/10.3390/min9050303>
- Kuhn, K., Meima, J.A., Rammlmair, D., Ohlendorf, C., 2016. Chemical mapping of mine waste drill cores with laser-induced breakdown spectroscopy (LIBS) and energy dispersive X-ray fluorescence (EDXRF) for mineral resource exploration. *Journal of Geochemical Exploration* 161, 72–84. <https://doi.org/10.1016/j.gexplo.2015.11.005>
- Kushnir, D., Sandén, B.A., 2012. The time dimension and lithium resource constraints for electric vehicles. *Resources Policy* 37, 93–103. <https://doi.org/10.1016/j.resourpol.2011.11.003>
- Labutin, T.A., Zaytsev, S.M., Popov, A.M., Zorov, N.B., 2016. A novel approach to sensitivity evaluation of laser-induced breakdown spectroscopy for rare earth elements determination. *J. Anal. At. Spectrom.* 31, 2223–2226. <https://doi.org/10.1039/C6JA00200E>
- Llovet, X., 2018. Electron Probe Microanalysis, in: Reference Module in Chemistry, Molecular Sciences and Chemical Engineering. Elsevier, p. B9780124095472144000. <https://doi.org/10.1016/B978-0-12-409547-2.14369-0>
- Ma, Q.L., Motto-Ros, V., Lei, W.Q., Boueri, M., Zheng, L.J., Zeng, H.P., Bar-Matthews, M., Ayalon, A., Panczer, G., Yu, J., 2010. Multi-elemental mapping of a speleothem using laser-induced breakdown spectroscopy. *Spectrochimica Acta Part B: Atomic Spectroscopy* 65, 707–714. <https://doi.org/10.1016/j.sab.2010.03.004>
- Martin, G., Rentsch, L., Höck, M., Bertau, M., 2017. Lithium market research – global supply, future demand and price development. *Energy Storage Materials* 6, 171–179. <https://doi.org/10.1016/j.ensm.2016.11.004>
- Martin, M., Martin, R.C., Allman, S., Brice, D., Wymore, A., Andre, N., 2015. Quantification of rare earth elements using laser-induced breakdown spectroscopy. *Spectrochimica Acta Part B: Atomic Spectroscopy* 114, 65–73. <https://doi.org/10.1016/j.sab.2015.10.005>
- Maxwell, P., 2014. Analysing the lithium industry: Demand, supply, and emerging developments. *Miner Econ* 26, 97–106. <https://doi.org/10.1007/s13563-013-0041-5>
- Meima, J.A., Rammlmair, D., 2020. Investigation of compositional variations in chromitite ore with imaging Laser Induced Breakdown Spectroscopy and Spectral Angle Mapper classification algorithm. *Chemical Geology* 532, 119376. <https://doi.org/10.1016/j.chemgeo.2019.119376>
- Meima, J.A., Rammlmair, D., Junge, M., 2022. The use of Laser Induced Breakdown Spectroscopy for the mineral chemistry of chromite, orthopyroxene and plagioclase from Merensky Reef and

- UG-2 chromitite, Bushveld Complex, South Africa. *Chemical Geology* 589, 120686. <https://doi.org/10.1016/j.chemgeo.2021.120686>
- Myakalwar, A.K., Sandoval, C., Velásquez, M., Sbarbaro, D., Sepúlveda, B., Yáñez, J., 2021. LIBS as a Spectral Sensor for Monitoring Metallic Molten Phase in Metallurgical Applications—A Review. *Minerals* 11, 1073. <https://doi.org/10.3390/min11101073>
- Nardecchia, A., Fabre, C., Cauzid, J., Pelascini, F., Motto-Ros, V., Duponchel, L., 2020. Detection of minor compounds in complex mineral samples from millions of spectra: A new data analysis strategy in LIBS imaging. *Analytica Chimica Acta* 1114, 66–73. <https://doi.org/10.1016/j.aca.2020.04.005>
- Neff, C., Keresztes Schmidt, P., Garofalo, P.S., Schwarz, G., Günther, D., 2020. Capabilities of automated LA-ICP-TOFMS imaging of geological samples. *J. Anal. At. Spectrom.* 35, 2255–2266. <https://doi.org/10.1039/D0JA00238K>
- Nikonow, W., Rammlmair, D., 2016. Risk and benefit of diffraction in Energy Dispersive X-ray fluorescence mapping. *Spectrochimica Acta Part B: Atomic Spectroscopy* 125, 120–126. <https://doi.org/10.1016/j.sab.2016.09.018>
- Nikonow, W., Rammlmair, D., Meima, J.A., Schodlok, M.C., 2019. Advanced mineral characterization and petrographic analysis by  $\mu$ -EDXRF, LIBS, HSI and hyperspectral data merging. *Miner Petrol* 113, 417–431. <https://doi.org/10.1007/s00710-019-00657-z>
- Noll, R., 2012. *Laser-Induced Breakdown Spectroscopy: Fundamentals and Applications*. Springer Berlin Heidelberg.
- Novotný, J., Novotný, K., Prochazka, D., Hrdlička, A., Kaiser, J., 2014. Two dimensional elemental mapping by laser-induced breakdown spectroscopy 26, 5.
- Novotný, K., Kaiser, J., Galiová, M., Konečná, V., Novotný, J., Malina, R., Liška, M., Kanický, V., Otruba, V., 2008. Mapping of different structures on large area of granite sample using laser-ablation based analytical techniques, an exploratory study. *Spectrochimica Acta Part B: Atomic Spectroscopy* 63, 1139–1144. <https://doi.org/10.1016/j.sab.2008.06.011>
- Paris Agreement, 2015. . United Nations Treaty Collection, Chapter XXVII 7. d.
- Radziemski, L., Cremers, D., 2013. A brief history of laser-induced breakdown spectroscopy: From the concept of atoms to LIBS 2012. *Spectrochimica Acta Part B: Atomic Spectroscopy* 87, 3–10. <https://doi.org/10.1016/j.sab.2013.05.013>
- Rakovský, J., Čermák, P., Musset, O., Veis, P., 2014. A review of the development of portable laser induced breakdown spectroscopy and its applications. *Spectrochimica Acta Part B: Atomic Spectroscopy* 101, 269–287. <https://doi.org/10.1016/j.sab.2014.09.015>
- Rethfeldt, N., Brinkmann, P., Riebe, D., Beitz, T., Köllner, N., Altenberger, U., Löhmansröben, H.-G., 2021. Detection of Rare Earth Elements in Minerals and Soils by Laser-Induced Breakdown Spectroscopy (LIBS) Using Interval PLS. *Minerals* 11, 1379. <https://doi.org/10.3390/min11121379>
- Rifai, K., Constantin, M., Yilmaz, A., Özcan, L.Ç., Doucet, F.R., Azami, N., 2022. Quantification of Lithium and Mineralogical Mapping in Crushed Ore Samples Using Laser Induced Breakdown Spectroscopy. *Minerals* 12, 253. <https://doi.org/10.3390/min12020253>
- Rifai, K., Doucet, F., Özcan, L., Vidal, F., 2018. LIBS core imaging at kHz speed: Paving the way for real-time geochemical applications. *Spectrochimica Acta Part B: Atomic Spectroscopy* 150, 43–48. <https://doi.org/10.1016/j.sab.2018.10.007>
- Rifai, K., Özcan, L.-Ç., Doucet, F.R., Rhoderick, K., Vidal, F., 2020. Ultrafast Elemental Mapping of Platinum Group Elements and Mineral Identification in Platinum-Palladium Ore Using Laser Induced Breakdown Spectroscopy. *Minerals* 10, 207. <https://doi.org/10.3390/min10030207>



- Romppanen, S., Häkkänen, H., Kaski, S., 2017. Singular value decomposition approach to the yttrium occurrence in mineral maps of rare earth element ores using laser-induced breakdown spectroscopy. *Spectrochimica Acta Part B: Atomic Spectroscopy* 134, 69–74. <https://doi.org/10.1016/j.sab.2017.06.002>
- Rossi, M., Dell’Aglia, M., De Giacomo, A., Gaudio, R., Senesi, G.S., De Pascale, O., Capitelli, F., Nestola, F., Ghiara, M.R., 2014. Multi-methodological investigation of kunzite, hiddenite, alexandrite, elbaite and topaz, based on laser-induced breakdown spectroscopy and conventional analytical techniques for supporting mineralogical characterization. *Phys Chem Minerals* 41, 127–140. <https://doi.org/10.1007/s00269-013-0631-3>
- Schulz, K.J., DeYoung, Jr., John H., Seal II, R.R., Bradley, D.C., 2017. Critical mineral resources of the United States—Economic and environmental geology and prospects for future supply (Report No. 1802), Professional Paper. Reston, VA. <https://doi.org/10.3133/pp1802>
- Scrosati, B., Garche, J., 2010. Lithium batteries: Status, prospects and future. *Journal of Power Sources* 195, 2419–2430. <https://doi.org/10.1016/j.jpowsour.2009.11.048>
- Sirven, J.-B., Sallé, B., Mauchien, P., Lacour, J.-L., Maurice, S., Manhès, G., 2007. Feasibility study of rock identification at the surface of Mars by remote laser-induced breakdown spectroscopy and three chemometric methods. *Journal of Analytical Atomic Spectrometry* 22, 1471. <https://doi.org/10.1039/b704868h>
- Sweetapple, M.T., Tassios, S., 2015. Laser-induced breakdown spectroscopy (LIBS) as a tool for in situ mapping and textural interpretation of lithium in pegmatite minerals. *American Mineralogist* 100, 2141–2151. <https://doi.org/10.2138/am-2015-5165>
- Sylvester, P.J., Jackson, S.E., 2016. A Brief History of Laser Ablation Inductively Coupled Plasma Mass Spectrometry (LA-ICP-MS). *ELEMENTS* 12, 307–310. <https://doi.org/10.2113/gselements.12.5.307>
- Takahashi, T., Thornton, B., 2017. Quantitative methods for compensation of matrix effects and self-absorption in Laser Induced Breakdown Spectroscopy signals of solids. *Spectrochimica Acta Part B: Atomic Spectroscopy* 138, 31–42. <https://doi.org/10.1016/j.sab.2017.09.010>
- Tucker, J.M., Dyar, M.D., Schaefer, M.W., Clegg, S.M., Wiens, R.C., 2010. Optimization of laser-induced breakdown spectroscopy for rapid geochemical analysis. *Chemical Geology* 277, 137–148. <https://doi.org/10.1016/j.chemgeo.2010.07.016>
- Vogt, D.S., Schröder, S., Rammelkamp, K., Hansen, P.B., Kubitzka, S., Hübers, H.-W., 2020. CaCl and CaF emission in LIBS under simulated martian conditions. *Icarus* 335, 113393. <https://doi.org/10.1016/j.icarus.2019.113393>
- Wang, X., Motto-Ros, V., Panczer, G., De Ligny, D., Yu, J., Benoit, J.M., Dussossoy, J.L., Peugeot, S., 2013. Mapping of rare earth elements in nuclear waste glass–ceramic using micro laser-induced breakdown spectroscopy. *Spectrochimica Acta Part B: Atomic Spectroscopy* 87, 139–146. <https://doi.org/10.1016/j.sab.2013.05.022>
- Wiens, R.C., Maurice, S., Lasue, J., Forni, O., Anderson, R.B., Clegg, S., Bender, S., Blaney, D., Barraclough, B.L., Cousin, A., Deflores, L., Delapp, D., Dyar, M.D., Fabre, C., Gasnault, O., Lanza, N., Mazoyer, J., Melikechi, N., Meslin, P.-Y., Newsom, H., Ollila, A., Perez, R., Tokar, R.L., Vaniman, D., 2013. Pre-flight calibration and initial data processing for the ChemCam laser-induced breakdown spectroscopy instrument on the Mars Science Laboratory rover. *Spectrochimica Acta Part B: Atomic Spectroscopy* 82, 1–27. <https://doi.org/10.1016/j.sab.2013.02.003>
- World Economic Forum, A.-A., 2022. Net-zero industry tracker: 2022 edition.

- Wu, X., Ma, J., Wang, J., Zhang, X., Zhou, G., Liang, Z., 2022. Progress, Key Issues, and Future Prospects for Li-Ion Battery Recycling. *Global Challenges* n/a, 2200067. <https://doi.org/10.1002/gch2.202200067>
- Xu, C., Dai, Q., Gaines, L., Hu, M., Tukker, A., Steubing, B., 2020. Future material demand for automotive lithium-based batteries. *Commun Mater* 1, 99. <https://doi.org/10.1038/s43246-020-00095-x>
- Xu, T., Liu, J., Shi, Q., He, Y., Niu, G., Duan, Y., 2016. Multi-elemental surface mapping and analysis of carbonaceous shale by laser-induced breakdown spectroscopy. *Spectrochimica Acta Part B: Atomic Spectroscopy* 115, 31–39. <https://doi.org/10.1016/j.sab.2015.10.008>
- Yoon, Y.Y., Kim, T.S., Chung, K.S., Lee, K.Y., Lee, G.H., 1997. Application of Laser Induced Plasma Spectroscopy to the Analysis of Rock Samples†. *Analyst* 122, 1223–1227. <https://doi.org/10.1039/a704782g>

## 2. Detecting REE-rich areas in heterogeneous drill cores from Storkwitz using LIBS and a combination of k-means clustering and spatial raster analysis

**Simon Müller<sup>1\*</sup>, Jeannet A. Meima<sup>1</sup>, Dieter Rammlmair<sup>1</sup>**

<sup>1</sup>Federal Institute for Geosciences and Natural Resources, Stilleweg 2, 30650 Hannover, Germany

\*Corresponding author. E-mail address: [SimonArne.Mueller@bgr.de](mailto:SimonArne.Mueller@bgr.de)

### KEYWORDS

Laser Induced Breakdown Spectroscopy (LIBS), drill core scanner, k-means clustering, raster analysis, Rare Earth Elements (REE), Storkwitz carbonatite

DOI: [10.1016/j.gexplo.2020.106697](https://doi.org/10.1016/j.gexplo.2020.106697)



# Detecting REE-rich areas in heterogeneous drill cores from Storkwitz using LIBS and a combination of k-means clustering and spatial raster analysis

Simon Müller<sup>\*</sup>, Jeannet A. Meima, Dieter Rammlmair

Federal Institute for Geosciences and Natural Resources, Stilleweg 2, 30650 Hannover, Germany

## ARTICLE INFO

### Keywords:

Laser Induced Breakdown Spectroscopy (LIBS)  
 Drill core scanner  
 K-means clustering  
 Raster analysis  
 Rare earth elements (REE)  
 Storkwitz carbonatite

## ABSTRACT

This paper presents a novel approach to calculate matrix-matched intensity limits for the spatially resolved detection of rare earth element (REE) enrichments in highly heterogeneous geological material from the Storkwitz carbonatite based on scanning Laser Induced Breakdown Spectroscopy (LIBS). A drill core from the Storkwitz carbonatite was mapped in detail with a LIBS drill core scanner. For reference purposes,  $\mu$ -EDXRF was applied for qualitative REE detection, and a microprobe was used for quantitative REE analysis.

Microprobe analysis of thin sections verified the existence of rare earth elements and revealed an accumulation of REEs around mineral rims. Microprobe measurements also revealed that the main carrier of rare earth elements in the analysed drill core are REE-carbonates with contents as high as 24.4 wt% for Ce, 15.4 wt% for La, and 9.2 wt% for Nd. Apatite and pyrochlore are carrier for rare earth elements as well, however, with significantly lower concentrations of Ce (1.0 wt%), La (0.3 wt%), and Nd (0.3 wt%).

K-means clustering was applied on the LIBS mapping to separate classes that show similarities in chemical composition. The classes represent carbonates, silicates, and rock matrix, respectively. According to the microprobe results, most REE-carbonates were found to be related to elevated porosity or microfractures in the rock matrix, forming very thin rims of idiomorphic and hypidiomorphic minute crystals and rarely dense aggregates around exposed minerals and fractured rock fragments. Therefore, a buffer zone calculation was performed on the distinct mineral classes to extract pixel belonging to mineral rims only. Rims without any enrichment in rare earth elements were then used to calculate matrix-matched intensity limits for REE enrichments. Based on the observed similarity in chemical composition for rim pixel and rock matrix pixel, this intensity limit could be transferred to all pixels belonging to the rock matrix.

Based on the calculated intensity limits for La, 1.4 area % of the sample was found to be enriched in REE-carbonates. This result was validated qualitatively by comparing it to a  $\mu$ -EDXRF mapping of the same sample. Optical comparison showed good agreement and pixel counting confirmed similar zones of enrichment. The results reveal that La enrichments in REE-carbonates are reliably detected with LIBS. A mass balance calculation has shown that about 88% of the REE enrichments in the investigated drill core seem to occur as pure REE-carbonates. The fast detection of drill core areas that are enriched in REEs makes LIBS a viable addition to the currently used methods in REE exploration.

## 1. Introduction

Rare earth elements (REE) play a crucial role in several fields of today's technology and their demand is growing year-by-year (Ganguli and Cook, 2018; Goodenough et al., 2018; Charalampides et al., 2015). Only few deposits are known where REEs are enriched to a point that mining is feasible and lots of these deposits are bound to carbonatitic host rocks (Goodenough et al., 2018; Kanazawa and Kamitani, 2006). Often, several hundred meters of drill cores have to be taken for the

detection of relevant formations or new deposits.

Fast and detailed spatial information on the distribution of REEs and other relevant components in drill cores would facilitate both core logging and sample selection processes. Samples could be taken selectively and very precisely for quantitative geochemical and mineralogical analyses with established but more time-consuming methods (Fabre, 2020). Core scanner technologies may offer these new possibilities for spatially resolved analysis of REEs and other components in drill cores. Examples for different core scanner approaches and technologies based

<sup>\*</sup> Corresponding author.

E-mail address: [SimonArne.Mueller@bgr.de](mailto:SimonArne.Mueller@bgr.de) (S. Müller).

<https://doi.org/10.1016/j.gexplo.2020.106697>

Received 2 June 2020; Received in revised form 8 October 2020; Accepted 8 November 2020

Available online 11 November 2020

0375-6742/© 2020 Elsevier B.V. All rights reserved.

on XRF, LIBS and visible light and near infrared spectrometry can be found in Croudace et al. (2006), Haavisto et al. (2013), Kuhn et al. (2016), Liang et al. (2012), Meima and Rammlmair (2020), Ross et al. (2013) and Zuo (2013).

In the case of REE exploration, Laser Induced Breakdown Spectroscopy (LIBS) is a promising technology for fast detection of enriched areas in drill cores on the mining site. LIBS is a spectroscopic technique based on emission of plasma. A laser beam is focused on the surface of a sample (solid, liquid or gas) and its energy creates a plasma out of the ablated material. During cooling, spectral emission correlated to atomic or molecular lines can be observed and measured with optical instruments. Specific elements show peak intensities at element specific wavelengths, which allows the detection of multiple elements in one atomic spectrum (Cremers and Radziemski, 2013; Hahn and Omenetto, 2012, 2010). REEs are sometimes difficult to measure due to weak emission lines but several authors showed examples for a successful detection of a number of different rare earth elements in different materials (Abedin et al., 2011; Bhatt et al., 2018; Fabre et al., 2018; Gaft et al., 2019; Martin et al., 2015; Romppanen et al., 2017; Wang et al., 2013).

LIBS offers the possibility to analyse single samples and even complete drill cores in 1D or 2D fast with high resolution and nearly no sample preparation needed (e.g. Kuhn et al., 2016; Meima and Rammlmair, 2020). Additionally, the measurements can be performed in-situ under atmospheric conditions and practically all elements can be measured (Effenberger and Scott, 2010; Galbács, 2015; Hahn and Omenetto, 2012). Nevertheless, especially the quantification of heterogeneous materials is challenging due to various physical and chemical matrix effects (Cremers and Radziemski, 2013; Hahn and Omenetto, 2012; Miziolek et al., 2006; Takahashi and Thornton, 2017). This is why LIBS in geology has mostly been used for classification problems and qualitative analysis of rocks or minerals (e.g. El-Saeid et al., 2019; Gottfried et al., 2009; Harmon et al., 2013; Khajehzadeh and Kauppinen, 2015; Lui and Koujelev, 2011; Meima and Rammlmair, 2020; Nikonow et al., 2019; Sirven et al., 2007). However, an increasing number of applications aims at using LIBS for quantitative geological applications as well (e.g. Death et al., 2008; El Haddad et al., 2019; Kuhn et al., 2016; Kuhn and Meima, 2019; Meima and Rammlmair, 2020; Pagnotta et al., 2020; Pořízka et al., 2014; Sanghavi et al., 2016; Tucker et al., 2010; Wiens et al., 2013).

Most carbonatitic REE deposits are exposed to various phases of hydrothermal alteration leading to their REE enrichment (Nadeau et al., 2015). The relevant rare earth bearing minerals mostly occur in the form of small aggregates at pathways of hydrothermal fluids, like fracture zones or as thin crusts around mineral rims, which they sometimes replace completely (Deng et al., 2017). Scanning LIBS has been shown to be capable of the detection of trace elements in small aggregates in a highly heterogeneous geological material (Díaz et al., 2017; Fabre et al., 2018; Meima and Rammlmair, 2020). The reliable detection of REEs in a highly heterogeneous geological environment, however, could be strongly improved by matrix-matched intensity limits. In this paper, an innovative combination of unsupervised clustering and raster analysis has been investigated for this purpose. To be able to detect aggregates that are enriched in REEs, it is necessary to separate the LIBS spectra that belong to the rock matrix on the one hand, and the spectra belonging to the mineral rims on the other hand. So far, unsupervised clustering techniques have only rarely been applied on LIBS mappings, and for different purposes, e.g. to investigate the composition of archaeological samples, identify brass alloy compositions, evaluate damage in concrete samples or detect wavelengths for the quantification of heavy metals in shellfish (Gottlieb et al., 2017; Pagnotta et al., 2015, 2017; Yuan et al., 2018).

In this paper, we present a novel approach to detect spots with increased REE contents in a large geological LIBS mapping using a combination of k-means clustering and raster analysis. We analysed a highly heterogeneous drill core from the central complex of the

Storkwitz carbonatite in eastern Germany. This carbonatitic complex has been investigated in detail by Krüger et al. (2013) and Seifert (2000). The dominant rock type is a poly-breccia that contains broken mineral or rock fragments, so called clasts of both, country rock and earlier stage carbonatites that are embedded in a matrix with different or similar composition as the clasts. For REE detection, rock matrix and clasts were divided using k-means clustering before raster analysis was performed to extract all points that belong to mineral rims. In a last step, mineral rims without REE enrichment were used as a matrix-matched subset to establish a limit for the spectral intensity above which REE-carbonates can be detected with our LIBS system.

## 2. Materials and methods

### 2.1. Sampled material and reference measurements

The Storkwitz complex includes a mixture of carbonatite related fragments such as carbonates (containing CO<sub>3</sub>), apatite and phlogopites. Additionally, host rock fragments of silicates (containing high concentrations of SiO<sub>2</sub> and combinations of K<sub>2</sub>O and Na<sub>2</sub>O) and palaeozoic sediments can be found. These clasts are embedded in a carbonatitic matrix (Krüger et al., 2013; Seifert, 2000), which appears to be a mixture of multiple breccia generations of a mainly carbonatitic mineral assemblage and variable amounts of host rock fines. It is important to notice that despite not being indicated by its name, the Storkwitz carbonatite still contains roughly 50% of felsic components, which are not composed of carbonate. For more detailed information on the Storkwitz complex, we refer to Krüger et al. (2013), Seifert (2000) and Niegisch et al. (2020).

The analysed drill core is part of drilling SES 1/2012 carried out by the Seltenerden Storkwitz AG in 2012. It comes from a depth of 493 m and stratigraphically belongs to the centre of the central complex. Table 1 gives an overview of the relevant petrographic unit of the Storkwitz complex, the occurring rock types, their major and minor rock forming minerals and the associated compositions as identified by Krüger et al. (2013) and Seifert (2000). The investigated drill core belongs to the carbonatites, more precisely to the Dolomite-Carbonatite breccia, and seems to be representative for the central complex of Storkwitz.

The analysed sample contains a large variety of clasts ranging from millimetres up to several centimetres in size. The clasts cover various minerals of carbonatite and silicate origin (Table 1) and are embedded in a matrix of carbonatite minerals and rock fines. The core was cut in half and a 1 cm thick slice was removed. Three quadratic thin sections with a length of 2.2 cm were cut out of the removed cuboid for microprobe measurements, covering clasts with varying compositions as well

**Table 1**

List of minerals with formulae occurring in host rock fragments and attributed to different stages of the Storkwitz Dolomite-Carbonatite breccia itself.

Rock types	Major and minor rock forming minerals	Formulae
Granitoid clasts	Richterite	Na[CaNa](Mg, Fe <sup>2+</sup> ) <sub>5</sub> [(OH) <sub>2</sub> ]Si <sub>8</sub> O <sub>22</sub> ]
	Aegirine	NaFe <sup>3+</sup> [Si <sub>2</sub> O <sub>6</sub> ]
	Alkali feldspar	KAlSi <sub>3</sub> O <sub>8</sub>
	Quartz	SiO <sub>2</sub>
Clasts of palaeozoic sediments	Quartz, clays	
	Plagioclase, clays	
Early-stage carbonatite-related clasts	Dolomite	CaMg[CO <sub>3</sub> ] <sub>2</sub>
	Calcite	Ca[CO <sub>3</sub> ]
	Ankerite	CaFe[CO <sub>3</sub> ] <sub>2</sub>
	Apatite	Ca <sub>5</sub> [(F, Cl, OH)(PO <sub>4</sub> ) <sub>3</sub> ]
	Pyrochlore	Ca <sub>2</sub> Nb <sub>2</sub> O <sub>7</sub>
	Phlogopite	KMg <sub>3</sub> [(F, OH) <sub>2</sub> ]AlSi <sub>3</sub> O <sub>10</sub> ]
Post brecciation matrix	Various interfragmentoidal carbonates	(CaMgFeMnSr) <sub>2</sub> [CO <sub>3</sub> ] <sub>2</sub>
Late stage crystallites	REE-carbonates	(Ce, La, Nd, Y)[(F, OH)CO <sub>3</sub> ]



as the rock matrix (Fig. 1A). The area below the removed slice (Fig. 1B) was mapped with  $\mu$ -EDXRF and LIBS, revealing a slightly different surface than the thin sections. Since the main purpose of microprobe measurements was the quantitative verification of REE existence in the core, measuring the exact same surface is not necessary for the method presented.

The electron microprobe measurements were performed with a JEOL JXA-8530F Hyperprobe. For analysis, an acceleration voltage of 20 kV, a sample current of 50 nA and a beam diameter of 10  $\mu$ m were used. Measurement time varies between 10 and 60 s depending on the specific element. Elements were calibrated against topaz (F), celestine (Sr) and monazite (La, Ce, Nd). Additionally, the standards periclase (Mg), quartz (Si), calcite (Ca), rhodochrosite (Mn), siderite (Fe), smithsonite (Zn) and REE-glass (Pr, Sm, Gd, Dy) were used for the calibration of carbonates. For apatite and pyrochlore, the additional standards willemite (Zn), almandine (Fe), jadeite (Na), xenotime (Y), zircon (Zr), rhodonite (Mn), tugtupite (Cl), columbite (Nb, Ta), baryte (Ba, S), monazite (Pr, Sm), albite (Si), pyrope (Mg), plagioclase (Al), orthoclase (K), apatite (Ca, P) and rutile (Ti) were chosen. Corrections were performed using the PRZ ( $\phi$ - $\rho$ - $z$ ) method and an in-house spreadsheet. Detailed information on the PRZ method can be found in Brown (1991). The total number of measurement points per mineral varies according to the mineral distributions in the sample. Additionally, ankerite, dolomite and calcite were combined, leading to an elevated number of measurement points for carbonates.

A proper validation of spatially resolved LIBS-based REE enrichment results would ideally require space-resolved REE reference measurements with an analytical technology capable of REE analysis. However, this solution, using a scanning microprobe or LA-ICP-MS for example, would be extremely time consuming, cost intensive and not possible with such a large sample. At this stage of our research, we opted for a qualitative validation of the results. Thereto, the sample that was mapped with LIBS was mapped beforehand with the Energy Dispersive X-Ray Fluorescence ( $\mu$ -EDXRF) spectrometer M4 Tornado (Bruker Nano GmbH, Germany). The Rh-tube, equipped with a polycapillary at an

incident angle of 51° was operated with an excitation energy of 50 kV, 600  $\mu$ A (30 W) and a spot size of 20  $\mu$ m. Data acquisition was done sequentially by two opposing detectors with 51° take off angle each at 2 ms per pixel acquisition time. Data evaluation was done by calculating the minimum signal per pixel of both detectors to eliminate diffraction signals in 2D element distribution patterns. The complete mapping also covers 10  $\times$  15 cm. For further information on the instrument, its specifications and the methodology, we refer to Nikonov and Rammlmair (2016).

## 2.2. LIBS setup

The LIBS mappings were carried out with a drill core scanner prototype developed by Lasertechnik Berlin (LTB) in 2011. The LIBS aperture consists of a 20 Hz Q-switch Nd-YAG laser that fires 11 ns pulses at 1064 nm with an energy of 50 mJ, an Echelle spectrometer (285–964 nm spectral range, 0.029–0.096 nm resolution) with a CCD detector and an optical camera. An exhaust system is mounted to avoid cross-crater contamination and the ionization of dust particles between laser head and focus point. The laser can move up to 1 m in X and 2.5 cm in Y direction and has a spot size of 200  $\mu$ m. To reduce the effects of temperature change on the spectrometer to a minimum, spectrometer and CCD are constantly held at 27 °C. Additional information on the parts and the general structure of the scanner can be found in Kuhn et al. (2016) and Meima and Rammlmair (2020).

Delay time and the number of laser shots to accumulate were optimized beforehand based on the maximum line emission of major elements in similar material. For this experiment, a delay time of 1  $\mu$ s was chosen. The scans were produced point by point with a short stop for each specific point measurement. For every measurement position, three laser pulses were accumulated. All spectra were background-corrected using a built-in dark measurement subtraction. The entire sample surface of 10  $\times$  15 cm was mapped with a step size of 200  $\mu$ m in four distinct measurements (Fig. 1C). After one area was mapped, the sample was moved by hand parallel to the stage for 2.5 cm in the specified direction

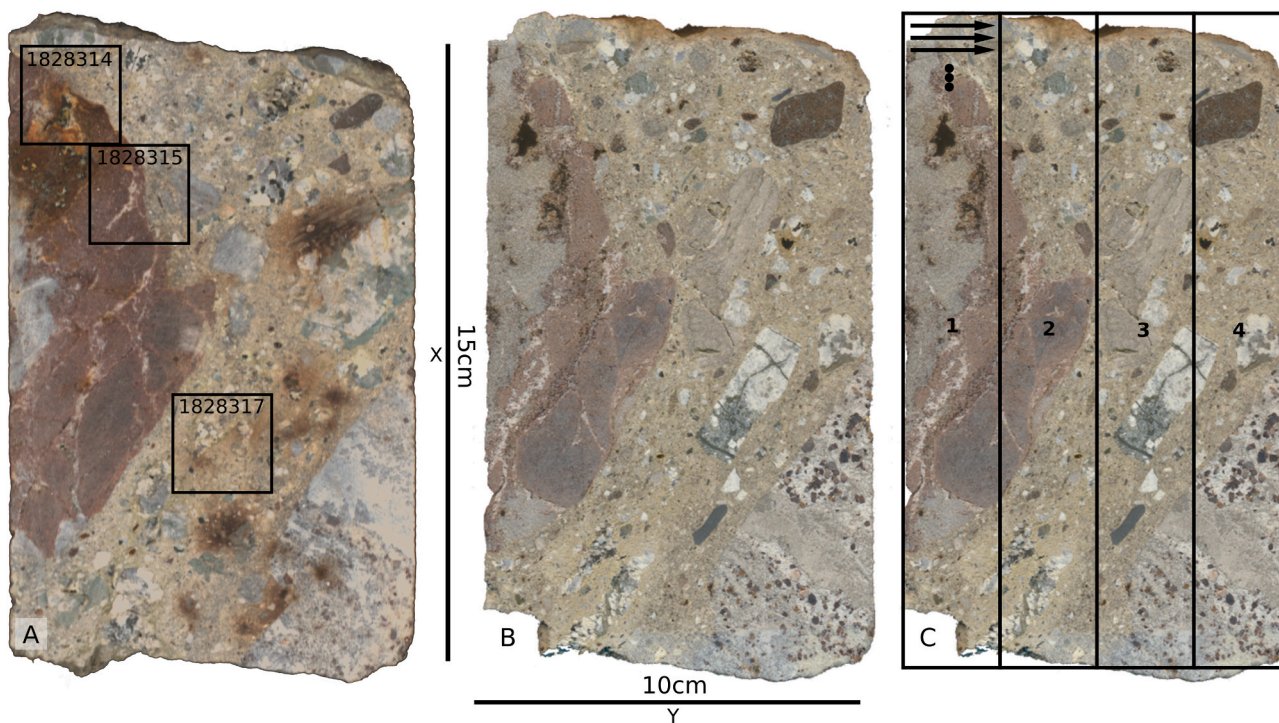


**Fig. 1.** (A) Positions of the thin sections 1828314, 1828315, and 1828317 on the core before a 1 cm slice was removed. Thin sections were used for microprobe analysis. (B) Core sample of the Storkwitz deposit measured with  $\mu$ -EDXRF and LIBS after the 1 cm slice was removed. (C) Distinct areas mapped with the LIBS drill core scanner. The arrows indicate the direction of the laser movement for mapping. Area 1, 2 and 3 cover 2.5  $\times$  15 cm, area 4 covers 2.4  $\times$  15 cm in size.

(Fig. 1C). Areas 1 to 3 cover  $2.5 \times 15$  cm, area 4 covers  $2.4 \times 15$  cm. The four distinct mappings were merged to one dataset that comprises the entire surface. Fig. 2 shows parts of a typical spectrum from a measurement spot rich in REEs and zooms in on spectral regions with characteristic emission lines for Ce, La and Nd.

### 2.3. Data processing

The raw data of the LIBS measurements were processed as described below. All software-dependant processing from step 2 onward was done using the open-source software R, Version 3.5.1 (R Core Team, 2018).

#### 2.3.1. Step 1

The spectrometer covers 36,400 distinct bands. Since the sample contains only a certain number of key elements (Table 1), using all bands would create a huge amount of redundant information, whereas spectral binning could result in a loss of information. Therefore, a total number of 66 emission lines were selected beforehand (Table 2), based on the expected minerals and their corresponding element composition (Table 1). Accordingly, all major rock forming elements (i.e. Al, Ca, Fe, K, Mg, Mn, Na, Si and Ti) were considered. Beryllium, Li, Ba, and Sr are often associated with REE occurrences and were therefore added to the list. Phosphor is an indicator for apatite, a possible carrier of REEs. Carbon was included because of the abundance of calcite and dolomite. The remaining elements are the rare earth elements Ce, La, Pr, Sm, Gd and Nd, as well as Nb, Y, and Ta.

The selected elements as well as their wavelengths are listed in Table 2. Where possible, at least three distinct wavelengths of different strength were selected to be able to identify possible interferences or self-absorption effects on individual emission lines. References for element specific wavelengths were the NIST-, Kurucz and AtomTrace-Databases available online (AtomTrace, 2020; Kramida et al., 2017; Smith et al., 2001), as well as Kuhn et al. (2016), Meima and Rammlair (2020) and the U.S. Army Research Laboratory (2010). Additionally, some REE specific wavelengths were taken from Abedin et al. (2011)

**Table 2**

Selected emission lines for major rock forming elements, minor elements, and REE.

Element	Spectral line (nm)
Al I	308.22, 394.40, 396.15
Ba II	553.55, 614.17, 712.03
Be II	313.04, 313.11
C I	909.48
Ca I	430.25
Ca II	315.89, 396.85
Ce II	394.28, 415.20, 457.23
Fe I	358.12, 371.99, 373.49
Gd I	371.36, 405.36, 419.08
Gd II	342.28
K I	766.49, 769.90
La I	394.91
La II	333.75, 338.09, 408.67
Li I	610.36, 670.78
Mg I	285.21, 517.27, 518.36
Mn I	403.08, 403.31, 403.45
Na I	588.99, 589.59, 819.48
Nb I	379.12, 412.38, 416.37
Nb II	313.06
Nd II	401.23, 415.63
P II	603.4, 604.31
Pr I	513.38
Pr II	417.94
Si I	288.16, 390.55
Si II	634.71
Sm I	429.67, 447.09
Sr I	460.73
Sr II	407.77, 421.55
Ta I	331.12, 406.14
Ta II	301.25
Ti II	308.80, 336.12, 337.28
Y II	371.03, 377.43, 417.75

and Bhatt et al. (2018). Furthermore, for reference purposes, the standardized reference sample CGL 111, containing 2.90 wt% Ce, 1.93 wt% La and 8800 ppm Nd, was also analysed with our LIBS system.

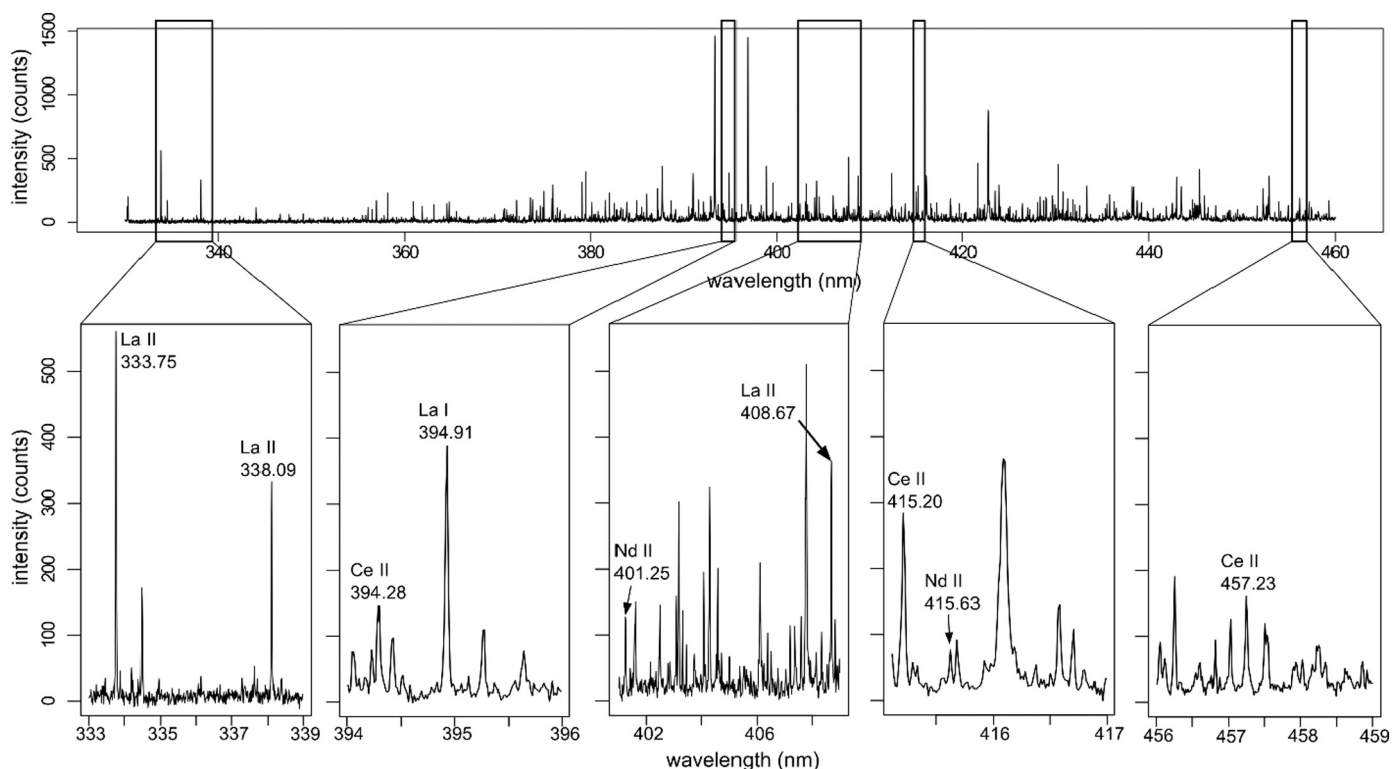


**Fig. 2.** LIBS spectrum enriched in REEs, with emphasis on spectral regions with characteristic emission lines for Ce, La, and Nd.

Peak integration was performed with an in-house C-program using an integration window of 0.05 nm. The size of the integration window was set relatively small to avoid overlap between emission lines close to each other. To prevent an unrealistic fit due to the integration of very close peaks, the intensity change around the centre of the expected peaks is monitored. If the intensity change does not follow a peak shape, the integration is aborted.

### 2.3.2. Step 2

Intensities of the extracted emission lines were stored in a LIBS hyperspectral data cube of stacked images, where each image represents the intensity distribution for one extracted emission line and each pixel corresponds to a single LIBS measurement. A more detailed description of the data cube can be found in [Meima and Rammlair \(2020\)](#).

### 2.3.3. Step 3

The cumulative intensity of all extracted emission lines was used to normalize the raw LIBS data to reduce shot-to-shot variations. Thereto, for every single pixel, the cumulative intensity of all extracted emission lines of [Table 2](#) was calculated. The raw intensity of every single emission line was then divided by the corresponding cumulative intensity.

### 2.3.4. Step 4

K-means clustering was applied to divide rock matrix and clasts as a first step in the extraction of mineral rims. We used the algorithm integrated in the R-stats package ([R Core Team, 2018](#)) and used as input the normalized intensities for all LIBS spectra as described in step 1, 2 and step 3. The algorithm divides  $n$  observations into  $k$  cluster. Each observation, which in our case represents one pixel, is connected to its nearest cluster centre based on the distance. The number of centres  $k$  has to be predefined. K-means was first introduced by [MacQueen \(1967\)](#) after an idea of [Steinhaus \(1956\)](#) and we refer to those papers for a detailed description.

The first cluster centres are initialized randomly, which can lead to a different partition of the data in different runs, even though the amount of centres remains constant. To avoid this problem of reproducibility, multiple initial configurations are created. In our case, using ten initial configurations lead to identical clustering results for five runs. The partitioning with the most replications is chosen as the output. The predefined number of maximum iterations was set to 200 but was never reached.

The optimal number for  $k$  is not known beforehand and several different internal criteria exist to calculate the optimum for  $k$ . We used the PBM-Index developed by [Pakhira et al. \(2004\)](#), which is integrated in the R package 'clusterCrit' ([Desgraupes, 2018](#)). It has been shown to deliver excellent results, mostly superior over several other criteria ([Vendramin, 2010](#); [Wang and Zhang, 2007](#)). The computational intensive PBM-Index was calculated for a representative subset of the data. We therefore subsampled the data randomly into 40,000 observations  $n$ , clustered the subset and calculated the optimal number of clusters based on the PBM-Index. Here, three cluster centres were found to be optimal and therefore used. Subsequently the  $k$ -nearest neighbour (knn) algorithm was used to fit the complete dataset to its closest cluster centre. In three runs with differently randomized sample sets, only 0.05% of the points showed differences in classification. Three clusters would also correspond to the number of major rock types, i.e. silicates, carbonates and the rock matrix and therefore, the complete dataset was clustered with  $k$ -means using three cluster centres.

The application of  $k$ -means for highly heterogeneous materials using spectral data e.g. from LIBS experiments may seem surprising, as the convex nature of  $k$ -means may lead to inappropriate classification with hard borders unable to consider potential outliers. However, we initially also tested other clustering algorithms such as DBSCAN, EM-clustering, and Self-Organizing-Maps. The results were nearly identical to those obtained with  $k$ -means. In comparison,  $k$ -means is computationally fast and easy to employ. This allows the establishment of meaningful

internal cluster criteria to find the optimal parameter  $k$  by testing a large number of different cluster centres. This is especially useful for large datasets like the one used in this paper, which otherwise would take a long time to process. Although sample heterogeneity is high, the three rock types show typical differences in several emission lines, which explains why meaningful results could be obtained with  $k$ -means as well. Additionally, we investigated the use of Principal Component Analysis (PCA) for dimensionality reduction before clustering. However, as there was no difference in the clustering result and no enhancement regarding computing time, we discarded PCA.

### 2.3.5. Step 5

A majority filter with  $5 \times 5$  kernel was applied to smooth the image and integrate single pixel into their surrounding class. This is important from a geological point of view for two reasons: (1) Single pixel that are assigned as a clast but are inside the rock matrix are too small to be clasts and (2) Single pixel that are defined as rock matrix but are inside of clasts are falsely classified and instead are part of the specific clast. In both cases, the class was assigned wrong since a single point with a diameter of  $200 \mu\text{m}$  is neither a complete clast nor matrix. To integrate these pixels into their surroundings, we used an approach similar to closing in image analysis: A majority filter was employed to the clustering result and the central pixel of the  $5 \times 5$  kernel was assigned to the most frequent class in the 25 considered pixel. Padding was used to prevent size reduction at the edges. This can lead to an equal distribution of classes for edge pixel, in which case the class of the central pixel was not changed.

The size of the moving window is crucial for the result. Since three classes were produced during clustering, a  $3 \times 3$  window is not effective in case each class is assigned three pixels, whereas a  $7 \times 7$  window covers 49 pixel in total. Since this is a large area, parts of the matrix between bigger clasts would wrongly be assigned as a clast. Due to the spot size of  $200 \mu\text{m}$ , a  $5 \times 5$  window corresponds to a square with 1 mm length, which is suitable for assigning even small minerals as well as the rock matrix correctly. This way, single particles with a small grain size around  $200 \mu\text{m}$  are adjusted according to their surrounding material. Although this causes finest fractions to disappear, it increases geological accuracy, since clasts are rarely this small and rock matrix normally does not occur in such small fractions inside of clasts.

### 2.3.6. Step 6

A buffer zone was calculated corresponding to mineral rims of separated clasts. We used the 'raster' package in R ([Hijmans, 2019](#)) to calculate a buffer zone around the clasts identified with  $k$ -means. This buffer zone matches the mineral rims and consists of pixel belonging to the Matrix-Cluster and its size is important: If the buffer zone is too big, information on mineral border chemistry will be mixed with chemistry of the pure rock matrix. One pixel in our mapping already corresponds to  $200 \mu\text{m}$ , so only one pixel was used as the buffer distance.

### 2.3.7. Step 7

As a last step, matrix-matched intensity limits were calculated for La. These limits enable the identification of a spectral intensity, above which REE-carbonates can be detected with the LIBS system used. Calculations are based on the La emission lines, which showed much higher abundancies compared to the other investigated REE lines. A matrix-matched background signal without any excitation was created using only pixel of rims that are not enriched in La as a subset. Outliers were removed using an iterative Z-score to receive a normal distribution ([Spiegel et al., 2013](#)). The intensity limit was then calculated based on the mean and 3 times the standard deviation of the background signal. The normalization described in step 3 is not expected to affect this calculation, because all processing is matrix-matched and the calculated intensity limit is applied only to pixel with similar matrix.

The different steps are summarized in [Table 3](#), where the performed task as well as a short description can be found.



**Table 3**  
Overview of the applied steps during data processing.

Step	Action	Description
1	Integration of relevant emission lines.	At least 2–3 emission lines were selected for major rock forming elements and relevant REEs (Table 2). The spectra were integrated with an integration window of 0.05 nm around the peaks.
2	Generation of the LIBS hyperspectral data cube.	Conversion of the extracted emission lines into an ENVI compatible format. This allows an easy visualization of spatially resolved element distribution maps.
3	Normalization to correct for shot-to-shot variations.	For every pixel, the integrated intensity of every single emission line was divided by the cumulated intensity of all extracted emission lines.
4	The k-means algorithm was used to separate clasts and rock matrix in the mapping.	K-means clustering was applied to all pixels using the normalized intensities of the selected set of emission lines. The optimal number of clusters was defined using the PBM-Index.
5	Smoothing to remove noise and falsely classified single pixel.	A moving window of size 5 × 5 was applied. The central pixel was assigned to the majority of all 25 pixels in the window.
6	Extraction of mineral rims.	A one-pixel buffer zone was calculated around every clast. The buffer zones correspond to mineral rims.
7	Establishment of a matrix-matched intensity limit, above which REE-rich areas can be detected.	Mineral rims without any REE enrichment were used to define a matrix-matched background signal to calculate an intensity limit for REEs. This intensity limit was transferred to all pixel of the formerly separated matrix (Step 3).

### 3. Results and discussion

#### 3.1. Microprobe reference measurements

Table 4 shows the average composition of REE-carbonates, apatite, pyrochlore, and carbonate minerals based on the microprobe measurements. Quantitative microprobe measurements on 33 different spots covering rock matrix and rims have shown that REE-carbonates are the main carrier for REEs in this sample (Table 4). Cerium, La and Nd show highest concentrations of up to 24.4, 15.4 and 9.2 wt%, respectively. Praseodymium, Sm and Gd are present but only to minor extends with values of 3.5, 1.2 and 3.2 wt%. Yttrium was also measured, but did not show concentrations higher than 0.8 wt%. The average size of the observed REE-carbonates is around 25 µm, whereas some aggregates cover larger areas. Measurements of pyrochlore revealed Nb contents as high as 50.2 wt%, whereas  $\sum$ REE contents were about 1.5 wt%.

Fig. 3 shows Back Scattered Electron (BSE) images, in which the weight of an element correlates with its optical appearance. Heavier elements, like REEs, visually appear brighter on screen and therefore, the BSE image is a first indication of the possible REE distribution in the sample. However, Ba, which is another heavy element present in Storkwitz samples, may be optically indistinguishable from REEs. Therefore, quantitative electron microprobe point measurements were performed as described in the Materials and methods section to obtain an accurate chemical composition of several REE-carbonates.

Fig. 3 shows that REE enrichments occur in small aggregates, either at mineral rims (A and B) or at porosities or microfractures in the rock matrix (C and D). This is in accordance with other carbonatite REE deposits, where REE bearing minerals were also found as thin layers at

grain boundaries or in fracture zones (Deng et al., 2017; Lottermoser, 1990). Twenty-one of the 33 measured REEs were analysed at mineral rims, the 12 remaining spots cover microfractures or porosities in the matrix. Average element concentrations of both areas are displayed in Table 4. The measured spots shown in Fig. 3 are representative for all REE-rich spots in the thin sections shown in Fig. 1A.

To estimate REE concentrations in other carbonates and possible carrier minerals (e.g. apatite and pyrochlore), several spots have been measured covering these minerals. Forty-six of these spots cover apatite and 28 pyrochlore. Overall, 109 other carbonates were measured, divided into ankerite, dolomite and calcite. The averaged results are shown in Table 4. Apatite shows average Ce concentrations of 0.69 wt%, pyrochlore of 0.96 wt%. Averaged contents for all other carbonates are 0.03 wt%. Silicate clasts were measured as well but did not contain any La, Ce, Pr, Nd, Sm, or Gd.

#### 3.2. LIBS measurements and clustering

Fig. 4 shows an RGB-image of normalized intensities representing the major rock forming elements Si, Ca and K as red, green and blue, respectively. This reveals two main types of clasts, one with mixed intensities of Si and K (purple) and one only containing Ca (green), missing the silicate components completely. Looking at these three elements, the rock matrix mostly consists of Ca with varying proportions of Si and K, making it distinguishable from both the carbonate clasts and the Si and K rich silicate clasts. Fig. 4 also shows a close-up of the intensity distribution of emission line La I – 394.91 nm for areas where the thin sections were taken. Since the extracted Ce and Nd emission lines show distinctively lower peak intensities than the La lines (Fig. 2), we focused on La to detect pixel enriched in REEs.

To make sure that the observed low intensities of Ce and Nd are not due to poorly chosen emission lines, we closely investigated several REE-rich spectra from different spots in the measured area. Thereto, the REE-rich spectra were compared to emission lines of REEs proposed by other researchers and to the NIST database (e.g. Abedin et al., 2011; Bhatt et al., 2018; Kramida et al., 2017). Unfortunately, no alternative interference-free emission lines with significantly higher intensities for Ce and Nd could be found. Additionally, we closely examined LIBS spectra of the CGL 111 reference standard, containing 2.90 wt% Ce, 1.93 wt% La and 8800 ppm Nd. The chosen emission lines for REEs (Table 2) were detected most conveniently and with similar intensities as displayed in Fig. 2. La on the other hand shows sufficiently strong emission lines useful for the determination of REE-carbonates and we therefore focused on La as a tracer for REE-carbonates. Strong La lines were also found in earlier LIBS measurements of REEs on hydrothermal ores by Fabre et al. (2018) or homogeneous minerals by Gaft et al. (2019).

The highest La intensities were found at the rims of clasts as well as in distinct particles related to porosities and microfractures that are loosely distributed in the rock matrix (Fig. 4). Most rims are often not fully surrounded by pixel enriched in La, and some mineral rims do not show any enrichment at all. These LIBS-based observations correspond very well to the microprobe-based observations shown in Fig. 3. Cerium, Nd, Pr, Sm, and Gd show coinciding results for most of the selected emission lines. However the noise for these REEs seems extensively higher, which is due to lower element concentrations and/or weaker emission lines.

It is important to notice that the average REE-carbonate in the investigated sample is significantly smaller than the laser spot size of 200 µm of the LIBS system used (Fig. 3). If the average size of a REE-carbonate is about 25 µm (Fig. 3), the resulting contribution of a REE-carbonate to the overall spectral emission of a pixel featuring a REE-carbonate is roughly 13%. The residual 87% emission is based on the surrounding material, which dilutes the peak intensity of the REE emission lines and increases the heterogeneity of REE-rich spectra. This makes it difficult to use a simple signal-to-noise ratio for the 2D mapping, with which REE-rich spectra could be found. Establishing a

**Table 4**

Quantitative chemical composition of REE-carbonates, apatite, pyrochlore and carbonate minerals as measured with the microprobe. The numbers give both the average chemical composition as well as the measured natural compositional variation based on microprobe measurements of n different minerals.

	REE-carbonate (n = 33)	REE-carbonate at rims (n = 21)	REE-carbonate in matrix (n = 12)	Carbonate (n = 109)	Apatite (n = 46)	Pyrochlore (n = 28)
Si wt%	0.4 ± 0.5	0.5 ± 0.6	0.2 ± 0.3	0.0 ± 0.1	0.0 ± 0.1	0.2 ± 0.5
Ti wt%	–	–	–	–	0.0 ± 0.1	1.4 ± 0.5
Al wt%	–	–	–	–	0.0 ± 0.0	0.0 ± 0.0
Fe wt%	0.5 ± 0.5	0.7 ± 0.5	0.3 ± 0.3	3.2 ± 2.6	0.1 ± 0.1	0.6 ± 0.6
Mn wt%	0.0 ± 0.0	0.1 ± 0.0	0.0 ± 0.0	1.4 ± 1.4	0.1 ± 0.0	0.1 ± 0.0
Mg wt%	0.1 ± 0.1	0.1 ± 0.1	0.1 ± 0.1	6.7 ± 4.3	0.1 ± 0.1	0.0 ± 0.0
Ca wt%	5.6 ± 2.9	5.0 ± 1.6	6.6 ± 4.1	27.0 ± 8.0	37.3 ± 1.3	10.6 ± 1.5
F wt%	7.0 ± 1.1	7.3 ± 0.5	6.4 ± 0.5	0.0 ± 0.0	2.7 ± 0.6	4.1 ± 0.8
Na wt%	–	–	–	–	0.3 ± 0.1	4.7 ± 0.9
K wt%	–	–	–	–	0.0 ± 0.1	0.0 ± 0.0
Cl wt%	–	–	–	–	0.0 ± 0.0	0.0 ± 0.0
P wt%	–	–	–	–	17.6 ± 1.1	0.0 ± 0.0
S wt%	–	–	–	–	0.0 ± 0.0	0.0 ± 0.0
Ba wt%	–	–	–	–	0.0 ± 0.0	0.1 ± 0.0
C wt%	4.3 ± 0.7	4.3 ± 0.3	4.5 ± 1.0	12.5 ± 0.3	–	–
Ce wt%	24.4 ± 1.8	24.4 ± 1.6	24.3 ± 2.2	0.03 ± 0.1	0.7 ± 0.4	1.0 ± 0.2
Dy wt%	0.0 ± 0.0	0.0 ± 0.0	0.0 ± 0.0	0.00 ± 0.0	–	–
Gd wt%	3.2 ± 0.3	3.2 ± 0.2	3.2 ± 0.3	0.00 ± 0.0	–	–
La wt%	14.8 ± 2.5	15.4 ± 1.5	13.8 ± 3.4	0.01 ± 0.0	0.3 ± 0.3	0.3 ± 0.1
Nb wt%	–	–	–	–	0.0 ± 0.0	47.9 ± 2.5
Nd wt%	8.3 ± 1.8	7.8 ± 0.8	9.2 ± 2.6	0.01 ± 0.0	0.3 ± 0.2	0.3 ± 0.1
Pr wt%	2.3 ± 0.3	2.3 ± 0.1	2.5 ± 0.5	0.00 ± 0.0	0.1 ± 0.2	0.1 ± 0.0
Sm wt%	1.1 ± 0.4	1.0 ± 0.1	1.2 ± 0.5	0.00 ± 0.0	0.1 ± 0.0	0.0 ± 0.0
Sr wt%	0.4 ± 0.1	0.5 ± 0.1	0.4 ± 0.1	0.6 ± 0.5	1.8 ± 1.0	1.2 ± 0.7
Ta wt%	–	–	–	–	0.0 ± 0.1	0.4 ± 0.6
Y wt%	–	–	–	–	0.1 ± 0.1	0.0 ± 0.0
Zn wt%	0.0 ± 0.0	0.00 ± 0.0	0.0 ± 0.0	0.0 ± 0.1	0.0 ± 0.0	0.0 ± 0.0
Zr wt%	–	–	–	–	0.0 ± 0.0	0.2 ± 0.2
O wt%	23.7 ± 2.4	23.3 ± 1.2	24.3 ± 3.6	50.0 ± 1.2	37.4 ± 1.5	26.8 ± 0.7
Total wt%	96.1 ± 2.7	95.8 ± 2.3	97.0 ± 3.0	101.4 ± 1.8	99.0 ± 2.2	100.0 ± 3.9

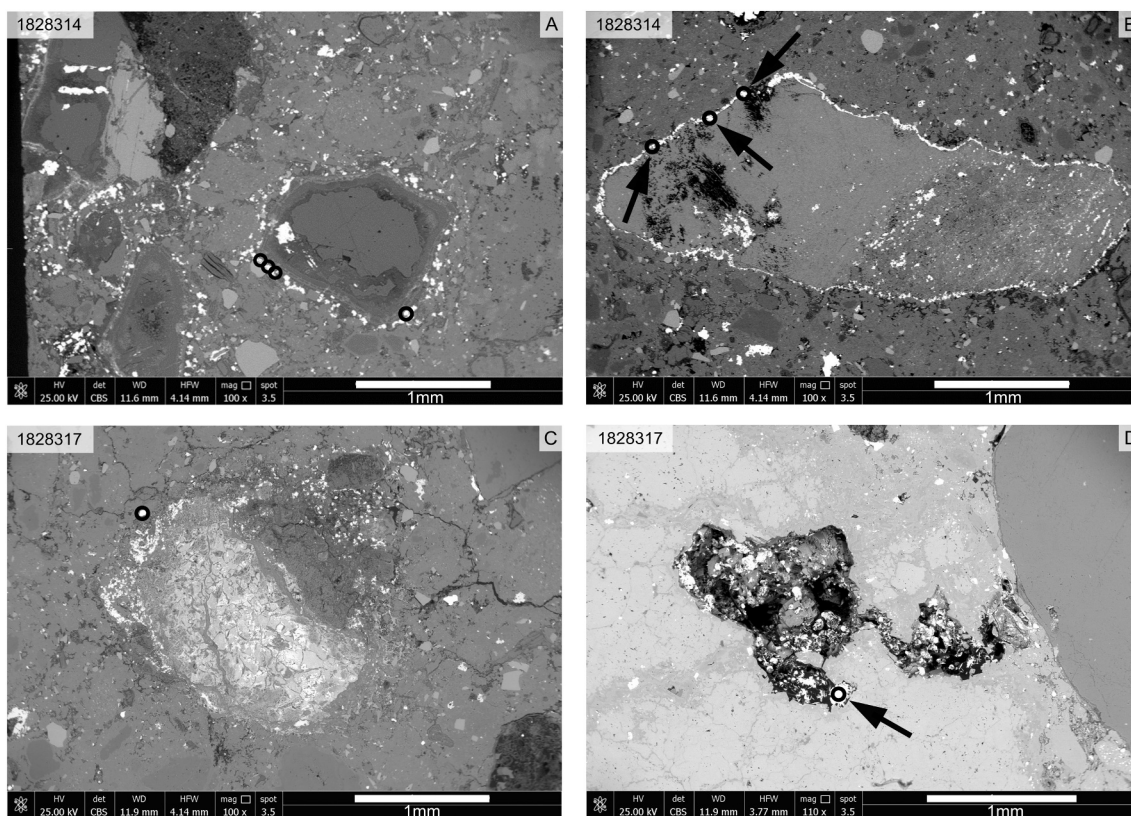


**Fig. 3.** BSE-images showing typical examples of analysed microprobe spots in the thin sections 1828314 and 1829317. Black circles indicate the measured spots. REE minerals show a bright colour. (A) and (B) are representative for areas where mineral rims are enriched in REEs, (C) and (D) show occurrences in elevated porosity or microfractures in the matrix.



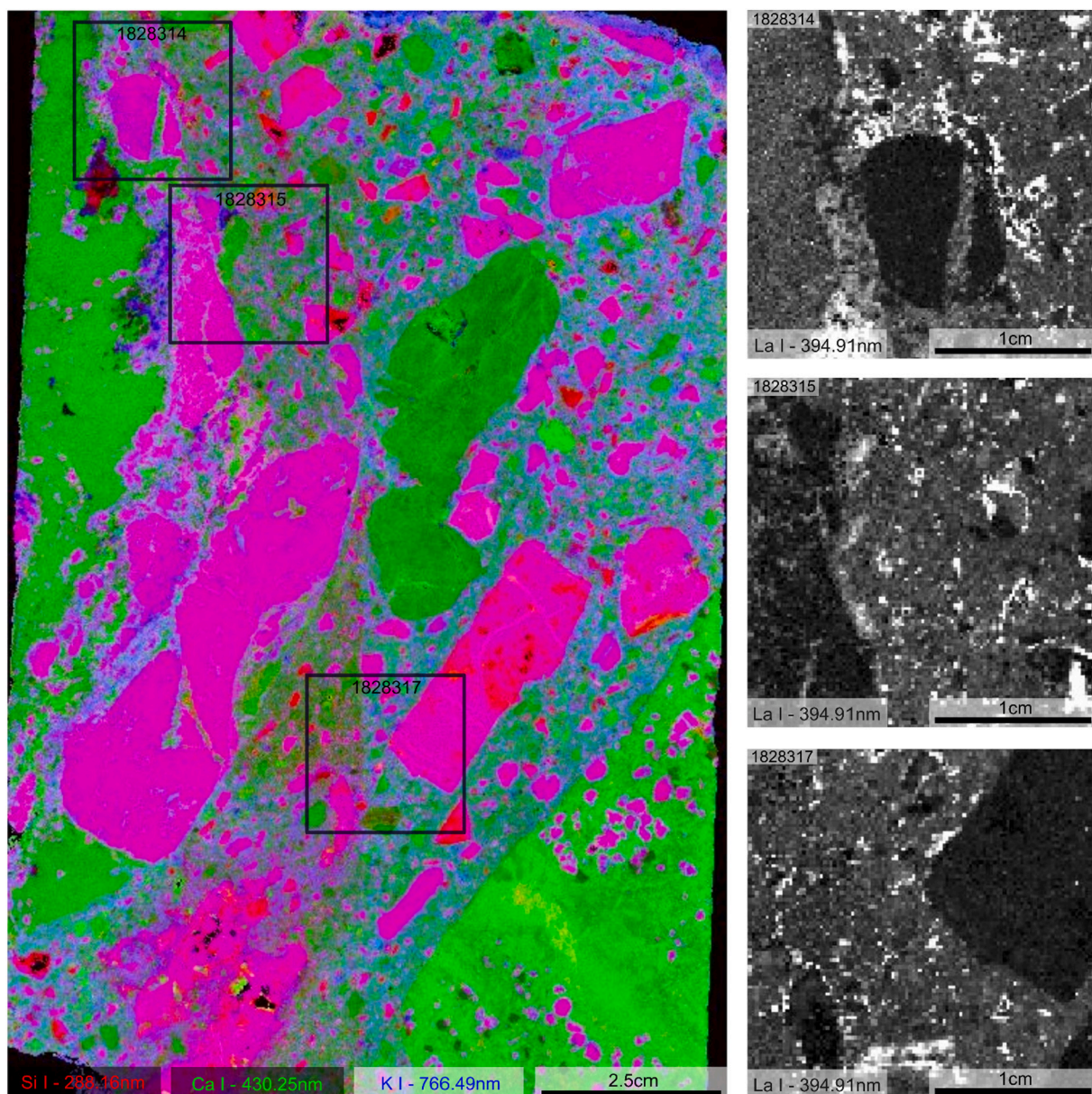


**Fig. 4.** RGB-image with Si I 288.16 nm (red), Ca I 430.25 nm (green) and K I 766.49 nm (blue) on the left to illustrate the chemical differences between Si- and K-rich silicates, Ca-rich carbonatitic clasts and the matrix in between. A more detailed overview of the areas corresponding to the thin sections is presented for La I 394.91 nm with enrichments at the rims of some clasts or in the matrix. (For interpretation of the references to colour in this figure legend, the reader is referred to the web version of this article.)

normalized intensity limit despite the spectral heterogeneity and the varying contributions of REE-carbonates to a spectrum is discussed in Section 3.3.

Fig. 5A shows the result of k-means clustering using the three predefined cluster centres. In the following sections, the three identified clusters are referred to as Silicate-Cluster, Carbonatite-Cluster, and Matrix-Cluster, corresponding to silicates, carbonates and the rock matrix. The main drivers of the separation can be traced more precisely by looking at Fig. 6, which shows the mean intensities of the selected emission lines for the three clusters.

The Silicate-Cluster shows - in comparison with the Carbonatite-Cluster and the Matrix-Cluster - the highest emission intensities for Na, K, and Al, and the lowest emission intensities for Ca, Mg, Sr and Ba. This result is consistent with the mineralogy of the silicate clasts, which are generally rich in K and Na (i.e. richterite, aegirine, alkali feldspar and phlogopite) but poor in Ca, Mg, Sr, and Ba. The Carbonatite-Cluster

shows the highest emission intensities for Ca, Mg, and Sr, and the lowest emission intensities for Na, K, and Al. Minerals of the Carbonatite-Cluster are indeed enriched in these elements (i.e. dolomite, ankerite and calcite). The Matrix-Cluster shows intermediate emission intensities for Na, K, Ca, Mg, and Sr and is representative for a mixture of very fine grained silicates and carbonates, which explains why the intensities are in between those from the Silicate- and the Carbonatite-Cluster.

However, there are no particular emission lines that are distinctively unique to a specific cluster and therefore, no single element can be used for a clear separation. Accordingly, the results based on clustering only (Fig. 5A) show a lot of scattering in the data and reveal relatively diffuse class boundaries. The moving window step, however, effectively removed the scattering in the data and created sharp boundaries between the three classes (Fig. 5B). Fig. 5C shows the resulting rims that were calculated on the basis of Fig. 5B.

For validation purposes, Fig. 5B is compared to the LIBS element



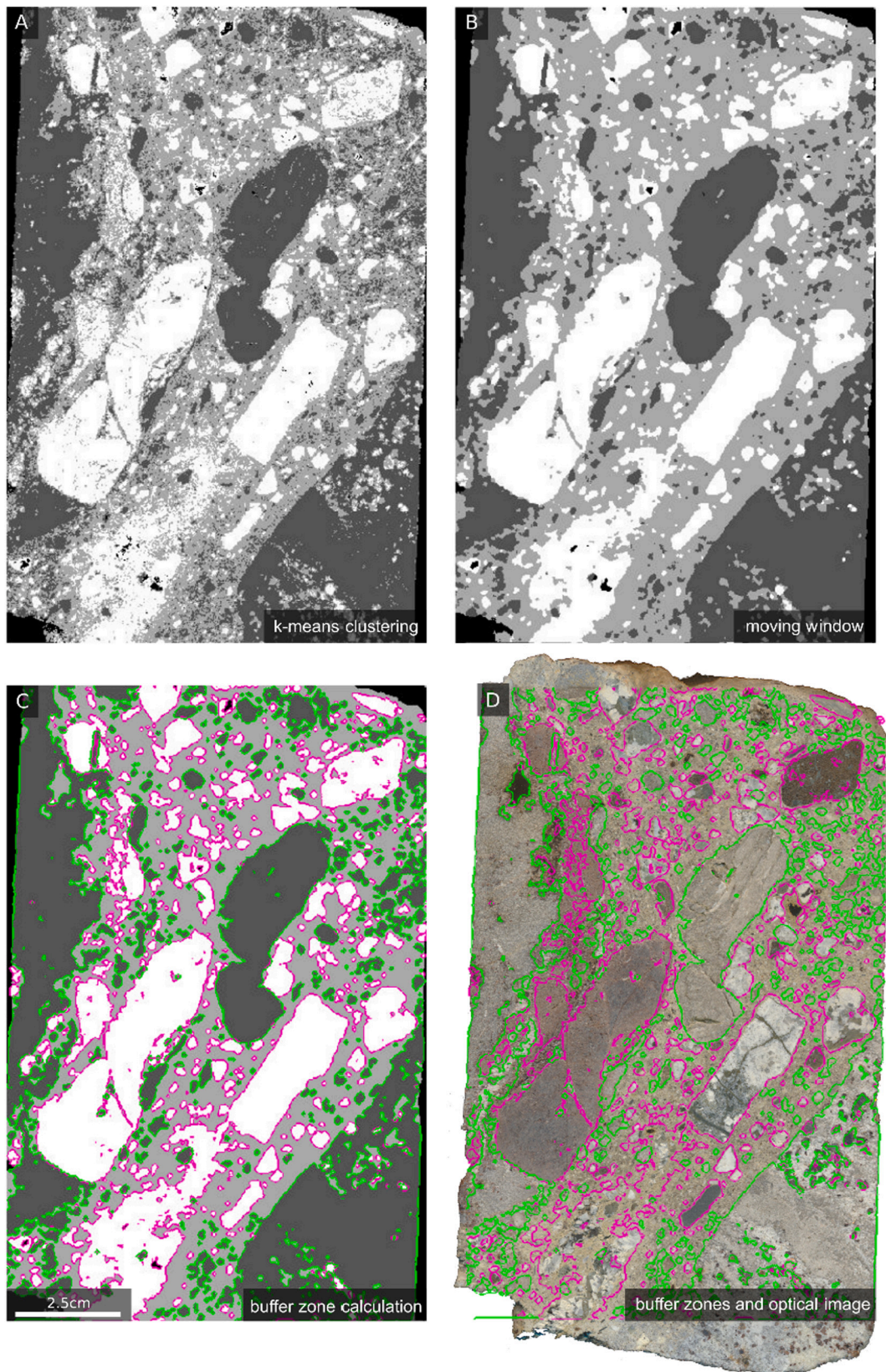


**Fig. 5.** (A) Result of k-means clustering using three predefined cluster centres. (B) Results after the application of a  $5 \times 5$  moving window. (C) Calculated buffer zones around silicate (pink) and carbonate clasts (green). (D) Buffer zones over optical image for validation. (For interpretation of the references to colour in this figure legend, the reader is referred to the web version of this article.)

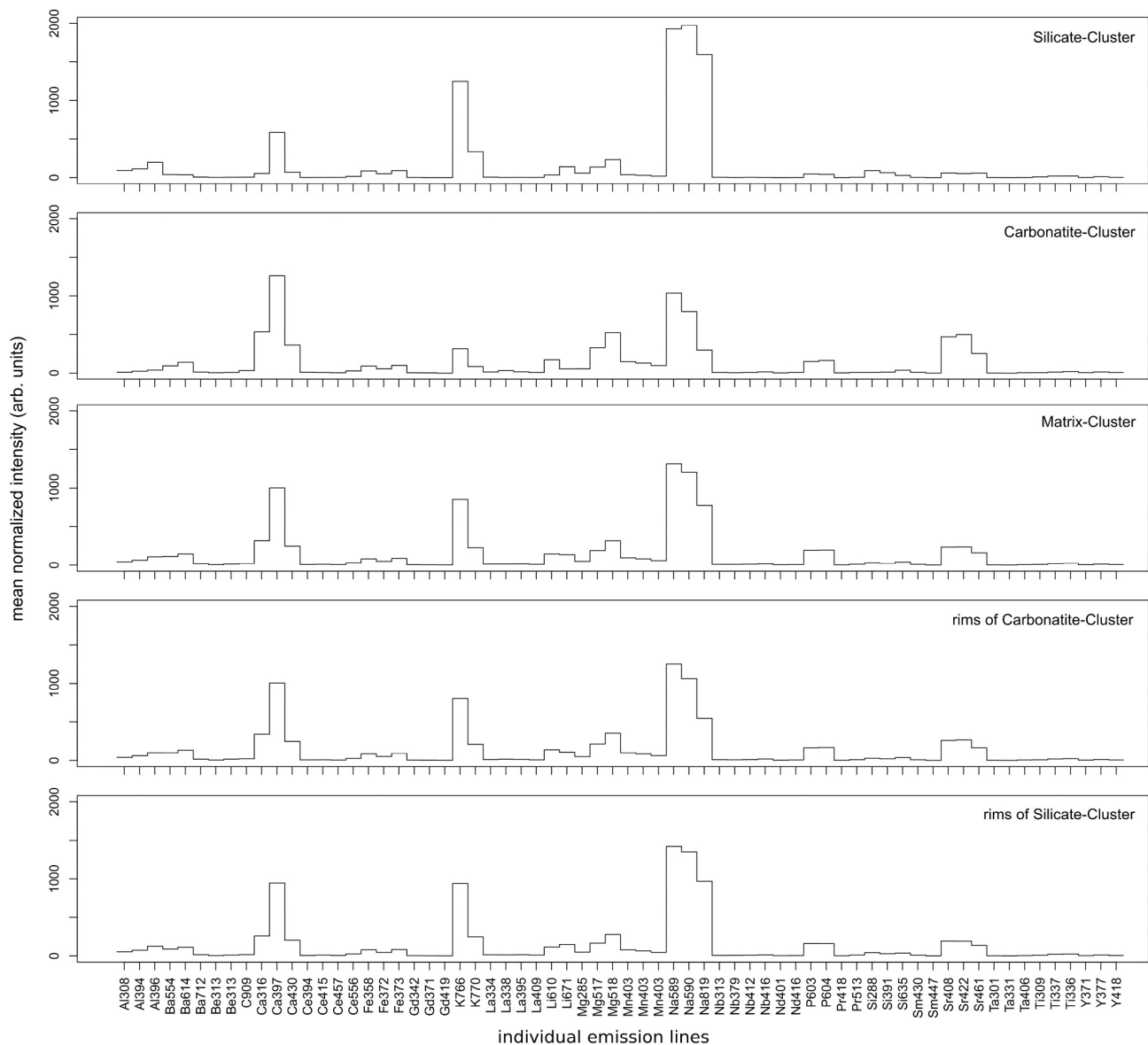


**Fig. 6.** Mean normalized intensities of individual emission lines for the three clusters produced with k-means clustering as well as for the extracted rims of the carbonate and silicate clasts.

mapping for Si288-Ca430-K766 (Fig. 4) and to the optical image of the physical sample (Fig. 5D). A distinct quantitative validation of the quality of the classification result is hardly possible, as the only reference is geological knowledge of the optical sample assisted by element mappings (e.g. Fig. 4). Therefore, the results of Fig. 5B were carefully compared to changes in texture (Fig. 5D) as well as to colour differences in the element mapping (Fig. 4). The differences in colour (Fig. 4) and texture (Fig. 5D) are generally in good agreement with the class distribution shown in Fig. 5B. Therefore, we assume that the final classification results shown in Fig. 5B are valid.

Nevertheless, clustering may fail when the chemical composition of the clasts becomes too similar to the composition of the matrix. This seems only to apply to small parts of the lower left area of the investigated sample. These areas are assigned to the Silicate-Cluster, whereas Fig. 4 and the optical image (Fig. 5D) indicate that they belong to the Matrix-Cluster instead.

### 3.3. Raster analysis and possibilities to calculate a matrix-matched intensity limit for REEs

Applying the moving window results in Fig. 5B. Single pixel are clearly integrated in their surroundings, and noise introduced by wrongly classified pixel is reduced. Fig. 5B was subsequently used to calculate buffer zones around the Silicate-Cluster and the Carbonatite-Cluster, respectively. Overall, the Silicate-Cluster comprises 484 and the Carbonatite-Cluster 446 clasts. Accordingly, as many buffer zones were calculated and extracted (Fig. 5C). The buffer zones correspond to mineral rims with a width of 200  $\mu\text{m}$ .

The mean normalized intensities for rim pixel around the Silicate- and Carbonatite-Clusters are very similar to those of pixel belonging to the Matrix-Cluster (Fig. 6). This indicates that the chemical composition of rim pixel is very similar to pixel belonging to the Matrix-Cluster and independent of the surrounding clast. Based on these similarities, we assume similar chemically induced matrix effects for pixel around rims as for pixel belonging to the Matrix-Cluster. This finding is relevant for the calculation and application of matrix-matched intensity limits, above which REE-carbonates can be detected with the LIBS system used.

The calculation of a Limit of Detection (LOD) usually requires matrix-specific blank measurements (Ismail et al., 2004; Windom and Hahn, 2009). However, these are not easily available for our measurements, which is a common problem for LIBS measurements on heterogeneous geological samples (Fabre, 2020). Since there is no possibility to create a sample with the same matrix and varying but known concentrations of La, LOD calculations normally used in analytical chemistry cannot be applied here. Instead, a set of representative matrix-specific blanks was selected directly from the LIBS mapping as described in Section 3.3.1.

### 3.3.1. Creating a matrix-matched blank measurement with normal distribution

In order to calculate an intensity limit above which REE-carbonates can be detected, a suitable blank measurement representing rims and Matrix-Cluster is needed. The blank dataset should be matrix-matched and not enriched in La. Consequently, the required matrix-matched dataset should show a Gaussian distribution towards the La intensity. Fig. 7A shows that the density plot for La II 333.75 nm for all pixel belonging to the Matrix-Cluster is indeed heavily shifted towards high La intensities.

A matrix-matched blank dataset, therefore, was prepared based on the finding that several mineral rims are not enriched in La at all. This was observed in the LIBS mapping and in the microprobe measurements. Since chemically induced matrix effects for pixel belonging to rims and Matrix-Cluster are likely to be similar (Fig. 6), an intensity limit calculated for each group can be used for the other group as well. Thereto, all 930 rims were analysed separately and if only a single rim-pixel was assigned as an outlier for any emission line of La by showing a value greater than the median plus three times the median absolute deviation, all pixel of this rim were dismissed. Although this dataset shows significant improvement concerning a normal distribution, a shift towards the right can still be observed (Fig. 7A).

To eliminate the skewness, outliers were removed using the Z-score (Spiegel et al., 2013). This approach was applied for both datasets displayed in Fig. 7. Since extreme outliers influence the mean and the standard deviation largely, an iterative approach was used starting with a Z-score of 10. It was decreased by one during every step until a Z-score of 3 was reached. After each iteration, we validated the distribution of the remaining dataset based on visible skewness and potential outliers

causing an offset. At a Z-score of 3, which corresponds to a confidence level of 99.73% (Spiegel et al., 2013), the treated subset of pixel from rims not enriched in La displayed a normal distribution for every emission line of La. The pixel of the Matrix-Cluster, however, still displayed a visible shift towards higher La intensities (Fig. 7B).

Since a Z-score of 10 is very high, only extreme outliers are found during this iteration step. For pixel of the Matrix-Cluster, only 80 pixel were found above this value. This number increased with decreasing Z-score to 3979 pixel above a Z-score of 3. For rim pixel without enrichment, the first outlier was found and removed at a Z-score of 5, whereas the major amount of outlier in this dataset were removed at a Z-score of 3. The specific Z-scores for pixel from the Matrix-Cluster and pixel from rims not enriched in La are indicated in Fig. 7A with grey lines and dotted black lines, respectively. Fig. 7 only shows La II 333.75 nm, but the other extracted La lines displayed similar behaviour. Therefore, the rim-based dataset shown in Fig. 7B was used as a matrix-matched blank measurement to calculate the normalized intensity limit.

### 3.3.2. Using the normalized intensity limit to detect enriched pixel in the Matrix-Cluster

Using the mean plus three times the standard deviation as suggested for LOD calculations by the IUPAC (1978), La II 333.75 nm shows a normalized intensity limit of 23.9, La II 338.09 nm of 33.5, La I 394.91 nm of 28.1 and La II 408.67 nm of 19.2. The different intensity limits for different lines are a result of the intensity distribution of the background signal around each individual emission line. Furthermore, the extracted emission lines of La are not equally strong (Fig. 2). Because of matrix issues, it is important to notice that these normalized intensity limits are valid for pixel belonging to the rims and to the Matrix-Cluster only.

These normalized intensity limits are subsequently used to find areas enriched in La (and thereto REE-carbonates) in the mineral rims and in the Matrix-Cluster. Only if a pixel shows intensity values greater than the limits calculated in 3.3.2 for all emission lines of La simultaneously, it is treated as enriched. This way, the risk of errors due to element interferences in single La emission lines is reduced. Fig. 8 illustrates the importance of using several emission line intensity limits simultaneously. The proportion of La II 338.09 nm to La I 394.91 nm of all enriched points depicted in grey show a near linear trend with increasing intensities observed in both lines. Considering all points

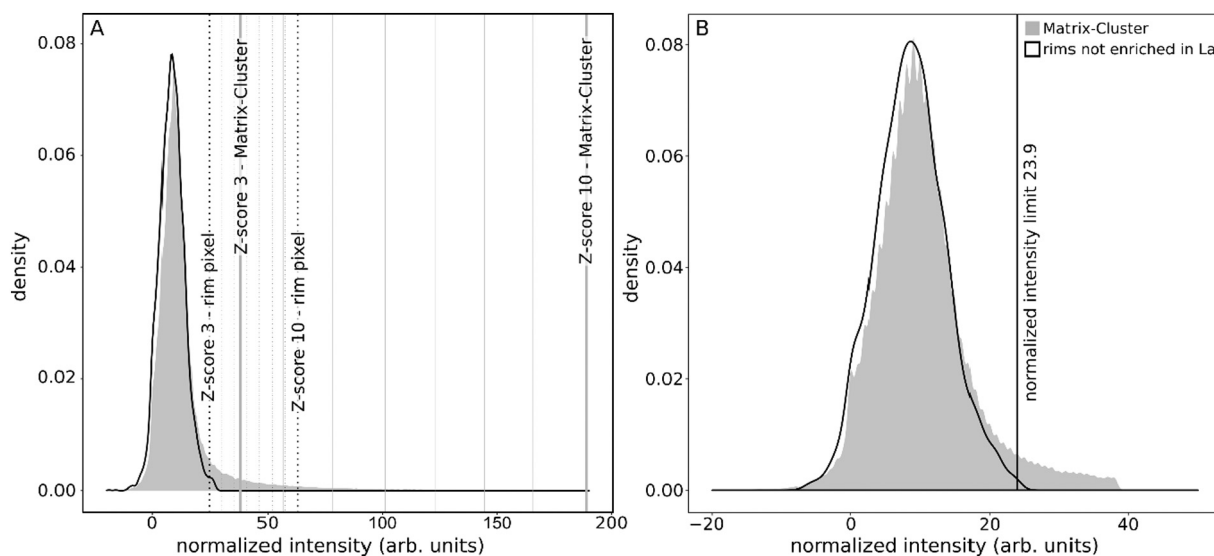
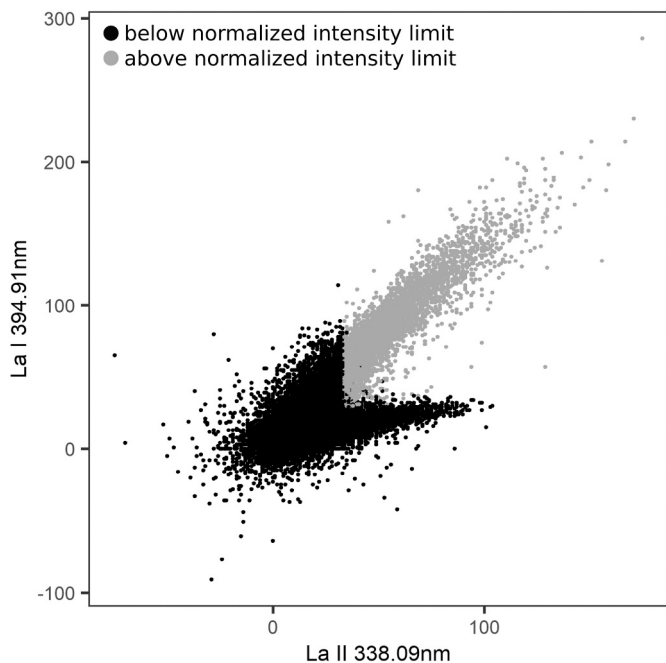


Fig. 7. (A) Density plot of La II 333.75 nm for all 159,694 pixel belonging to the Matrix-Cluster (grey) and the 5211 pixel from rims not enriched in La (black line). Initial and final Z-scores for both subsets are highlighted with vertical lines. (B) Density plot of the same emission line and the remaining 150,618 pixel from the Matrix-cluster and 5161 pixel from rims not enriched in La after outlier removal using the iterative Z-score. The vertical line indicates the intensity limit of 23.9 for La II 333.75 nm calculated with the 5161 pixel from rims not enriched in La after outlier removal. The application of Z-scores for outlier removal is explained in the text.





**Fig. 8.** Correlation between La I 394.91 nm and La II 338.09 nm intensities for the Matrix-Cluster. The dots represent all pixel that belong to the Matrix-Cluster, the grey dots only those above the normalized intensity limit of both emission lines.

shown in Fig. 8, several points form a second trend in which increasing values of La I 338.09 nm correspond to near constant values of La I 394.09 nm, indicating that La enrichment cannot be detected looking at only one emission line. Overall, 1.4% of all pixel of the complete mapping are above the intensity limit of every extracted La emission line and therefore found to be enriched in REEs.

### 3.4. Comparison of REE enrichments observed with LIBS and $\mu$ -EDXRF

Fig. 9 shows the spatial distribution of REE enrichments in the investigated core as obtained with LIBS as well as with  $\mu$ -EDXRF. The LIBS-data show La-enrichments as a tracer for REE-carbonates around mineral rims and in the rock-matrix. Only pixel above the calculated intensity limits (Section 3.3.2) were considered to be enriched in La. The  $\mu$ -EDXRF data show pixel that were excited in both Ce  $L\alpha$  and Nd  $L\alpha$ . Since La  $L\alpha$  could not be measured with  $\mu$ -EDXRF, the combination of Ce  $L\alpha$  and Nd  $L\alpha$  was used as a tracer for REE-carbonates instead. This combination also effectively prevents interferences with e.g. Ba. The  $\mu$ -EDXRF measurement was resized from an original resolution of  $4850 \times 5450$  pixel to the size of the LIBS measurement ( $495 \times 755$  pixel). Pixel aggregation was used to calculate the value for the resulting pixel, i.e. the mean of all pixel that were merged together. Fig. 9 (middle) shows the percentage of REE enriched pixel in every row of the image for both the LIBS- and the  $\mu$ -EDXRF-based images.

In general, the LIBS-based results seem to be consistent with the  $\mu$ -EDXRF-based results. The  $\mu$ -EDXRF mapping shows similar spots of enrichment as the LIBS analysis. Mostly, Ce  $L\alpha$  and Nd  $L\alpha$  are present at rims of minerals and fill porosities inside the matrix. Although an identical trend can be observed for the LIBS-based and EDXRF-based results (Fig. 9 middle), when looking more closely at the data, minor differences can also be seen. The small shift along the intensity profile

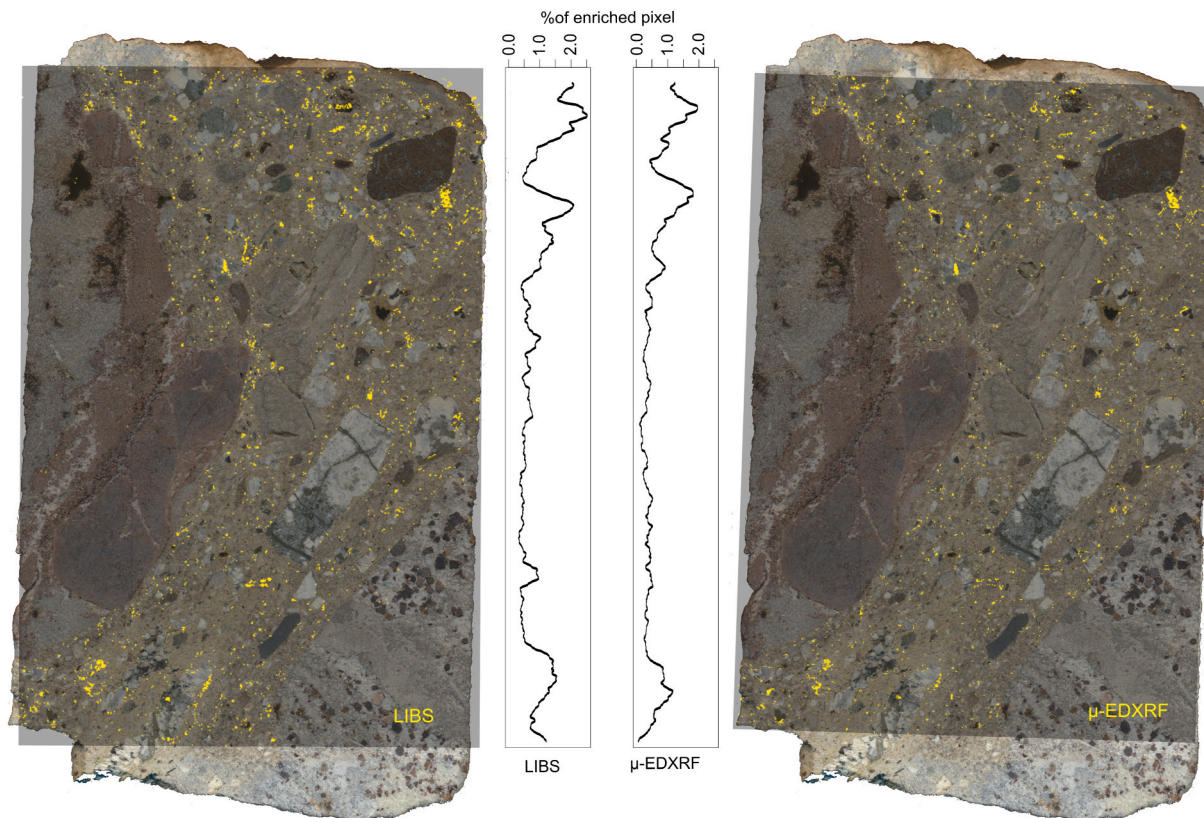


**Fig. 9.** Comparison of pixel enriched in La with LIBS (left) and Ce  $L\alpha$  and Nd  $L\alpha$  with  $\mu$ -EDXRF (right). The detected pixel are highlighted in yellow. The two diagrams in the centre correspond to the percentage of enriched pixel per row of the LIBS and the  $\mu$ -EDXRF measurement, respectively. (For interpretation of the references to colour in this figure legend, the reader is referred to the web version of this article.)

could eventually sign for a small horizontal misalignment of the measurement area affecting the more morphology-sensitive  $\mu$ -EDXRF measurement. Since irradiation is performed at a  $51^\circ$ , a change in focal distance would drive the signal slightly out of the pixel under investigation showing some degree of signal attenuation.

A proper validation of the results would require space-resolved REE reference measurements with an analytical technology capable of quantitative REE analysis, which is a subject for future research. The  $\mu$ -EDXRF data are not precise enough for a quantitative validation due to the rather short spectral acquisition time of 2 ms that resulted in relatively bad signal statistics, the spectral interferences described above, the absence of a calibration, and also the differences in sampling depth between LIBS and EDXRF. Whereas the LIBS craters are about  $50\ \mu\text{m}$  in depth (Meima and Rammlair, 2020), the  $\mu$ -EDXRF signal saturation depth for Ce  $L\alpha$  and Nd  $L\alpha$  could vary between a few tens of  $\mu\text{m}$  and a few hundreds of  $\mu\text{m}$ . This depends on the bulk density at an investigated pixel, which is the density of the sum of phases diluted by porosity over the excited volume. Typical penetration depths for 90% escape are in the range of 5–500  $\mu\text{m}$ , depending on the atomic number of the analyte element and composition of the sample (Markowicz, 2011).

### 3.5. General discussion

#### 3.5.1. Mass balance calculation for REE-carbonates and other REE carrier minerals

Microprobe measurements (Table 4) have revealed that small concentrations of REEs also occur in apatite and pyrochlore ( $\sim 0.3\ \text{wt}\%$  La and  $\sim 1.0\ \text{wt}\%$  Ce), as well as in different carbonate minerals ( $\sim 0.01\ \text{wt}\%$  La and  $\sim 0.03\ \text{wt}\%$  Ce). These concentrations were below the limit of detection for our LIBS system, as the corresponding LIBS spectra did not show any La and/or Ce peaks. Despite these relatively low concentrations, an unknown amount of REEs could be missed with LIBS simply due to the large area that is covered especially by the carbonate minerals. Therefore, a mass balance calculation was performed to explore the significance of the different REE carrier minerals.

Table 5 shows the assumptions for the mass balance calculation as well as the resulting  $\sum\text{REE}_2\text{O}_3$  concentrations for the identified REE carrier minerals. The  $\sum\text{REE}_2\text{O}_3$  represents the total amount of REE expressed as oxide. The  $\sum\text{REE}_2\text{O}_3$  weight percentages were calculated using specific REE concentrations for each carrier mineral, mineral densities, and the area percent covered by each carrier mineral on the analysed sample surface. The  $\sum\text{REE}_2\text{O}_3$  concentrations in the different carrier minerals are based on the microprobe measurements (Table 4). Densities were taken from (Barthelmy, 2012). With respect to the carbonate minerals, the average density for dolomite, ankerite and calcite was taken. For REE-carbonates, bastnaesite was adopted as the main carrier and therefore its density was employed. To determine the area percent covered by apatite, pyrochlore, and the different carbonates (dolomite, ankerite and calcite), the in-house tool “petrographic analyst” described by Nikonow et al., 2019 was used on the  $\mu$ -EDXRF

**Table 5**

Assumptions and resulting weight percentages of  $\sum\text{REE}_2\text{O}_3$  in the measured sample for all minerals containing significant amounts of  $\text{REE}_2\text{O}_3$ .

	$\sum\text{REE}_2\text{O}_3$ in mineral wt%	Mineral area %	Density $\text{g}/\text{cm}^3$	$\sum\text{REE}_2\text{O}_3$ in sample wt%
Carbonate minerals	0.06 <sup>a</sup>	42 <sup>b</sup>	2.9 <sup>d</sup>	0.04
Apatite	1.8 <sup>a</sup>	4 <sup>b</sup>	3.2 <sup>d</sup>	0.1
Pyrochlore	1.9 <sup>a</sup>	0.3 <sup>b</sup>	4.1 <sup>d</sup>	0.01
REE-carbonate	63.3 <sup>a</sup>	0.4 <sup>c</sup>	5.0 <sup>d</sup>	0.7

<sup>a</sup> REE concentrations based on microprobe measurements (Table 4).

<sup>b</sup> Area % based on mineral classification of  $\mu$ -EDXRF data (see text).

<sup>c</sup> Based on LIBS intensity limits calculated for all La emission lines (see text).

<sup>d</sup> Mineral densities taken from Barthelmy (2012).

measurement data. The size of these carrier minerals is usually greater than the LIBS spot size of  $200\ \mu\text{m}$ . The effect of internal porosity on the signal was ignored since high variation is assumed to occur pixel per pixel.

REE-carbonates, however, are distinctively smaller than the spot size of the LIBS instrument. Therefore, the calculated amount of La-enriched pixel (1.4%) does not represent the amount of pure REE-carbonates. However, the average La content of the La-enriched pixel could be estimated on the basis of Fig. 8 as described below. Considering the observed La emission intensities shown in Fig. 8, it is assumed that the greatest La intensity corresponds to a pixel-volume that is fully covered by a relative pore free REE-carbonate aggregate and therefore corresponds to the REE concentration for pure REE-carbonate (Table 4). The lowest La intensities on the other hand, are close to the detection limit. The La detection limit of our instrument was assumed to be 1 wt%, which is in between the La concentrations in apatite and pyrochlore, which could not be detected with our LIBS system, and the La concentrations in standard CGL 111, which could indeed be detected with our LIBS system. Based on a linear equation to fit all La intensities into concentrations, the average pixel above the La intensity limit (Section 3.3.1) would represent a La concentration of  $\sim 4\ \text{wt}\%$ . Accordingly, 27% of the 1.4% pixel above the La intensity limit would refer to pure REE-carbonates. Table 5, therefore, includes 0.4 area % for pure REE-carbonates.

According to Table 5, the investigated sample would contain a total of 0.8 wt% REE oxides, of which 0.1 wt% are present in apatite and 0.7 wt% in REE-carbonates. Therefore, about 88% of total REE oxides were detected with LIBS in this study.

Goodenough et al. (2016) combined data of different REE deposits and their expected REE concentrations. For the Storkwitz diatreme, a total of 0.45% REE oxides were reported. Additionally, Niegisch et al. (2020) determined  $\text{REE}_2\text{O}_3$  concentrations of 0.64 wt% for the upper part of the Storkwitz carbonatite. Notably, Niegisch et al. (2020) found monazite to be one of the REE bearing minerals, but it was not present in our investigated sample. Assuming that the central complex, out of which the investigated sample was taken, contains higher amounts of REE oxides than the neighbouring parts of the diatreme, 0.8 wt% seems to be a reasonable result. Since the highly enriched carbonates represent the last stage of hydrothermal alteration, additional information can be obtained by the REE partitioning in primary or secondary phases. The ratio bulk to secondary enrichment might be a key parameter for applying the proper mineral treatment strategy for REE mineral recovery.

#### 3.5.2. Clustering and possible improvements for REE detection with LIBS

Clustering is a viable option for unsupervised classification of classes with similar matrices in LIBS mappings of heterogeneous geological samples. Rompanen et al. (2017) have shown that there are more algorithms, such as Singular Value Decomposition (SVD) that can be used for this task. Creating matrix-matched subsets for geochemically similar spectra of a heterogeneous sample could also be performed using supervised algorithms (e.g. Random Forest, Support Vector Machines or feedforward Artificial Neural Networks) instead of the unsupervised clustering that was applied in this paper. One major advantage of clustering is exactly this unsupervised nature, which allows a separation into chemically similar areas solely based on emission line intensities without any prior knowledge.

In contrast, a supervised classification approach would require detailed prior knowledge on material characteristics. This is because in a supervised scenario representative subsets for training have to be selected carefully beforehand. For an accurate classification of pixel enriched in REEs, this subset needs to cover a wide variety of pixels containing different proportions of REE-carbonates mixed with surrounding material as well as pixel without any REE enrichment. These pixels must in turn cover the different clasts and matrix to be representative for the heterogeneity of the sample. However, when such prior



knowledge is available, supervised methods may find application on other cores of the same lithology. We have tested a supervised approach using as prior knowledge the results obtained in this paper. Thereto, we used the pixels enriched in REEs as input for a supervised random forest classification. Treating all other pixels as not enriched in REEs and using 2/3 of each pixel set as training, we were able to classify over 80% of testset pixel enriched in REEs correctly.

Clustering proved to be a useful pre-step prior to separate matrix-matched spectra. Working only with matrix-matched spectra (i.e. similar LIBS matrices) also helps to overcome interferences within emission lines (Fabre et al., 2018), which is important for heterogeneous materials that cover various elements of interest. It is especially important for the detection of rare earth elements, since emission lines of REEs show significant spectral interferences and mostly occur only in low concentrations in geological material (Gaft et al., 2019). Using several emission lines of the same element simultaneously minimizes the risk of spectral interferences in heterogeneous material even further.

Clustering is also a useful pre-step prior to quantification. Quantifying LIBS data is mostly done with homogeneous reference samples of similar matrix and known concentrations, which are difficult to obtain for heterogeneous samples (Fabre et al., 2018). Calibration free LIBS (CF-LIBS) allows the quantification based on the measured LIBS spectrum directly, but several time consuming calculations have to be applied in the process (Pagnotta et al., 2018). Quantifying only selected areas or even only single spectra of interest reduces the time needed greatly. Therefore, combining the extraction methods described in this paper with CF-LIBS could be a promising approach to quantify REEs directly from the LIBS measurement.

Due to the small size of REE-carbonates (Fig. 3) compared to the size of the LIBS laser spot, REEs are mixed with surrounding material and pores, and only minerals with sufficiently high concentrations of REEs can be detected with certainty. Therefore, the method described here only works well for punctual REE enrichments but fails to detect small concentrations diffusively distributed. Without punctual enrichment, REE oxide contents are not high enough to be above the detection limit for LIBS, which is the reason why we were not able to detect Ce or La sufficiently in apatite and pyrochlore. Low concentrations of REEs in the material show lower LIBS intensities in general (Bhatt et al., 2018; Gaft et al., 2019). Bhatt et al. (2018) showed that measuring samples in noble gas atmosphere increases the spectral line intensity of REEs and Gaft et al. (2019) were able to detect molecular lines of LaO and YO although only minor concentrations of both elements were present. These enhancements could enable the detection of REEs appearing in small concentrations in mappings of carbonatite REE deposits. Additionally, reducing the laser spot size could further reduce dilution, but multiply measurement times.

Several known major REE deposits are geologically similar to Storkwitz. They are associated with carbonatites, and different minerals show REE enrichments (Deng et al., 2017; Kanazawa and Kamitani, 2006). Additionally, REE bearing minerals precipitate at grain boundaries and fractures, and some, especially those related to hydrothermal overprint show stronger REE enrichment than potential precursor minerals (Deng et al., 2017), and we can therefore assume that the method proposed here can be applied for other major REE deposits as well, providing insight into REE portioning due to redistributions.

LIBS drill core scanners allow detailed 1D or 2D detection of various zones of REE enrichment in complete drill cores, with results available during or right after measurement on the site of mining. Traditional methods usually rely on meter wise sampling where information of the spatial distribution of REE enrichment is mostly lost and sections of interest need to be shipped to a laboratory for further analysis. Nevertheless, concentrations for the mapped surface can only roughly be estimated with LIBS based on a semi-quantitative basis and the result is prone to 3D effects since the surface of the material may not resemble the bulk concentrations. Therefore, LIBS drill core analysis adds valuable spatial information, but cannot fully replace traditional lab

analyses.

#### 4. Conclusion

This paper presents a novel approach for the spatially resolved detection of REE enrichments in highly heterogeneous geological material from the Storkwitz carbonatite based on scanning LIBS.

We have shown that a LIBS-based analysis of REE enrichments in highly heterogeneous geological material requires detailed spatially resolved LIBS measurements of sufficiently large surface areas. Furthermore, we have shown that k-means clustering and raster analysis offer opportunities to reduce sample heterogeneity by automatically separating different matrices and extracting REE-relevant features. Mineral clasts and rock matrix were divided using k-means clustering, before raster analysis was performed to extract all points that belong to mineral rims. Finally, we have successfully tested the application of matrix-matched intensity limits above which REE-carbonates can be detected with LIBS. Following the LOD approach, these limits are based on blank measurements, which consist of REE-free matrix-matched subsets of the data. Four strong La emission lines (La II 333.75 nm, La II 338.09 nm, La I 394.91 nm and La II 408.67 nm), which show distinctively higher emission intensities than the Ce and Nd emission lines, were detected with our LIBS system and used as a tracer for REE-carbonates.

About 88% of the REE-enrichments in the investigated drill core seem to occur as pure REE-carbonates. These REE-carbonates, which most prominently occur at the rims of different minerals or in areas of elevated porosity or microfractures that are loosely distributed in the matrix of the breccia, were successfully detected with scanning LIBS. The LIBS-based results could be confirmed with  $\mu$ -EDXRF and microprobe reference measurements. According to the microprobe measurements, low concentrations of additional REEs were found in the minerals apatite and pyrochlore ( $\sim 1.6$  wt%  $\sum$ REE), as well as diffusively distributed in normal carbonates ( $\sim 0.05$  wt%  $\sum$ REE). A mass balance calculation shows how the different REE-carrier minerals contribute to the total amount of REEs in the investigated sample.

#### CRediT authorship contribution statement

Simon Müller: Conceptualization, Methodology, Software, Investigation, Formal analysis, Writing - Original Draft, Visualization, Data Curation.

Jeannet Meima: Conceptualization, Methodology, Writing - Review & Editing, Funding acquisition, Project administration, Supervision.

Dieter Rammlair: Conceptualization, Methodology, Writing - Review & Editing.

#### Declaration of competing interest

The authors declare that they have no known competing financial interests or personal relationships that could have appeared to influence the work reported in this paper.

#### Acknowledgements

We thank Dr. Lapp and the Geological Survey of Saxony (LfULG) for providing the Storkwitz drill cores and additional information from former investigations. Furthermore, we thank Christian Wöhr, Simon Goldmann and Marleen Künker for the electron microprobe measurements as well as Martin Schodlok for fruitful discussions on REE distributions in the Storkwitz carbonatite. We thank David Mory and Sven Merk for fruitful discussions on LIBS technology. We also thank the anonymous reviewers for their very helpful remarks on the manuscript.

## Funding

This work was funded by the Federal Ministry for Economic Affairs and Energy (Grant Nr. ZF4441001SA7).

## References

- Abedin, K.M., Haider, A.F.M.Y., Rony, M.A., Khan, Z.H., 2011. Identification of multiple rare earths and associated elements in raw monazite sands by laser-induced breakdown spectroscopy. *Optics Laser Technol.* 43, 45–49 (doi:0.1016/j.optlastec.2010.05.003).
- AtomTrace, 2020. Periodic Table | AtomTrace [WWW Document]. URL: <https://www.atomtrace.com/elements-database/>. (Accessed 9 April 2020).
- Barthelmy, D., 2012. Mineralogy Database [WWW Document]. URL: <http://www.webmineral.com/>. (Accessed 20 February 2020).
- Bhatt, C.R., Jain, J.C., Gouguet, C.L., McIntyre, D.L., Singh, J.P., 2018. Determination of rare earth elements in geological samples using laser-induced breakdown spectroscopy (LIBS). *Appl. Spectrosc.* 72, 114–121 (doi:0.1177/0003702817734854).
- Brown, J.D., 1991.  $\phi(\rho z)$  equations for quantitative analysis. In: Heinrich, K.F.J., Newbury, D.E. (Eds.), *Electron Probe Quantitation*. Springer US, Boston, MA, pp. 77–81 (doi:0.1007/978-1-4899-2617-3.5).
- Charalampides, G., Vatalis, K.I., Apostolos, B., Ploutarch-Nikolas, B., 2015. Rare earth elements: industrial applications and economic dependency of Europe. *Proc. Econ. Finan.* 24, 126–135 (doi:0.1016/S2212-5671(15)00630-9).
- Cremers, D., Radziemski, L., 2013. *Handbook of Laser-Induced Breakdown Spectroscopy*, Second edition (doi:0.1002/9781118567371).
- Croudace, I.W., Rindby, A., Rothwell, R.G., 2006. ITRAX: description and evaluation of a new multi-function X-ray core scanner. In: Geological Society, London, Special Publications, 267, pp. 51–63 (doi:0.1144/GSL.SP.2006.267.01.04).
- Death, D.L., Cunningham, A.P., Pollard, L.J., 2008. Multi-element analysis of iron ore pellets by laser-induced breakdown spectroscopy and principal components regression. *Spectrochim. Acta B Atom. Spectrosc.* 63, 763–769 (doi:0.1016/j.sab.2008.04.014).
- Deng, M., Xu, C., Song, W., Tang, H., Liu, Y., Zhang, Q., Zhou, Y., Feng, M., Wei, C., 2017. REE mineralization in the Bayan Obo deposit, China: evidence from mineral paragenesis. *Ore Geol. Rev.* 91, 100–109 (doi:0.1016/j.oregeorev.2017.10.018).
- Desgraupes, B., 2018. *clusterCrit: Clustering Indices*.
- Díaz, D., Hahn, D.W., Molina, A., 2017. Quantification of gold and silver in minerals by laser-induced breakdown spectroscopy. *Spectrochim. Acta B Atom. Spectrosc.* 136, 106–115 (doi:0.1016/j.sab.2017.08.008).
- Effenberger, A., Scott, J., 2010. Effect of atmospheric conditions on LIBS spectra. *Sensors* 10, 4907–4925 (doi:0.3390/s100504907).
- El Haddad, J., de Lima Filho, E.S., Vanier, F., Harhira, A., Padiou, C., Sabsabi, M., Wilkie, G., Blouin, A., 2019. Multiphase mineral identification and quantification by laser-induced breakdown spectroscopy. *Miner. Eng.* 134, 281–290 (doi:0.1016/j.mineng.2019.02.025).
- El-Saeid, R.H., Abdel-Salam, Z., Pagnotta, S., Palleschi, V., Harith, M.A., 2019. Classification of sedimentary and igneous rocks by laser induced breakdown spectroscopy and nanoparticle-enhanced laser induced breakdown spectroscopy combined with principal component analysis and graph theory. *Spectrochim. Acta B Atom. Spectrosc.* 158, 105622 (doi:0.1016/j.sab.2019.05.011).
- Fabre, C., 2020. Advances in laser-induced breakdown spectroscopy analysis for geology: a critical review. *Spectrochim. Acta B Atom. Spectrosc.* 166, 105799 (doi:0.1016/j.sab.2020.105799).
- Fabre, C., Devismes, D., Moncayo, S., Pelascini, F., Trichard, F., Lecomte, A., Bousquet, B., Cauzid, J., Motto-Ros, V., 2018. Elemental imaging by laser-induced breakdown spectroscopy for the geological characterization of minerals. *J. Anal. Atom. Spectrom.* 33, 1345–1353 (doi:0.1039/C8JA00048D).
- Gaft, M., Raichlin, Y., Pelascini, F., Panzer, G., Motto Ros, V., 2019. Imaging rare-earth elements in minerals by laser-induced plasma spectroscopy: molecular emission and plasma-induced luminescence. *Spectrochim. Acta B Atom. Spectrosc.* 151, 12–19 (doi:0.1016/j.sab.2018.11.003).
- Galbács, G., 2015. A critical review of recent progress in analytical laser-induced breakdown spectroscopy. *Anal. Bioanal. Chem.* 407, 7537–7562 (doi:0.1007/s00216-015-8855-3).
- Ganguli, R., Cook, D.R., 2018. Rare earths: a review of the landscape. *MRS Energy Sustain.* 5, E9 (doi:0.1557/mre.2018.7).
- Goodenough, K.M., Schilling, J., Jonsson, E., Kalvig, P., Charles, N., Tuduri, J., Deady, E. A., Sadeghi, M., Schiellerup, H., Müller, A., Bertrand, G., Arvanitidis, N., Eliopoulos, D.G., Shaw, R.A., Thrane, K., Keulen, N., 2016. Europe's rare earth element resource potential: an overview of REE metallogenetic provinces and their geodynamic setting. *Ore Geol. Rev.* 72, 838–856 (doi:0.1016/j.oregeorev.2015.09.019).
- Goodenough, K.M., Wall, F., Merriman, D., 2018. The rare earth elements: demand, global resources, and challenges for resourcing future generations. *Nat. Resour. Res.* 27, 201–216 (doi:0.1007/s11053-017-9336-5).
- Gottfried, J.L., Harmon, R.S., De Lucia, F.C., Miziolek, A.W., 2009. Multivariate analysis of laser-induced breakdown spectroscopy chemical signatures for geomaterial classification. *Spectrochim. Acta B Atom. Spectrosc.* 64, 1009–1019 (doi:0.1016/j.sab.2009.07.005).
- Gottlieb, C., Millar, S., Grothe, S., Wilsch, G., 2017. 2D evaluation of spectral LIBS data derived from heterogeneous materials using cluster algorithm. *Spectrochim. Acta B Atom. Spectrosc.* 134, 58–68 (doi:0.1016/j.sab.2017.06.005).
- Haavisto, O., Kauppinen, T., Häkkinen, H., 2013. Laser-induced breakdown spectroscopy for rapid elemental analysis of drillcore. *IFAC Proc.* 46, 87–91 (doi:0.3182/20130825-4-US-2038.00047).
- Hahn, D.W., Omenetto, N., 2010. Laser-induced breakdown spectroscopy (LIBS), part I: review of basic diagnostics and plasma–particle interactions: still-challenging issues within the analytical plasma community. *Appl. Spectrosc.* 64, 335A–336A (doi:0.1366/000370210793561691).
- Hahn, D.W., Omenetto, N., 2012. Laser-induced breakdown spectroscopy (LIBS), part II: review of instrumental and methodological approaches to material analysis and applications to different fields. *Appl. Spectrosc.* 66, 347–419 (doi:0.1366/11-06574).
- Harmon, R.S., Russo, R.E., Hark, R.R., 2013. Applications of laser-induced breakdown spectroscopy for geochemical and environmental analysis: a comprehensive review. *Spectrochim. Acta B Atom. Spectrosc.* 87, 11–26 (doi:0.1016/j.sab.2013.05.017).
- Hijmans, R.J., 2019. *raster: Geographic Data Analysis and Modeling*.
- Ismail, M.A., Imam, H., Elhassan, A., Younis, W.T., Harith, M.A., 2004. LIBS limit of detection and plasma parameters of some elements in two different metallic matrices. *J. Anal. Atom. Spectrom.* 19, 489 (doi:0.1039/b315588a).
- IUPAC, 1978. Nomenclature, symbols, units and their usage in spectrochemical analysis. II. Data interpretation analytical chemistry division. *Spectrochim. Acta B* 33, 241–245 (doi:0.1016/0584-8547(78)80044-5).
- Kanazawa, Y., Kamitani, M., 2006. Rare earth minerals and resources in the world. *J. Alloys Compound* 408–412, 1339–1343 (doi:0.1016/j.jallcom.2005.04.033).
- Khajehzadeh, N., Kauppinen, T.K., 2015. Fast mineral identification using elemental LIBS technique. *IFAC-PapersOnLine* 48, 119–124 (doi:0.1016/j.ifacol.2015.10.089).
- Kramida, A., Ralchenko, Y., Reader, J., NIST ASD Team, 2017. *NIST Atomic Spectra Database* [WWW Document]. URL: <https://physics.nist.gov/PhysRefData/ASD/LIBS/libsum.html>. (Accessed 9 April 2020).
- Krüger, J.C., Romer, R.L., Kämpf, H., 2013. Late Cretaceous ultramafic lamprophyres and carbonates from the Delitzsch Complex, Germany. *Chemical Geology* 353, 140–150 (doi:0.1016/j.chemgeo.2012.09.026).
- Kuhn, K., Meima, J.A., 2019. Characterization and economic potential of historic tailings from gravity separation: implications from a mine waste dump (Pb-Ag) in the Harz Mountains Mining District, Germany. *Minerals* 9, 303 (doi:0.3390/min9050303).
- Kuhn, K., Meima, J.A., Rammlair, D., Ohlendorf, C., 2016. Chemical mapping of mine waste drill cores with laser-induced breakdown spectroscopy (LIBS) and energy dispersive X-ray fluorescence (EDXRF) for mineral resource exploration. *J. Geochem. Explor.* 161, 72–84 (doi:0.1016/j.gexplo.2015.11.005).
- Liang, L., Sun, Y., Yao, Z., Liu, Y., Wu, F., 2012. Evaluation of high-resolution elemental analyses of Chinese loess deposits measured by X-ray fluorescence core scanner. *CATENA* 92, 75–82 (doi:0.1016/j.catena.2011.11.010).
- Lottermoser, B.G., 1990. Rare-earth element mineralisation within the Mr. Weld carbonate laterite, Western Australia. *Lithos* 24, 151–167 (doi:0.1016/0024-4937(90)90022-5).
- Lui, S.-L., Koujelev, A., 2011. Accurate identification of geological samples using artificial neural network processing of laser-induced breakdown spectroscopy data. *J. Anal. Atom. Spectrom.* 26, 2419 (doi:0.1039/c1ja10093a).
- MacQueen, J., 1967. Some methods for classification and analysis of multivariate observations. In: *Fifth Berkeley Symposium on Mathematical Statistics and Probability*. University of California Press, Berkeley, Calif., pp. 281–297. Presented at the Proceedings of the Fifth Berkeley Symposium on Mathematical Statistics and Probability, Volume 1: Statistics.
- Markowicz, A., 2011. An overview of quantification methods in energy-dispersive X-ray fluorescence analysis. *Pramana* 76, 321–329 (doi:0.1007/s12043-011-0045-z).
- Martin, M., Martin, R.C., Allman, S., Brice, D., Wymore, A., Andre, N., 2015. Quantification of rare earth elements using laser-induced breakdown spectroscopy. *Spectrochim. Acta B Atom. Spectrosc.* 114, 65–73 (doi:0.1016/j.sab.2015.10.005).
- Meima, J.A., Rammlair, D., 2020. Investigation of compositional variations in chromitite ore with imaging laser induced breakdown spectroscopy and spectral angle mapper classification algorithm. *Chem. Geol.* 532, 119376 (doi:0.1016/j.chemgeo.2019.119376).
- Miziolek, A.W., Palleschi, V., Schechter, I. (Eds.), 2006. *Laser Induced Breakdown Spectroscopy*. Cambridge University Press, Cambridge (doi:0.1017/CBO9780511541261).
- Nadeau, O., Cayer, A., Pelletier, M., Stevenson, R., Jébrak, M., 2015. The Paleoproterozoic Montviel carbonate-hosted REE–Nb deposit, Abitibi, Canada: geology, mineralogy, geochemistry and genesis. *Ore Geol. Rev.* 67, 314–335 (doi:0.1016/j.oregeorev.2014.12.017).
- Niegijs, M., Kamradt, A., Borg, G., 2020. Geochemical and Mineralogical Characterization of the REE-Mineralisation in the Upper Zone of the Storkwitz Carbonate Complex From Drill Core SES-1/2012 91.
- Nikonov, W., Rammlair, D., 2016. Risk and benefit of diffraction in energy dispersive X-ray fluorescence mapping. *Spectrochim. Acta B Atom. Spectrosc.* 125, 120–126 (doi:0.1016/j.sab.2016.09.018).
- Nikonov, W., Rammlair, D., Meima, J.A., Schodlok, M.C., 2019. Advanced mineral characterization and petrographic analysis by  $\mu$ -EDXRF, LIBS, HSI and hyperspectral data merging. *Miner. Petrol.* 113, 417–431 (doi:0.1007/s00710-019-00657-z).
- Pagnotta, S., Grifoni, E., Legnaioli, S., Lezzner, M., Lorenzetti, G., Palleschi, V., 2015. Comparison of brass alloys composition by laser-induced breakdown spectroscopy and self-organizing maps. *Spectrochim. Acta B Atom. Spectrosc.* 103–104, 70–75 (doi:0.1016/j.sab.2014.11.008).
- Pagnotta, S., Lezzner, M., Ripoll-Seguer, L., Hidalgo, M., Grifoni, E., Legnaioli, S., Lorenzetti, G., Poggialini, F., Palleschi, V., 2017. Micro-laser-induced breakdown spectroscopy (Micro-LIBS) study on ancient Roman mortars. *Appl. Spectrosc.* 71, 721–727 (doi:0.1177/0003702817695289).

- Pagnotta, S., Lezzerini, M., Campanella, B., Gallelo, G., Grifoni, E., Legnaioli, S., Lorenzetti, G., Poggialini, F., Raneri, S., Safi, A., Palleschi, V., 2018. Fast quantitative elemental mapping of highly inhomogeneous materials by micro-laser-induced breakdown spectroscopy. *Spectrochim. Acta B Atom. Spectrosc.* 146, 9–15 (doi:0.1016/j.sab.2018.04.018).
- Pagnotta, S., Lezzerini, M., Campanella, B., Legnaioli, S., Poggialini, F., Palleschi, V., 2020. A new approach to non-linear multivariate calibration in laser-induced breakdown spectroscopy analysis of silicate rocks. *Spectrochim. Acta B Atom. Spectrosc.* 166, 105804 (doi:0.1016/j.sab.2020.105804).
- Pakhira, M.K., Bandyopadhyay, S., Maulik, U., 2004. Validity index for crisp and fuzzy clusters. *Pattern Recogn.* 37, 487–501 (doi:0.1016/j.patcog.2003.06.005).
- Pořízka, P., Demidov, A., Kaiser, J., Keivanian, J., Gornushkin, I., Panne, U., Riedel, J., 2014. Laser-induced breakdown spectroscopy for in situ qualitative and quantitative analysis of mineral ores. *Spectrochim. Acta B Atom. Spectrosc.* 101, 155–163 (doi:0.1016/j.sab.2014.08.027).
- R Core Team, 2018. R: A Language and Environment for Statistical Computing. R Foundation for Statistical Computing, Vienna, Austria.
- Romppanen, S., Häkkinen, H., Kaski, S., 2017. Singular value decomposition approach to the yttrium occurrence in mineral maps of rare earth element ores using laser-induced breakdown spectroscopy. *Spectrochim. Acta B Atom. Spectrosc.* 134, 69–74 (doi:0.1016/j.sab.2017.06.002).
- Ross, P.-S., Bourke, A., Fresia, B., 2013. A multi-sensor logger for rock cores: methodology and preliminary results from the Matagami mining camp, Canada. *Ore Geol. Rev.* 53, 93–111 (doi:0.1016/j.oregeorev.2013.01.002).
- Sanghavi, H.K., Jain, J., Bol'shakov, A., Lopano, C., McIntyre, D., Russo, R., 2016. Determination of elemental composition of shale rocks by laser induced breakdown spectroscopy. *Spectrochim. Acta B Atom. Spectrosc.* 122, 9–14 (doi:0.1016/j.sab.2016.05.011).
- Seifert, W., 2000. Compositional variation in apatite, phlogopite and other accessory minerals of the ultramafic Delitzsch complex, Germany: implication for cooling history of carbonatites. *Lithos* 53, 81–100 (doi:0.1016/S0024-4937(00)00010-4).
- Sirven, J.-B., Sallé, B., Mauchien, P., Lacour, J.-L., Maurice, S., Manhès, G., 2007. Feasibility study of rock identification at the surface of Mars by remote laser-induced breakdown spectroscopy and three chemometric methods. *J. Anal. Atom. Spectrom.* 22, 1471 (doi:0.1039/b704868h).
- Smith, P.L., Heise, C., Kurucz, R.L., 2001. Atomic spectral line database from CD-ROM 23 of R. L. Kurucz [WWW Document]. URL: <https://www.cfa.harvard.edu/amp/ampdata/kurucz23/sekur.html>. (Accessed 9 April 2020).
- Spiegel, M.R., Schiller, J.J., Srinivasan, R.A., 2013. *Schaum's Outline of Probability and Statistics*, Fourth edition. McGraw-Hill, New York, Chicago, San Francisco, Lisbon, London, Madrid, Mexico City, Milan, New Delhi, San Juan, Seoul, Singapore, Sydney, Toronto.
- Steinhaus, H., 1956. Sur la division des corps matériels en parties. *Bull. Acad. Polon Sci.* 801–804.
- Takahashi, T., Thornton, B., 2017. Quantitative methods for compensation of matrix effects and self-absorption in laser induced breakdown spectroscopy signals of solids. *Spectrochim. Acta B Atom. Spectrosc.* 138, 31–42 (doi:0.1016/j.sab.2017.09.010).
- Tucker, J.M., Dyar, M.D., Schaefer, M.W., Clegg, S.M., Wiens, R.C., 2010. Optimization of laser-induced breakdown spectroscopy for rapid geochemical analysis. *Chem. Geol.* 277, 137–148 (doi:0.1016/j.chemgeo.2010.07.016).
- U.S. Army Research Laboratory, 2010. LIBS Elemental Database – CCDC Army Research Laboratory [WWW Document]. URL: <https://www.arl.army.mil/who-we-are/directorates/wmrd/librs/>. (Accessed 7 September 2020).
- Vendramin, L., 2010. Relative clustering validity criteria: a comparative overview. *Stat. Anal. Data Mining* 3, 27.
- Wang, W., Zhang, Y., 2007. On fuzzy cluster validity indices. *Fuzzy Sets Syst.* 158, 2095–2117 (doi:0.1016/j.fss.2007.03.004).
- Wang, X., Motto-Ros, V., Panczer, G., De Ligny, D., Yu, J., Benoit, J.M., Dussossoy, J.L., Peugeot, S., 2013. Mapping of rare earth elements in nuclear waste glass–ceramic using micro laser-induced breakdown spectroscopy. *Spectrochim. Acta B Atom. Spectrosc.* 87, 139–146 (doi:0.1016/j.sab.2013.05.022).
- Wiens, R.C., Maurice, S., Lasue, J., Forni, O., Anderson, R.B., Clegg, S., Bender, S., Blaney, D., Barraclough, B.L., Cousin, A., Deflores, L., Delapp, D., Dyar, M.D., Fabre, C., Gasnault, O., Lanza, N., Mazoyer, J., Melikechi, N., Meslin, P.-Y., Newsom, H., Ollila, A., Perez, R., Tokar, R.L., Vaniman, D., 2013. Pre-flight calibration and initial data processing for the ChemCam laser-induced breakdown spectroscopy instrument on the Mars Science Laboratory rover. *Spectrochim. Acta B Atom. Spectrosc.* 82, 1–27 (doi:0.1016/j.sab.2013.02.003).
- Windom, B.C., Hahn, D.W., 2009. Laser ablation—laser induced breakdown spectroscopy (LA-LIBS): a means for overcoming matrix effects leading to improved analyte response. *J. Anal. Atom. Spectrom.* 24, 1665 (doi:0.1039/b913495f).
- Yuan, L., Chen, Xiaojing, Lai, Y., Chen, Xi, Shi, Y., Zhu, D., Li, L., 2018. A novel strategy of clustering informative variables for quantitative analysis of potential toxic element in *Tegillarca granosa* using laser-induced breakdown spectroscopy. *Food Anal. Methods* 11, 1405–1416 (doi:0.1007/s12161-017-1096-7).
- Zuo, R., 2013. ITRAX: a potential tool to explore the physical and chemical properties of mineralized rocks in mineral resource exploration. *J. Geochem. Explor.* 132, 149–155 (doi:0.1016/j.gexplo.2013.06.010).

### 3. Mineral classification of lithium-bearing pegmatites based on laser-induced breakdown spectroscopy: Application of semi-supervised learning to detect known minerals and unknown material

**Simon Müller<sup>1\*</sup>, Jeannet A. Meima<sup>1</sup>**

<sup>1</sup>Federal Institute for Geosciences and Natural Resources, Stilleweg 2, 30650 Hannover, Germany

\*Corresponding author. E-mail address: [Jeannet.Meima@bgr.de](mailto:Jeannet.Meima@bgr.de)

#### KEYWORDS

Laser-Induced Breakdown Spectroscopy (LIBS), Linear Discriminant Analysis (LDA), One-Class Support Vector Machines (OC-SVM), Spodumene pegmatite, Unknown matrix

DOI: 10.1016/j.sab.2022.106370



# Mineral classification of lithium-bearing pegmatites based on laser-induced breakdown spectroscopy: Application of semi-supervised learning to detect known minerals and unknown material

Simon Müller<sup>\*</sup>, Jeannet A. Meima

Federal Institute for Geosciences and Natural Resources, Stilleweg 2, 30655 Hannover, Germany

## ARTICLE INFO

### Keywords:

Laser-induced breakdown spectroscopy (LIBS)  
Linear discriminant analysis (LDA)  
One-class support vector machines (OC-SVM)  
Spodumene pegmatite  
Unknown matrix

## ABSTRACT

Mineral exploration and active mining relies on extensive drilling campaigns that produce large numbers of drill cores. LIBS is ideally suited for their fast and effective measurement, but matrix effects complicate quantitative geological LIBS applications due to the extensive amount of different minerals, rock types, and lithologies, as well as all textural and optical parameters increasing physical matrix effects. This is challenging for the application of LIBS in geological exploration, since LIBS data processing highly depends on matrix-matched models. The fast acquisition of new data is in conflict with the large amount of existing minerals and lithologies. As a result, new appearances are common during ongoing drilling campaigns, resulting in incomplete train sets for supervised classification and quantification.

This paper presents a novel semi-supervised learning (SSL) classification model to resolve related issues by separating known minerals in geological drill cores based on a set of train samples, while also detecting unknown material, i.e. new lithologies and/or minerals not in the train set. Using a combination of supervised Linear Discriminant Analysis (LDA) and semi-supervised One-Class Support Vector Machines (OC-SVM), main minerals and known accessory minerals were effectively separated from unknown material in LIBS mappings of Spodumene and Muscovite pegmatite, as well as from Metagreywacke in drill cores from the Rapasaari lithium deposit in Finland. Self-learning was applied to automatically increase the number of train samples, which effectively decreased the number of unknowns due to physical matrix effects in coherent crystals.

Validation with respect to the main minerals revealed an almost perfect classification of albite, spodumene, K-feldspar, quartz, and muscovite. Measurement points of Metagreywacke, which were only included in the test set, were correctly detected as unknown. Transferring the developed model onto LIBS mappings and drill core profile measurements displayed excellent classification results for main and accessory minerals included in the train set. Mixed spectra at mineral borders, as well as accessory minerals not in the train set were correctly identified as unknown.

## 1. Introduction

Laser-Induced Breakdown Spectroscopy (LIBS) is an analytical technique receiving increasing interest in a wide variety of fields during recent years [1–5]. A highly energetic laser beam is focused onto the investigated sample (solid, liquid or gas), ablating small amounts of material to create a plasma that contains the elemental information of the ablated surface. During plasma cooling, atomic signatures are emitted and the resulting spectrum is collected with optical instruments (e.g. in [6,7]). Elements show emission peaks at element specific wavelengths, which enables the detection of multiple elements in a

single spectrum.

Measurements can be performed in-situ with high speed and high resolution under atmospheric conditions and nearly no sample treatment is required [1]. Practically all elements can be measured, which makes LIBS especially useful for geological applications since it allows the detection of major, minor, and trace elements at the same time (e.g. in [1–3]). It has already been used to address different kinds of geological subjects (e.g. in [8–15]) and unlike most analytical methods, LIBS can detect even small traces of Li. It has therefore been applied to detect and (semi-)quantitatively analyse various Li-bearing minerals in different geological samples with unsupervised methods and univariate

<sup>\*</sup> Corresponding author.

E-mail address: [Jeannet.Meima@bgr.de](mailto:Jeannet.Meima@bgr.de) (S. Müller).

<https://doi.org/10.1016/j.sab.2022.106370>

Received 28 September 2021; Received in revised form 14 January 2022; Accepted 14 January 2022

Available online 19 January 2022

0584-8547/© 2022 The Authors. Published by Elsevier B.V. This is an open access article under the CC BY license (<http://creativecommons.org/licenses/by/4.0/>).



regression models [16–18].

Major drawback of LIBS are the physical and chemical matrix effects that make the analysis of LIBS measurements especially challenging for heterogeneous material [19–21]. Physical and chemical matrix effects are often problematic in geological applications, since differences in surface topography, grain size, elemental concentrations, transparency of individual minerals, or the way the laser hits the mineral lattice influence the LIBS plasma, resulting in different responses in the spectrometer [22–24]. Additionally, phase transitions from one mineral to another cannot be perfectly resolved, which results in mixed spectra on mineral borders [9,25]. Despite these challenges, its speed coupled with its high resolution makes LIBS an especially promising technique for geological exploration and mining campaigns, where large amounts of drill cores are analysed [9,26–30].

Contrary to the speed of measurement, preparing reference samples for LIBS quantification is time consuming and difficult, since matrix-matched standards are needed (e.g. in [8,21,31]). Unfortunately, existing LIBS-based mineral libraries cannot be transferred between different LIBS systems yet [32]. This requirement of matrix-matched standards, however, can become especially challenging for the application of LIBS in exploration settings. The appearance of new lithologies or minerals is common during ongoing drilling campaigns, resulting in incomplete train sets. To avoid unreliable quantification or classification results, it is necessary to explicitly identify new data not covered by the reference data. The majority of conventional supervised classification algorithms lack this possibility of identifying “unknown” samples [33], although, for example, Spectral Angle Mapper (SAM) or Minimum Distance allow the detection of unknown data points based on thresholds. Nevertheless, defining these thresholds manually is time consuming and difficult, since they may be matrix-dependent and have to be validated for each mineral individually.

Semi-supervised learning (SSL) has been used to classify large amounts of unknown data based on a small set of known reference samples. If the unknown data point is similar to the set of reference samples, it is classified accordingly, otherwise, it is labelled as unknown [33]. Here, SSL can help to detect unknown measurement points in LIBS data of geological drill cores. To our knowledge, no LIBS-based publication used SSL for this purpose. Instead, several approaches exist in other disciplines (e.g. in [34–37]). Various methods exist to enhance classification results of SSL algorithms. One involves a manual selection of data points initially classified as unknown. After an identification based on expert knowledge, they are added to the set of reference samples and a new classification model is calculated (e.g. in [38]). Another possible option – self-learning – iteratively increases the set of reference samples automatically with the newly classified measurement points and classifies the remaining unknown data again [33].

The objective of this paper was the novel application and validation of the SSL classification algorithm One-Class Support Vector Machines (OC-SVM) for LIBS measurements in geological settings, with the purpose of detecting known minerals and unknown matrix with a limited set of train data. To cope with the strong physical matrix effects in the investigated pegmatite samples, self-learning was investigated to automatically increase the reference dataset iteratively. This SSL-based method was tested for well-known drill cores from the Rapasaari lithium-deposit in Finland, containing Spodumene pegmatite, Muscovite pegmatite and Metagreywacke. Prior to OC-SVM, the LIBS data were transformed with Linear Discriminant Analysis (LDA) to increase class separability and to create distinct clusters. This is important for the density-based class boundary calculation performed with OC-SVM, which enables the creation of narrow class boundaries used to identify known minerals, while also detecting unknown material. Although there are no publications combining LDA and OC-SVM, different approaches successfully employ LDA to improve the classification of LIBS measurements (e.g. in [39–43]). OC-SVM on the other hand has only been used for classification in other fields of spectroscopic analysis (e.g. in [44–46]).

## 2. Material and methods

### 2.1. Sample description

The Rapasaari lithium deposit is part of the Kaustinen lithium pegmatite province in Finland and hosts Spodumene pegmatite with modelled  $\text{Li}_2\text{O}$  concentrations between 1.02 and 1.46 wt% [47]. Rocks typically found in the Rapasaari area cover Spodumene pegmatite, Muscovite pegmatite, mica schists (mostly Metagreywacke), intermediate volcanic rocks and rarely sulphide rich schists [47]. Nine drill core meters from the Rapasaari lithium deposit were analysed in this project, consisting of three different rock types: The first 7.9 m cover drill cores from the Spodumene and Muscovite pegmatite that were cut in half, whereas the remaining 1.1 m contain Metagreywacke left intact.

Table 1 lists the main minerals of Spodumene and Muscovite pegmatite together with their mineral formula and optical characteristics relevant for LIBS, which both highly influence the resulting spectrum. Optical characteristics may vary from sample to sample, depending on the angle that the minerals are cut or, in the case of transparency, the underlying minerals. Crystal sizes in the Spodumene pegmatite range from 0.5 to several centimetres and especially spodumene and albite show large crystals with lengths up to 10 cm [47–49], which is also observed in the investigated drill cores. The Muscovite pegmatite includes identical minerals as the Spodumene pegmatite but with varying distributions. The number of spodumene crystals decreases strongly, whereas proportions of muscovite increase. The sizes of feldspar and quartz grains are similar to the Spodumene pegmatite, whereas the average size of spodumene and muscovite crystals decreases to several millimetres. Additionally, the Muscovite pegmatite developed porosities between the small crystals, which is not found in the Spodumene pegmatite. Both pegmatites may include grains of the accessory minerals apatite, zinnwaldite, Nb-Ta-oxides, beryl, garnet (grossular), arsenopyrite, and sphalerite [47–49]. The two pegmatites are optically difficult to distinguish, due to identical minerals and similar colours.

The Metagreywacke of the Rapasaari complex mostly consists of mica schists with additional minerals of feldspar, quartz, different mica, and matrix, which is also mostly comprised by mica. In general, greywacke is a very broad term lacking a clear definition and for the investigated samples in this paper, estimating the mineral proportions is difficult due to the small size of the crystals that mostly lie in the sub-millimetre scale. Nevertheless, the whole lithology is clearly separable from the pegmatites through its darker colour. Fig. 1 displays the investigated drill cores and highlights the areas of the LIBS mappings, the different lithologies, and their transitions.

### 2.2. LIBS measurements

All LIBS measurements were performed with a drill core scanner prototype developed by Lasertechnik Berlin (LTB) in 2011. The instrument includes a Q-switch Nd-YAG laser, operating with a repetition rate of 20 Hz, a pulse duration of 11 ns, an excitation wavelength of 1064 nm

**Table 1**  
Main minerals of Spodumene and Muscovite pegmatite, their corresponding formula and relevant optical characteristics for LIBS.

Mineral	Formula	Optical characteristics
Albite (feldspar - pure Na-endmember)	$\text{Na}[\text{AlSi}_3\text{O}_8]$	Opaque
K-feldspar (feldspar - pure K-endmember)	$\text{K}[\text{AlSi}_3\text{O}_8]$	Opaque
Quartz	$\text{SiO}_2$	Transparent
Muscovite	$\text{KAl}_2[(\text{OH}, \text{F})_2]$ $\text{AlSi}_3\text{O}_{10}$	Reflective, shiny, flaky
Spodumene	$\text{LiAlSi}_2\text{O}_6$	Visible cleavage, shiny

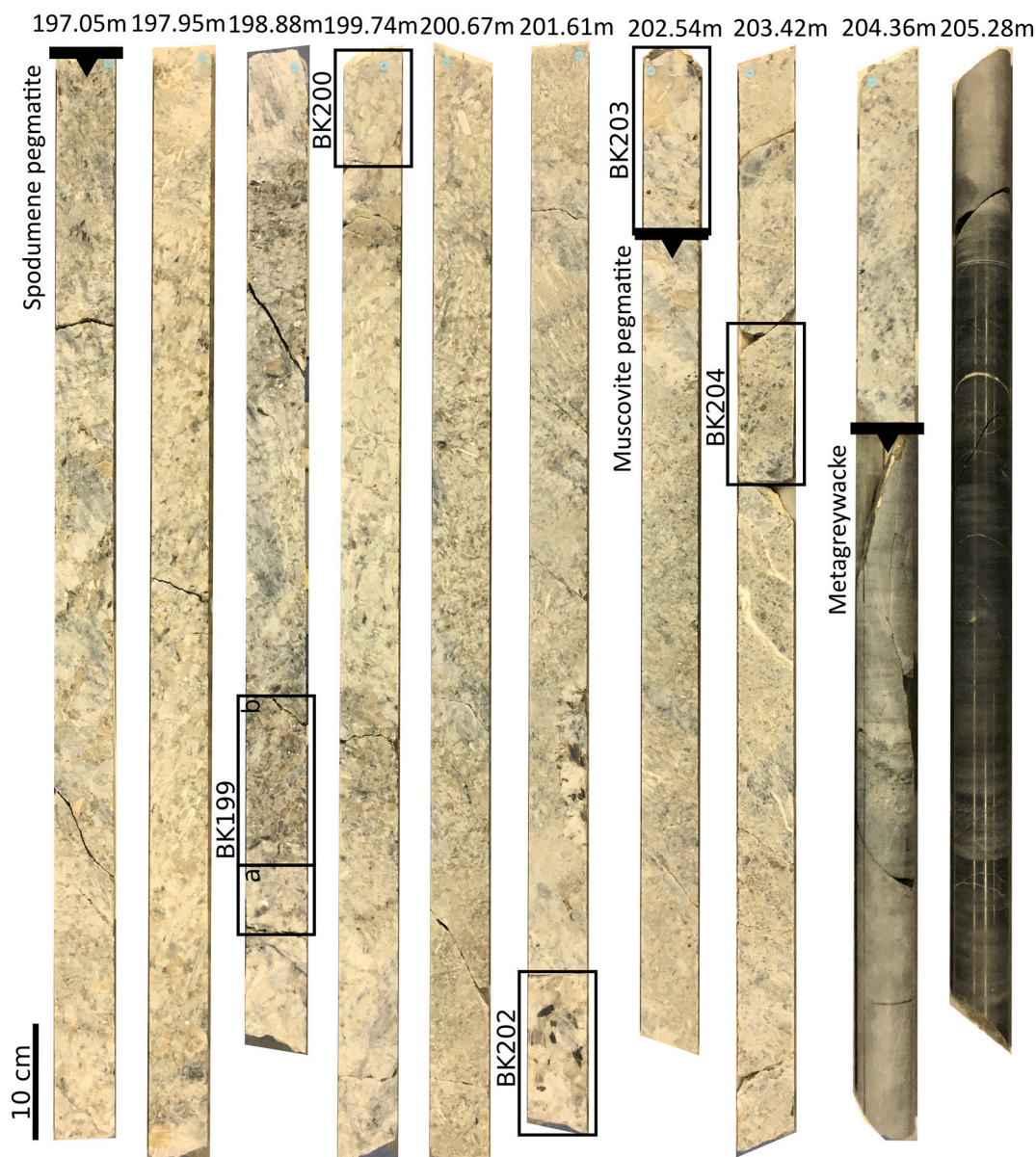


Fig. 1. Drill cores from the Rapasaari complex investigated in this study. A LIBS profile was taken through the centre of every drill core and detailed LIBS mappings were taken for the six rectangles. The three lithologies are highlighted, the arrow indicates the measurement direction.

and a laser energy of 35 mJ. The plasma is captured with an Echelle spectrometer covering a spectral range of 285–964 nm with a resolution of 0.029–0.096 nm and a CCD detector. The laser has a spot size of 200  $\mu\text{m}$  and can move up to 1 m in X and 2.5 cm in Y direction, the investigated sample remains in place. To avoid cross-crater contamination and the ionization of small dust particles between laser head and focus point during laser movement, an exhaust system is attached and moves with the laser. Spectrometer and CCD are constantly held at 27 °C to minimize the effects of temperature change during measurements. More information on the LIBS setup can be found in [8].

Delay time and number of accumulated laser shots were optimized based on signal-to-noise ratio and line intensities of elements present in the main minerals of the Spodumene pegmatite (i.e. Si, Al, Na, K, and Li). Optimal results were achieved with three accumulated shots. A 1D-profile measurement was performed point by point by moving the laser for 200  $\mu\text{m}$  in X direction through the centre of every drill core, with a short stop for each distinct point measurement. The Spodumene and Muscovite pegmatite were measured along their cut surface, whereas the exterior part of the uncut Metagreywacke was measured. To ensure

comparability, core measurements of uncut Metagreywacke were validated with spectra of a cut surface from a Metagreywacke sample and similar intensities were achieved.

Additionally, six selected areas highlighted in Fig. 1 were mapped with a step size of 200  $\mu\text{m}$  in Y and X direction. Their length ranges from 4.8 to 16 cm with a consistent width of 4.8 cm. The samples cover all main minerals of the Spodumene and Muscovite pegmatite in various proportions and sizes, representative for both lithologies. Due to their width above 2.5 cm, every sample was divided into two areas that were measured independently. After one area was mapped, the sample was moved by hand parallel to the stage for 2.5 cm in the specific direction. Afterwards, the two corresponding areas were merged into one dataset that was used for analysis.

### 2.3. Spectral processing

Fig. 2 displays a typical spectrum of every main mineral present in the pegmatites and one typical spectrum of the Metagreywacke. Using the entire spectrum for classification purposes would result in large

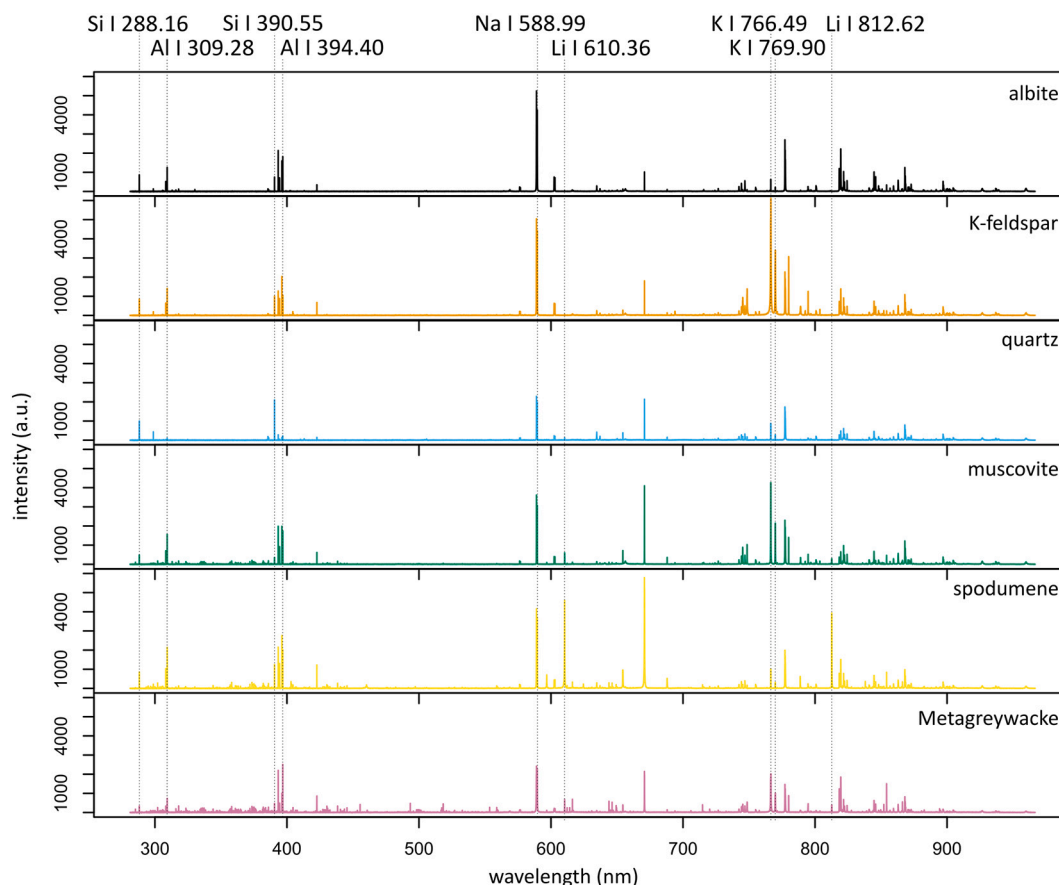


Fig. 2. Representative spectra of the main minerals present in the Spodumene and Muscovite pegmatite and a typical spectrum of the Metagreywacke lithology.

amounts of redundant information. Therefore, relevant emission lines were chosen based on elemental compositions of the main minerals shown in Table 1 (Al, K, Li, Mg, Na, and Si). Additionally, lines for Be, Ca, Nb, P, and Zn were extracted to cover elements of all accessory minerals described in the literature [47]. Since the developed classification model aims at detecting unknown geological material of all kinds, emission lines for the major rock forming elements Fe, Mn, and Ti were added as well. At least two lines were extracted for every element covering different regions of the spectrum. The lines were located using knowledge of previous work [10] as well as [18] for the three relevant Li I lines at 610.36 nm, 670.79 nm, and 812.64 nm.

The emission lines were extracted using peak integration performed with an in-house C-program and an integration window of 1.0 nm for spectral regions below 600 nm and 1.5 nm for spectral regions above 600 nm, which is in accordance with the observed peak widths. All emissions line intensities were normalized using the total intensity of the corresponding spectrum collected by the spectrometer to reduce shot-to-shot variations. Collinearity of variables introduces severe problems for the discrimination ability of LDA [50], and since different emission lines of the same element show collinearity, the number of extracted emission lines was ultimately reduced to one line per element. The optimal set of emission lines for LDA was determined based on the best separation of mineral classes and unknown material using the developed classification model. Best results were achieved using the emission lines displayed in Table 2, which were then used to generate LIBS hyperspectral data cubes, where each pixel represents a single LIBS measurement and each image the spectral intensity of a single target emission line (see [9] for a detailed explanation). This allows an uncomplicated visualization and processing of spatially resolved element distributions. For the extraction of mineral-specific measurement points, the ENVI image analysis software (version 5.5) was applied.

Table 2

Final set of emission lines showing best classification results.

Element	Spectral line (nm)	$E_i$ (eV)	$E_k$ (eV)	$A_{ki}$ ( $10^8 \text{ s}^{-1}$ )
Al I	396.15	0.014	3.14	0.99
Ca II	315.89	3.12	7.05	3.10
Fe I	373.49	0.86	4.18	0.90
K I	766.49	0.00	1.62	0.38
Li I	812.64	1.85	3.37	0.22
Mg I	285.21	0.00	4.35	4.91
Mn I	403.08	0.00	3.08	0.17
Na I	818.33	2.10	3.62	0.42
Si I	288.16	0.78	5.08	2.17
Ti II	308.80	0.049	4.06	1.50
P II	603.40	10.74	12.79	0.38
Be II	313.04	0.00	3.96	1.13
Nb I	379.12	0.13	3.40	0.64
Zn I	334.50	4.08	7.78	1.50

#### 2.4. Creation of train and test data

The reference data for the initial SSL classification model were extracted from regions of interest (ROIs) that belong to one of the main minerals shown in Table 1, which will be the known classes for the SSL classification model. This initial model does not yet contain any accessory minerals, to be able to test the model's ability to detect accessory mineral as unknowns. ROIs for distinct minerals were identified by comparing optical images of the six detailed LIBS mappings highlighted in Fig. 1 with RGB images covering different LIBS emission lines. Fig. 3 shows a grey value image of emission line Al I 396.15 nm with the mineral-specific ROIs extracted from mappings BK199a and BK199b. This way, 70 ROIs were extracted from the six LIBS mappings, covering 14 ROIs of albite, 12 of K-feldspar, 19 of quartz, 12 of muscovite, and 13



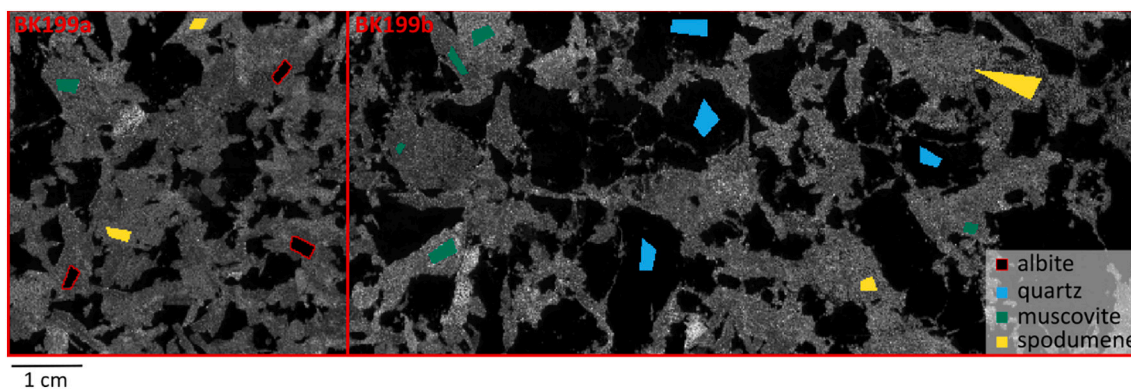


Fig. 3. Grey value image of LIBS mappings BK199a and BK199b for emission line Al I 396.15 nm with all ROIs that were extracted from these mappings.

of spodumene. Three ROIs of every mineral (i.e. every class) were randomly removed from the reference set and stored for testing. The measurement points of the remaining 55 ROIs were used to build the train set.

Every ROI covers a varying number of measurement points. Physical matrix effects can lead to variations in the measured LIBS intensities within a single crystal (i.e. one ROI), even in chemically homogeneous material [23]. Using only the average intensity of each ROI was not sufficient to cover the observed intensity variations. Therefore, an arbitrary number of 25 measurement points was selected from every ROI using the Kennard-stone algorithm [51] implemented in the R-package *prospectr* [52]. The algorithm samples the desired amount of data points based on pairs of measurement points with maximum Euclidean distance from one another. This allows the creation of a reproducible subset with uniform intensity distribution over each ROI. To enable a validation of the algorithm's ability to detect unknown samples, 40 single measurement points of Metagreywacke were randomly selected and included in the test set. The train set contains the five classes albite, K-feldspar, quartz, muscovite, and spodumene, whereas the test set includes the additional unknown class Metagreywacke.

The large crystals in the pegmatite allow relatively easy identification of mineral phases based on optical appearance and LIBS intensities, which is why the described procedure for collecting reference samples works especially well for the investigated material. Additional Raman measurements were performed on a few typical crystals in smaller samples to verify the correct identification of the main minerals.

### 2.5. Creation of a reference image

In addition to the train and test set, a pixel-matched reference image of LIBS mapping BK199a was created. Sample BK199a consists of the five main minerals listed in Table 1 and does not contain significant accessory minerals. A random forest model was built and used as the foundation for the ground truth image. To capture areas not representing albite, K-feldspar, quartz, muscovite, and spodumene with the random forest model (i.e. mineral borders at transition zones, porosities or accessory minerals), over 3000 pixel from various mineral borders and coherent ROIs from different accessory minerals were labelled as an unknown class. Wrongly classified pixel from the random forest model were customized based on geological expertise and macroscopic analysis of the physical sample, as well as RGB images of different mineral-specific combinations of LIBS emission lines. Special attention was paid to label the visible porosities and transition zones between minerals as unknown. Extracting single pixel from mineral transitions and small accessory minerals for the random forest model, as well as the manual adaption of wrongly classified pixel was very time consuming and inefficient, but necessary to validate the results of the newly developed SSL classification model in Section 3.2.1.

### 2.6. Workflow of the SSL classification model

Fig. 4 illustrates the workflow of the developed SSL classification model, using the open-source software R, version 3.5.1 [53]. Three independent steps are performed, before the newly classified data is added to the train set and the classification model is run again.

In the first step, the training data are transformed into the LDA-space with the LDA algorithm included in the MASS package available in R [54]. This supervised method enhances class separability and reduces dimensionality by calculating between-class variance and within-class variance as the distance between the means of the different classes and the distance between mean and samples of an individual class, respectively. It contains  $n-1$  dimensions, where  $n$  is the number of classes. For a detailed description of LDA, we refer to [55].

Subsequently, the LDA-transformed data of the train set is used to calculate an individual class boundary for every mineral class with OC-SVM. Thereto, OC-SVM computes a binary function to capture regions in the input space where the probability density of the investigated class lives [56]. The function results in positive values for unknown data points that are in regions with a high density of labelled reference data and in negative values for the rest. This function is used to check class boundaries of unknown data in step 2. In this paper, the OC-SVM algorithm of R-package *e1071* [57] was applied. It is based on the algorithm proposed by [56] to which we refer for a detailed explanation. To compute an optimal class boundary with OC-SVM, the radial basis Kernel (RBF) was applied and parameter 'nu' was automatically tuned using a grid search with values from 0.01 to 0.2 and a step size of 0.01, while gamma was left at default.

In the second step, the unknown data are transformed into the LDA space of the train samples using the LDA function calculated in the first step. The transformed data are inserted into the binary OC-SVM functions of every class and the results are stored for label assignment.

The third step predicts class membership of the unknown data. If the results of all OC-SVM functions are negative for an unknown data point, it is classified as unknown. If one single mineral-specific boundary function is positive, the sample is labelled according to the corresponding mineral class. Class boundaries might overlap and a measurement point can therefore show positive values for more than one mineral-specific boundary function. The questionable data point is then classified according to the class centre with smallest Euclidean distance.

Subsequently, self-learning begins, which means that the newly labelled data are added to the train set and a new classification model is built in step 1 to predict the remaining unknown samples in step 2 and 3. Due to the increased number of reference data, the LDA-space may change and, as a result, change the boundary calculation as well. In this paper, self-learning was applied iteratively for an arbitrary number of seven times or until no more changes to the classification results were observed.

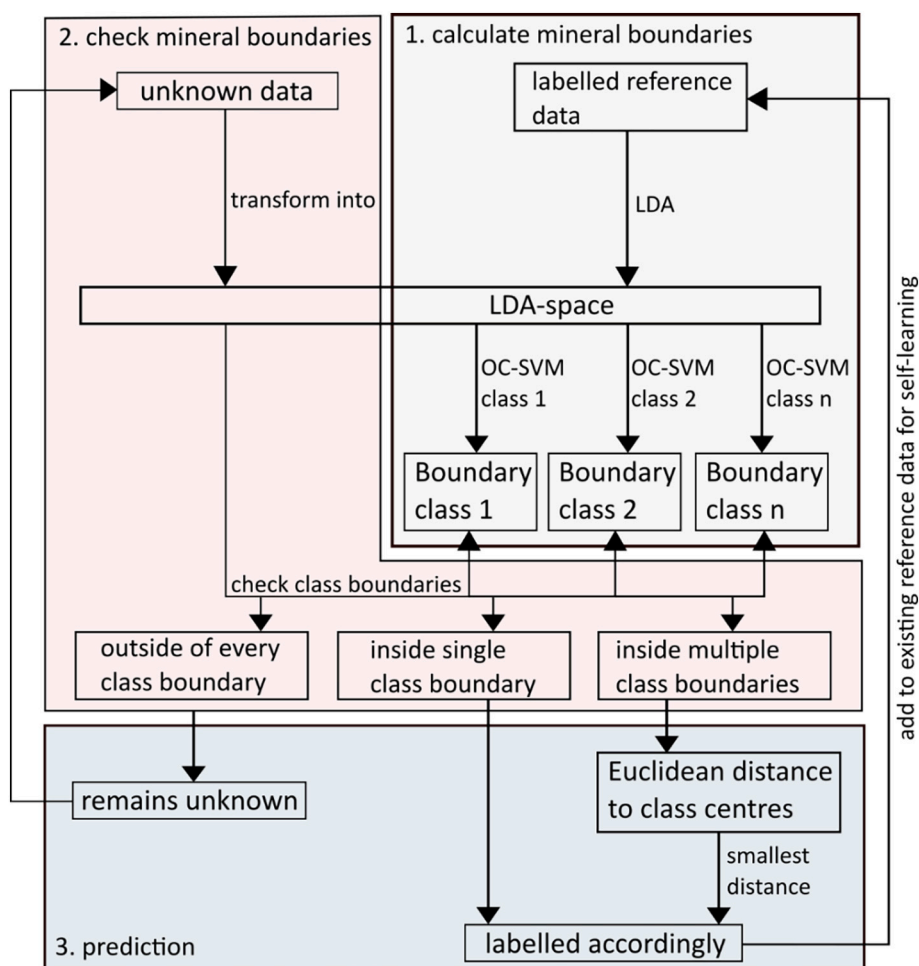


Fig. 4. Workflow implemented for the SSL classification model of minerals and unknown matrix. The number of reference data increases after each iteration using the newly labelled data as additional training samples, until there are no more changes to the classification results or a pre-defined number of iterations has been reached.

### 3. Results and discussion

#### 3.1. Evaluating the SSL classification model using train and test data

To evaluate the results of the developed classification model, the test set was predicted and classified as described in Section 2.6. Classification results of the test set are shown in the confusion matrix in Table 3. Misclassification between the known mineral classes does not exist and all points of Metagreywacke, the lithology unknown to the train set, were correctly identified as unknown. Self-learning did not show any improvement for the test set, since the low number of test samples did not influence the newly calculated LDA-space and therefore no new boundaries were created with OC-SVM. Despite the good results, 1 out of 75 reference points of muscovite as well as 2 out of 75 reference points of K-feldspar and quartz were incorrectly classified as unknown. It is

important to investigate possible reasons for this misclassification to understand the classification results of the detailed LIBS mappings described in Section 3.2.

Fig. 5 indicates the separation ability of LDA for the different minerals of the train and test set including the unknown class (here Metagreywacke). Due to their distinct chemical compositions, spodumene (high  $\text{LiO}_2$  values) and quartz (only  $\text{SiO}_2$ ) form distinct clusters in several combinations of the LDA-space. Containing similar major elements but in varying proportions, muscovite, albite, and K-feldspar show mineral clusters close to each other, sometimes even overlapping. Nevertheless, the different element ratios allow a distinct separation of feldspar and muscovite, visible in the combination LD1 – LD2. K-feldspar and albite are endmember of a solid solution with varying contents of K and Na. Their chemical similarity leads to overlapping clusters in some combinations of the LDA-space. Nevertheless, distinct differences can be

Table 3

Confusion matrix with classification results of the test set using the combination of emission lines shown in Table 2. The reference data is shown vertically, the prediction results horizontally.

	Albite	K-feldspar	Quartz	Muscovite	Spodumene	Unknown
Albite	75	0	0	0	0	0
K-feldspar	0	73	0	0	0	0
Quartz	0	0	73	0	0	0
Muscovite	0	0	0	74	0	0
Spodumene	0	0	0	0	75	0
Unknown	0	2	2	1	0	40

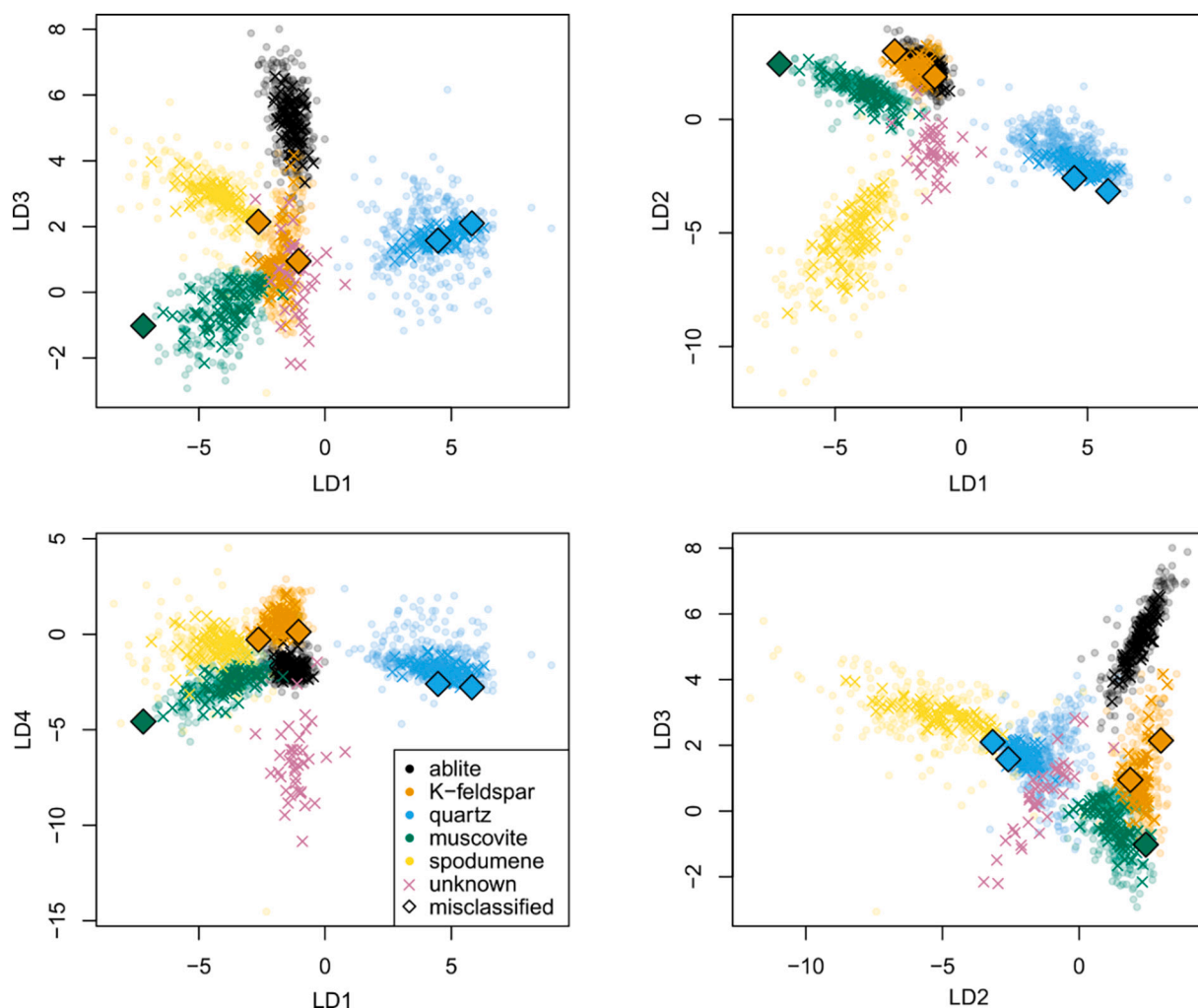


Fig. 5. Different combinations of dimensions of the LDA-space calculated with samples of the train set (circles). The crosses correspond to measurement points of the test set, the magnified diamonds represent the measurement points that were wrongly classified as unknown.

observed in the combination LD2 – LD3 and Table 3 does not show misclassification of albite as K-feldspar or vice versa. The Metagreywacke samples are correctly labelled as unknown, forming distinct clusters in LD1 – LD2 and LD1 – LD4.

The misclassified points of muscovite, K-feldspar, and quartz plot at the edges of their corresponding mineral cluster in several LD-combinations (Fig. 5). This implies that the mineral boundaries calculated with OC-SVM follow the density distribution of the corresponding mineral cluster very closely and as a result, small intensity deviations of newly measured material can lead to a classification as unknown. The scattering of the training data reflects the spectral variations of each mineral class, which in this particular case are induced by physical matrix effects, mostly due to varying optical properties of the investigated minerals. Consequently, not all intensity variations of every individual LIBS spectrum may be covered by the train set, and outliers are in turn classified as unknown. Increasing the train set by hand is a possible option to cover more intensity variations. This time consuming practice was not very successful and, therefore, self-learning was investigated in detail in Section 3.2, to automatically increase the train set with the newly classified data.

### 3.2. Evaluating the SSL classification model for detailed drill core measurements

#### 3.2.1. LIBS mapping BK199a consisting mostly of main minerals

For further validation purposes, the SSL classification model for the main minerals was subsequently applied on mapping BK199a (Fig. 1). It mostly includes main minerals and therefore allows an evaluation of the results obtained with the initial train set. To be able to evaluate the classification results, a customized reference image was created as described in Section 2.5. Fig. 6 displays the optical image as well as an RGB image of BK199a, together with the reference image and the classification results of the SSL classification model without- and after the first iteration of self-learning.

The RGB image in Fig. 6 features the selected emission lines for Si, Al, and Li (Table 2). Blue areas indicate high intensities of Li I 812.64 nm correlated to spodumene, red areas display high intensities of Si I 288.16 nm, corresponding to quartz. With high Al I 394.15 nm intensities, green pixels mostly indicate albite, K-feldspar, and muscovite, respectively. The customized reference image and the classification results without- and after the first iteration of self-learning are displayed in the bottom three images of Fig. 6. In general, a very good correspondence between the SSL classification result and the reference image can be observed. The main minerals represented by the train set are well recognized by the SSL classification model.

In total, 14.2% of all pixels of the reference image are labelled as



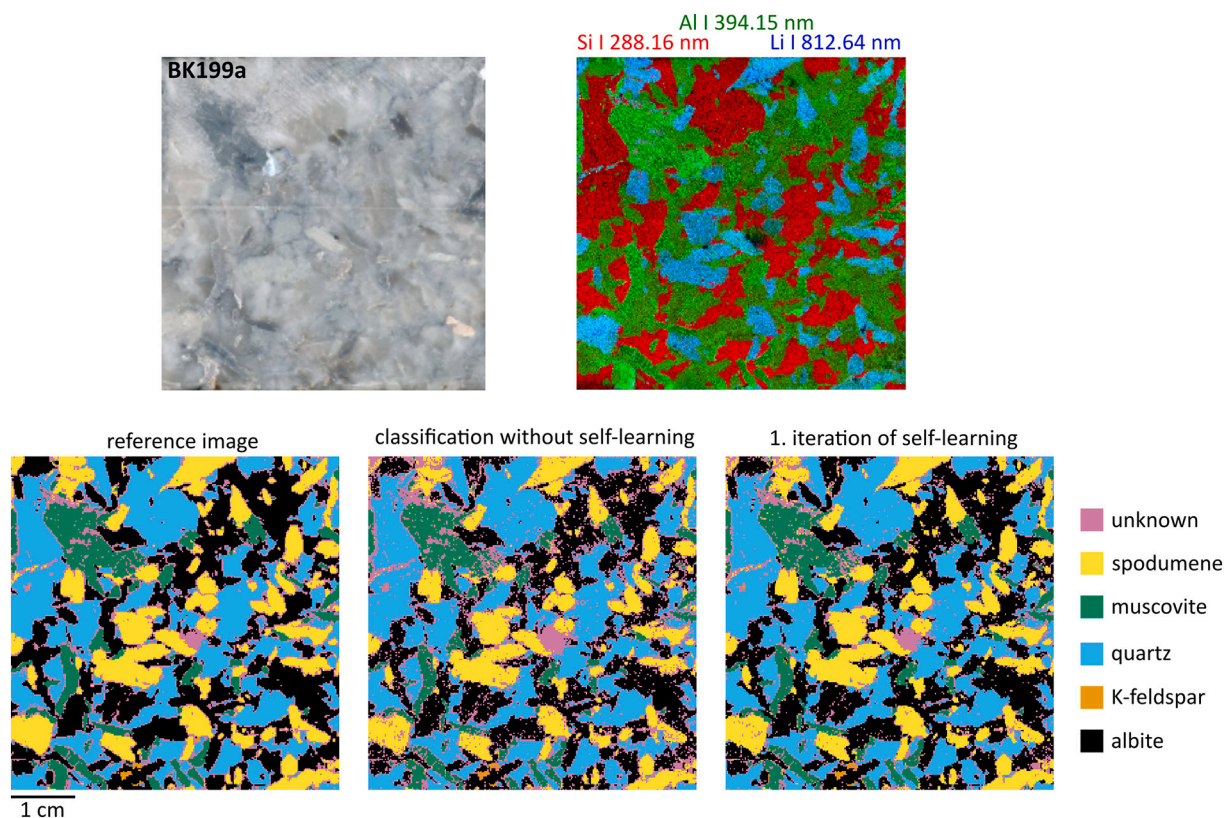


**Fig. 6.** Optical image of Spodumene pegmatite mapping BK199a and an RGB image with Si I 288.16 nm (red), Al I 394.15 nm (green) and Li I 812.64 nm (blue), as well as the reference image and the classification results without- and after the first iteration of self-learning. In the RGB image, quartz (red), muscovite and albite (both green), as well as spodumene (blue) can be identified. (For interpretation of the references to colour in this figure legend, the reader is referred to the web version of this article.)

unknown. The number of unknowns in the SSL classification result without self-learning, however, is higher than in the reference image (20.1%), decreasing with the first iteration of self-learning to 12.9%. Overall, three main reasons for the occurrence of unknowns were revealed:

- (1) Unknown measurement points are found at mineral borders between different mineral grains. Here, the laser spot covers two or more distinct minerals, resulting in mixed spectra at transition zones. Since the train set only comprises measurement points of pure minerals, mixed spectra lie outside the mineral boundaries calculated with OC-SVM and are accordingly classified as unknown. This is shown in Fig. 7, where exemplary measurement points from different mineral borders were extracted from LIBS mapping BK199a and transformed into the LDA-space without self-learning. Accordingly, the measurement points plot between the clusters formed by minerals of the train set. With self-learning, the mineral cluster variability increases due to the increased number of train samples. As a result, fewer pixel from mineral transition zones lie outside the mineral boundaries calculated with OC-SVM and therefore, fewer pixel from mineral transition zones are classified as unknown.
- (2) Single measurement points inside of large crystals are occasionally classified as unknown. They correspond to pixel with intensity variations not fully covered by the limited number of training samples, as discussed in Section 3.1. Individual mineral crystals do not seem to have constant optical properties (Fig. 6). In particular, the degree of porosity and transparency seems to vary, leading to increased intensity variations and a possible classification as unknown for single points in large crystals. After the first iteration of self-learning, the image shows significantly

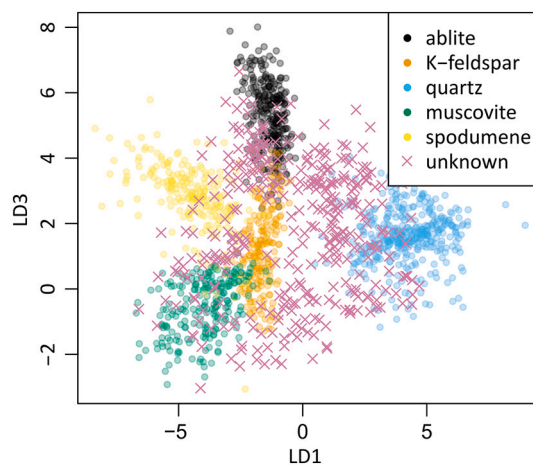


**Fig. 7.** LD1 and LD3 of the LDA-space without self-learning and selected measurement points from exemplary mineral transitions of sample BK199a, labelled as unknown (crosses).

less single measurement points that are classified as unknown (Fig. 6).

- (3) Minerals unknown to the train set, e.g. the coherent areas in the middle and top-left part of BK199a, are classified as unknown. Since only the main minerals were included in the initial train set, these measurement points were correctly identified as unknown.

The total number of unknowns is highly influenced by the crystal size of the minerals, since large accessory minerals or small crystals (i.e.

more mixed spectra due to mineral transitions) result in higher numbers of unclassified points.

Fig. 8 shows the influence of self-learning on the classification result, using the parameters recall (Eq. (1)) and precision (Eq. (2)). These parameters were calculated with the reference image and the classification results of sample BK199a after each iteration of self-learning. Because only 0.15 area-% of sample BK199a consists of K-feldspar and changes in precision are not representative, K-feldspar has not been considered for assessing the influence of self-learning.

$$\text{Recall} = \frac{\text{correctly classified pixel of a class}}{\text{total number of existing pixel of a class}} \quad (1)$$

$$\text{Precision} = \frac{\text{correctly classified pixel of a class}}{\text{total number of predicted pixel of a class}} \quad (2)$$

Recall values increase with every iteration of self-learning for albite, quartz, muscovite, and spodumene, but decrease for pixel classified as unknown (Fig. 8). From the first iteration of self-learning onwards, recall values are above 0.9 for the main minerals. This is explained by the decreasing number of measurement points classified as unknown due to physical matrix effects, as compared to the classification model without self-learning. Precision values, however, display opposing behaviour for every class (Fig. 8). The slow decrease observed for the main minerals is explained by the increasing number of mineral boundary points that are wrongly classified as albite, quartz, muscovite or spodumene. With respect to the unknowns, the decreasing number of mineral boundary points result in gradually decreasing recall values to below 0.53 after seven iterations of self-learning. Simultaneously, overcoming the physical matrix effects decreases the number of wrong predictions as unknowns and, thus, increases precision values of the unknown class from 0.54 to values above 0.73 after the first iteration of self-learning.

Due to the opposing behaviour of recall and precision, as well as the opposing behaviour of main minerals and unknown class, the combination of both indices has to be evaluated for every iteration of self-learning to get best results. Fig. 8 indicates an optimal combination of recall and precision after the first iteration of self-learning, which, therefore, was applied throughout this paper.

The corresponding confusion matrix for sample BK199a (Table 4) shows that misclassification between the classes that are included in the train set is nearly not existent, an observation that supports the findings of Section 3.1. The unknown measurement points mostly correspond to transition zones between the different minerals. The mineral crystals of

**Table 4**

Confusion matrix with classification results of sample BK199a after the first iteration of self-learning. The reference data is shown vertically, the prediction results horizontally.

	Albite	Quartz	Muscovite	Spodumene	Unknown
Albite	16,370	0	0	0	1298
Quartz	0	16,408	0	0	1112
Muscovite	0	0	5187	6	59
Spodumene	1	0	47	10,088	258
Unknown	860	324	367	464	5507

the investigated area are relatively small and therefore many transition zones exist. The discrepancy between reference sample and prediction concerning the unknown class is mostly a result of the increased number of train samples for the first iteration of self-learning. This increases the variability of each mineral cluster greatly, and, therefore, the mineral boundaries calculated with OC-SVM are expanded. As a result, pixel at mineral boundaries, which are unknown in the reference image, may be predicted as a neighbouring mineral instead.

### 3.2.2. Updating the SSL classification model by including accessory minerals

Fig. 9 shows for the consecutive mappings BK199a and BK199b the optical image, an RGB image with Si I 288.16 nm, Al I 394.15 nm and Li I 812.64 nm, and the classification result based on the SSL classification model developed in Section 3.1 after the first iteration of self-learning. The classification result displays large coherent areas that are labelled as unknown. These areas are associated with crystals of accessory minerals, inconsistently occurring throughout the selected drill core samples. The spectral differences of the corresponding measurement points are also reflected in the LDA-space (Fig. 10), where several measurement points of the unknown minerals are displayed. They form distinct clusters outside the calculated borders of the main minerals.

Specifying these accessory minerals allows an update of the SSL classification model and a classification of the unknown minerals in future samples. To identify the unknown areas, typical LIBS spectra for these unknown areas were compared to the mineral chemistry of all possible accessory minerals for this ore deposit [47–49]. Emission peaks for major elements, Be, Zn, and P suggest that the questionable areas presumably cover beryl ( $\text{Be}_3\text{Al}_2\text{Si}_6\text{O}_{18}$ ), apatite ( $\text{Ca}_5(\text{F,Cl,OH})(\text{PO}_4)_3$ ), and a Zn-bearing phase (Fig. 11). The beryl spectrum shows the characteristic duplet at Be II 313.042 nm and Be II 313.107 nm, as well as the

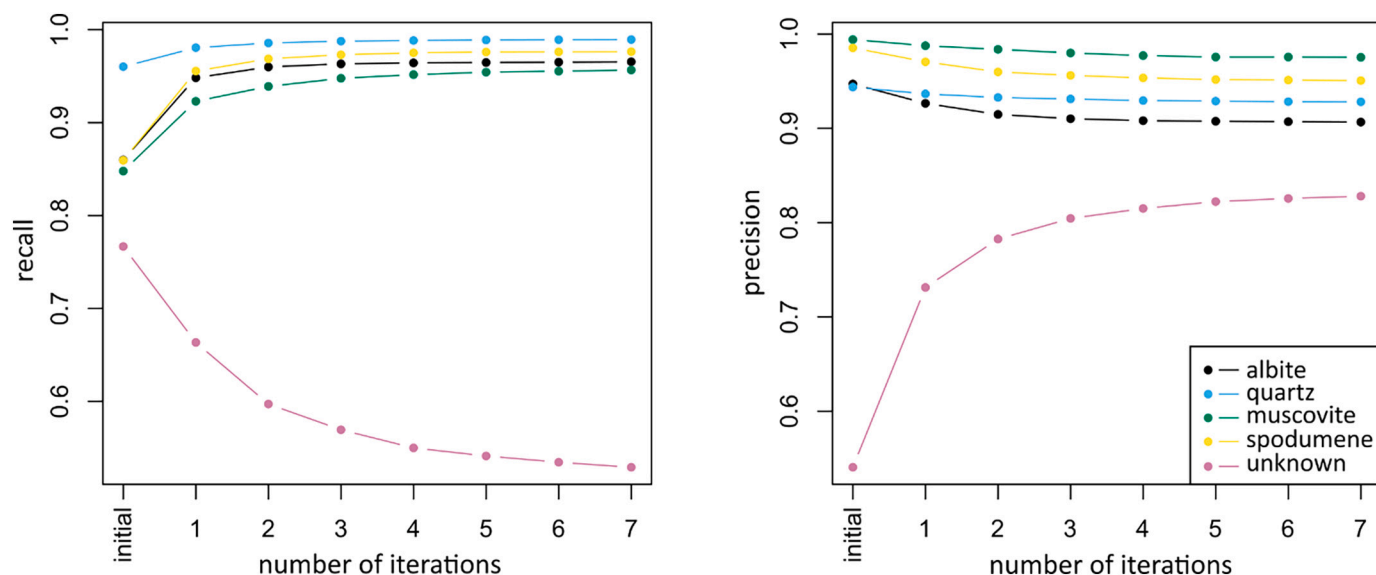


**Fig. 8.** Recall and precision of sample BK199a for the initial classification model without self-learning and every following iteration of self-learning.



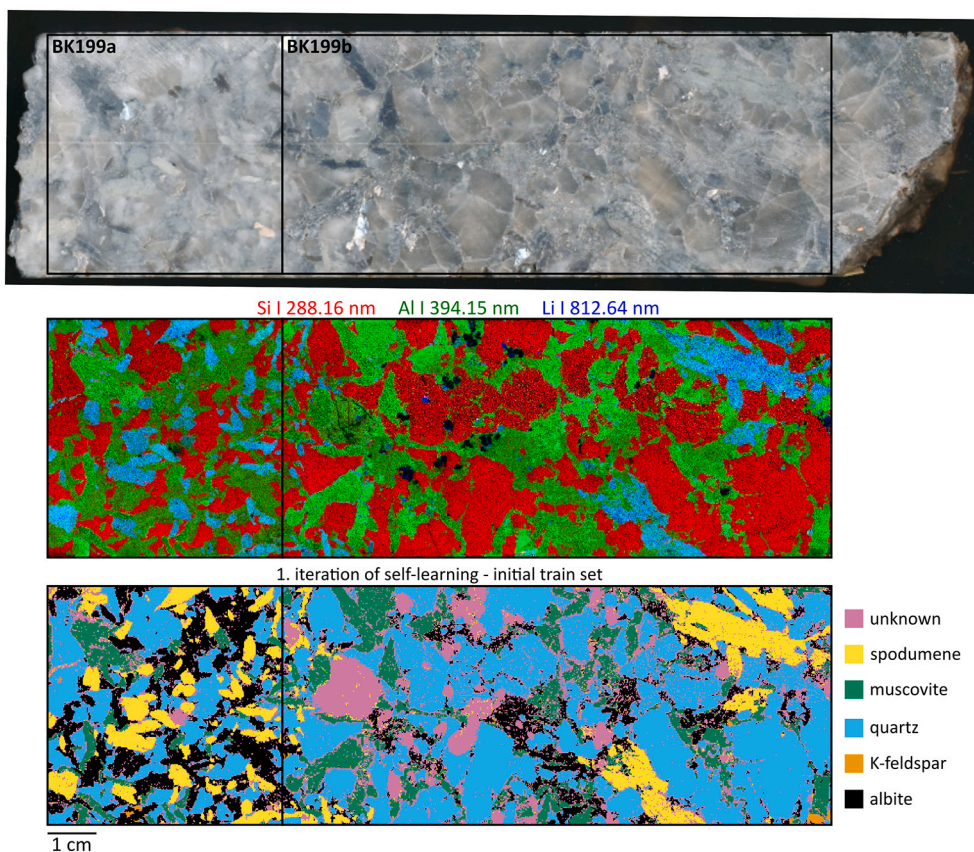


Fig. 9. Optical image, RGB image and classification result after the first iteration of self-learning for samples BK199a and BK199b, using the initial train set without accessory minerals.

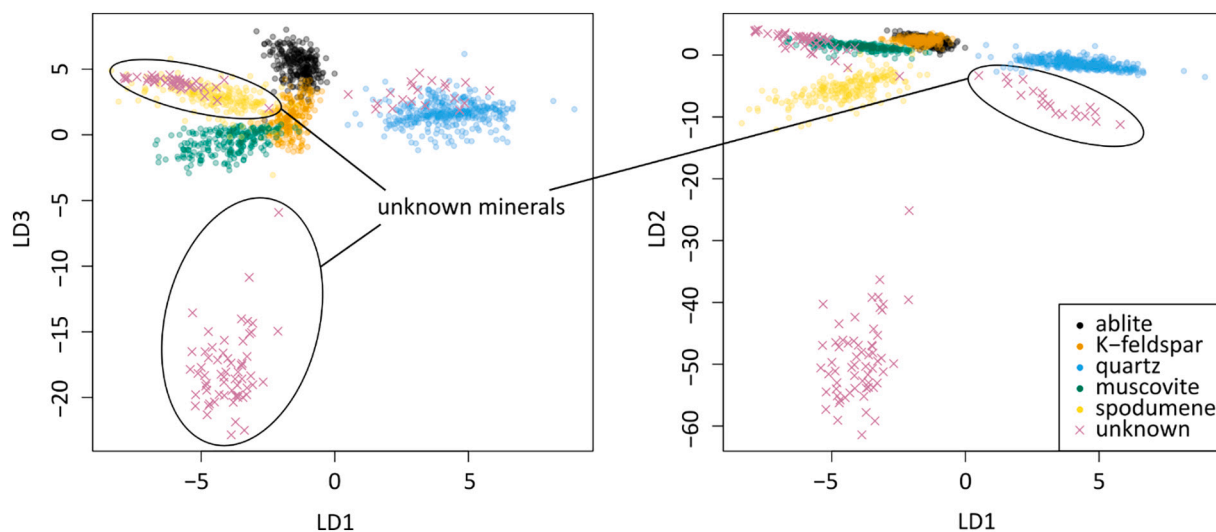


Fig. 10. Two different combinations of dimensions of the LDA-space without self-learning, showing selected measurement points of coherent areas classified as unknown in BK199a and BK199b (crosses). The distinct clusters formed by unknown measurement points belong to minerals that were not included in the initial train set.

characteristic Al emission lines. The apatite spectrum is dominated by Ca emission lines and shows emission at P II 603.404 nm. The Zn-bearing spectrum is characterized by emission lines for Zn. Low emission at S I 921.29 nm is observed as well, but no specific mineral assignment could be made. This results is supported by the RGB image of samples BK199a and BK199b shown in Fig. 12, which displays Be II 313.04 nm, Zn I 334.50 nm, and P II 603.40 nm, as green, red, and blue,

respectively. As a result, areas covered by beryl would appear green, the Zn-bearing phase red, and phosphate-bearing apatite would appear blue.

After their identification, representative measurement points of beryl, apatite, and the Zn-bearing phase were included in the train set and the SSL classification model was run again. The new classification result for samples BK199a and BK199b after the first iteration of self-

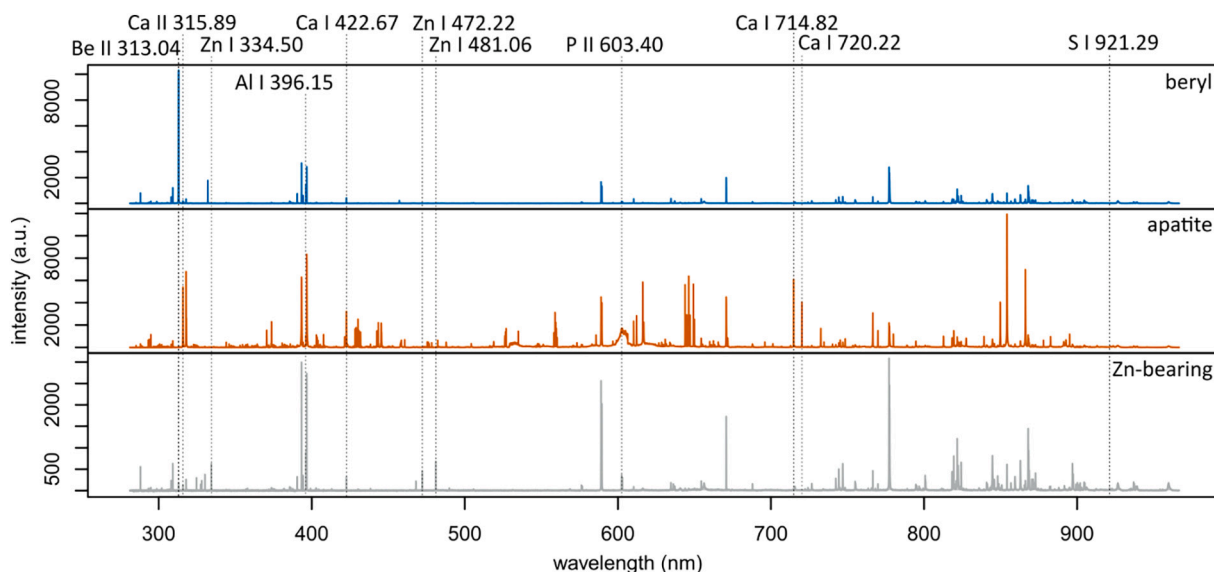


Fig. 11. Individual spectra of the accessory minerals beryl, apatite and a Zn-bearing phase. Several mineral specific element lines are highlighted.

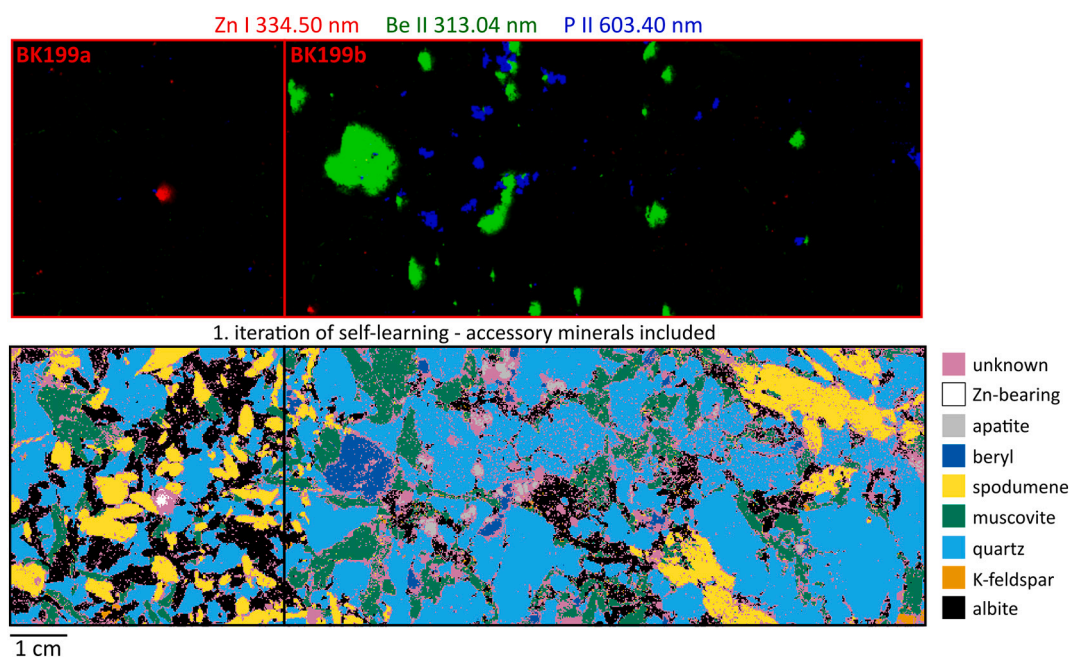


Fig. 12. RGB image of samples BK199a and BK199b, as well as the final classification result after the first iteration of self-learning. The RGB image features Zn I 334.50 nm, Be II 313.04 nm, and P II 603.40 nm, which reveals the accessory minerals beryl (green), apatite (blue) and a Zn-bearing phase (red). (For interpretation of the references to colour in this figure legend, the reader is referred to the web version of this article.)

learning is shown below the RGB image in Fig. 12. Most of the coherent areas formerly labelled as unknown are now correctly classified as beryl, apatite, and the Zn-bearing phase, respectively. Mostly transition zones and some individual points inside of large minerals remain unknown, whereas the majority of the large crystals are now correctly classified. Some small coherent areas remain unknown, even after updating the train set. These areas optically correspond to macro porosities.

### 3.2.3. Various LIBS mappings

Fig. 13 shows for all six LIBS mappings that the total number of unknown measurement points decreases with every iteration of self-learning. Samples BK199a, BK199b, BK200, BK202, and BK203 cover Spodumene pegmatite and include the main minerals of Table 1 in various proportions and crystal sizes. Sample BK204 is part of the

Muscovite pegmatite, showing increased porosities and smaller crystal sizes, although the main minerals are identical. Accessory minerals were only identified in the samples BK199a, BK199b, BK200, and BK204, with varying types, crystal sizes and proportions.

For BK199a and BK199b, the model without self-learning classified 23.4% and 26.8% of the sample as unknown, decreasing to 14.6% and 18.6% after the first iteration of self-learning, respectively. The larger percentage of unknowns in sample BK199b compared to BK199a has been identified as a result of increased porosities. Since the accessory minerals are included in the updated train set, the reduction of unknown points due to self-learning can mostly be explained by the decrease of mineral transition zones and due to the better capability of the model to deal with various matrix effects.

Subsequent iterations of self-learning only show minor changes,

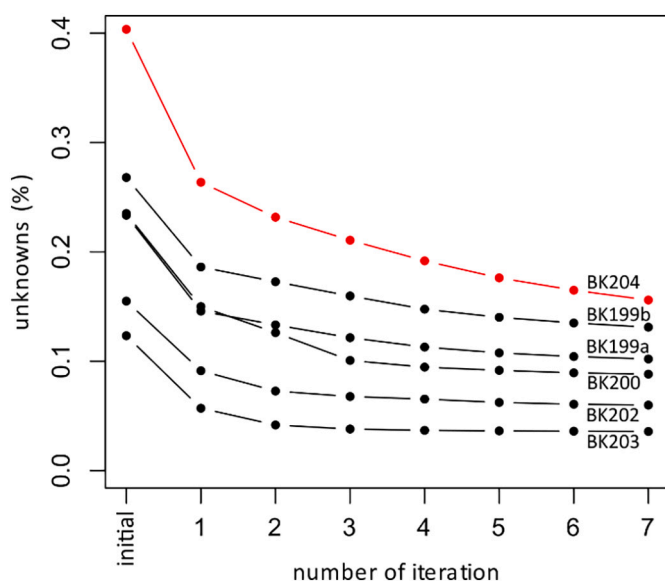


Fig. 13. Remaining percentages of unknown measurement points for the six LIBS mappings for the final classification model without- and after each iteration of self-learning. All LIBS mappings of Spodumene pegmatite are displayed in black, the one of Muscovite pegmatite is displayed in red. (For interpretation of the references to colour in this figure legend, the reader is referred to the web version of this article.)

which reinforces the use of one iteration of self-learning for the classification of the investigated samples. Similar trends are visible for the other LIBS mappings. Samples BK202 and BK203 show the lowest percentages of unknown measurement points, which is due to their large crystal sizes. Sample BK204 on the other hand, displays the highest percentages of unknown points. This sample was taken from the Muscovite pegmatite, which shows an increased porosity, holes and smaller crystal sizes (Fig. 14). The porosities can be traced in the optical image as well as in the first RGB image of Fig. 14, where the dark tracks and light green areas correspond to porosities with varying LIBS intensities. Several coherent areas remain unknown after the first iteration of self-learning. These areas are associated with holes inside and at the border of the right hand side of the sample. They can be identified optically, and by the teal colour in the first RGB image. Spodumene crystals are found inside both holes, which explains the elevated Li I 812.64 nm intensities. As a result of the varying focus depth, their Li intensities differ from spodumene crystals at the plane surface and the specific areas are correctly identified as unknown. Despite high Be II 313.04 nm intensities, the two elongated areas in the centre of the image are not classified as beryl (Fig. 14, second RGB image). Optically, they are associated to fractures and the elevated Be II 313.04 nm intensities are most certainly a result of fluid interactions without the crystallization of beryl. As a result, these areas correctly remain classified as unknown.

### 3.2.4. LIBS drill core profile measurements

The drill core profile measurements were used to validate the SSL classification model's ability to identify a new lithology as unknown. Table 5 shows the classified mineral percentages for every individual lithology, as well as the percentage of data points classified as unknown, using the updated SSL classification model without- and after one iteration of self-learning. After one iteration of self-learning, 99.5% of the Metagreywacke was correctly identified as unknown. The percentages of unknown measurement points in Spodumene and Muscovite pegmatite are in accordance with the results displayed in Section 3.2.3. The increasing number of unknown measurement points after the transition from Spodumene to Muscovite pegmatite is likely a result of the

increased surface porosity in combination with the decreased particle size (i.e. more mixed spectra), which was also observed in Figs. 13 and 14.

Nominative mineral percentages of the Spodumene pegmatite profile measurements were validated with literature values. From all measurement points of the Spodumene pegmatite that were not classified as unknown after the first iteration of self-learning, 26.6% were classified as albite, 21.5% as K-feldspar, 31.0% as quartz, 3.2% as muscovite, and 16.6% as spodumene. Especially the mineral percentage of spodumene is very similar to the mineralogical analysis presented in [47], but also albite, K-feldspar, quartz, and muscovite are in accordance with the percentage ranges defined in the same publication.

### 3.3. General discussion

Reliable quantitative analysis with LIBS can usually only be provided with matrix-matched quantification models and reference samples [14]. With respect to lithium, [39] have also shown that correct quantification results of Li in material with similarly large crystals can only be ensured for minerals that are already included in the train set. With the proposed SSL classification model, it is possible to detect mineral crystals unknown to the train set prior to quantification. Although it has only been demonstrated for pegmatites, a transfer onto various geological materials is likely, and, therefore, the developed SSL classification model may be applied to avoid unreliable predictions in geological LIBS measurements. Self-learning can be particularly helpful to reduce the influence of physical matrix effects on the classification of unknown measurement points in samples with crystal sizes greater than the LIBS laser spot. The developed workflow is especially interesting for geological materials because of the enormous amount of existing minerals and extreme sample heterogeneities. For example, in geological exploration projects, where hundreds of consecutive drill core meters are investigated, incomplete train sets can hardly be avoided. In worst-case scenarios, the predicted concentrations of unknown areas are not conspicuous, although being distorted by matrix effects.

Mixed spectra at mineral transitions were detected as unknown measurement points by the developed SSL model. Their influence on geological classification models has been investigated by [9], who explicitly included both pure and mixed spectra as individual classes. In [25], it was shown that the quantification of mixed spectra is possible, if the mixture components are known and are of distinct mineral chemistry. In the scenario presented in this paper, corresponding endmember could be discovered in the LDA-space and the models could be adapted accordingly.

The developed classification model uniformly labels all unknown minerals as unknown, despite them representing different material. Raman analysis could be added to simplify the task of identifying e.g. unknown accessory minerals. As LIBS, it relies on high-energy lasers and a combination of both techniques is already used for different applications (e.g. in [58–60]), while first attempts use Raman for drill core scanning exist, too [61,62]. After fast profile measurements with LIBS, questionable areas of the drill core that were classified as unknown could be measured with Raman. This would enhance mineral classification of questionable unknowns, which could then be included in the train set for future classification of newly taken drill cores of the same deposit.

## 4. Conclusion

This paper introduces a novel SSL classification model able to classify known minerals and detect material unknown to the train set in LIBS measurements of pegmatitic geological samples. Thereto, LDA and OC-SVM were combined to calculate mineral boundaries for a train set including main and accessory minerals of the investigated sample material (albite, K-feldspar, quartz, muscovite, spodumene, beryl, apatite and a Zn-bearing phase). Unknown data is transformed into the same



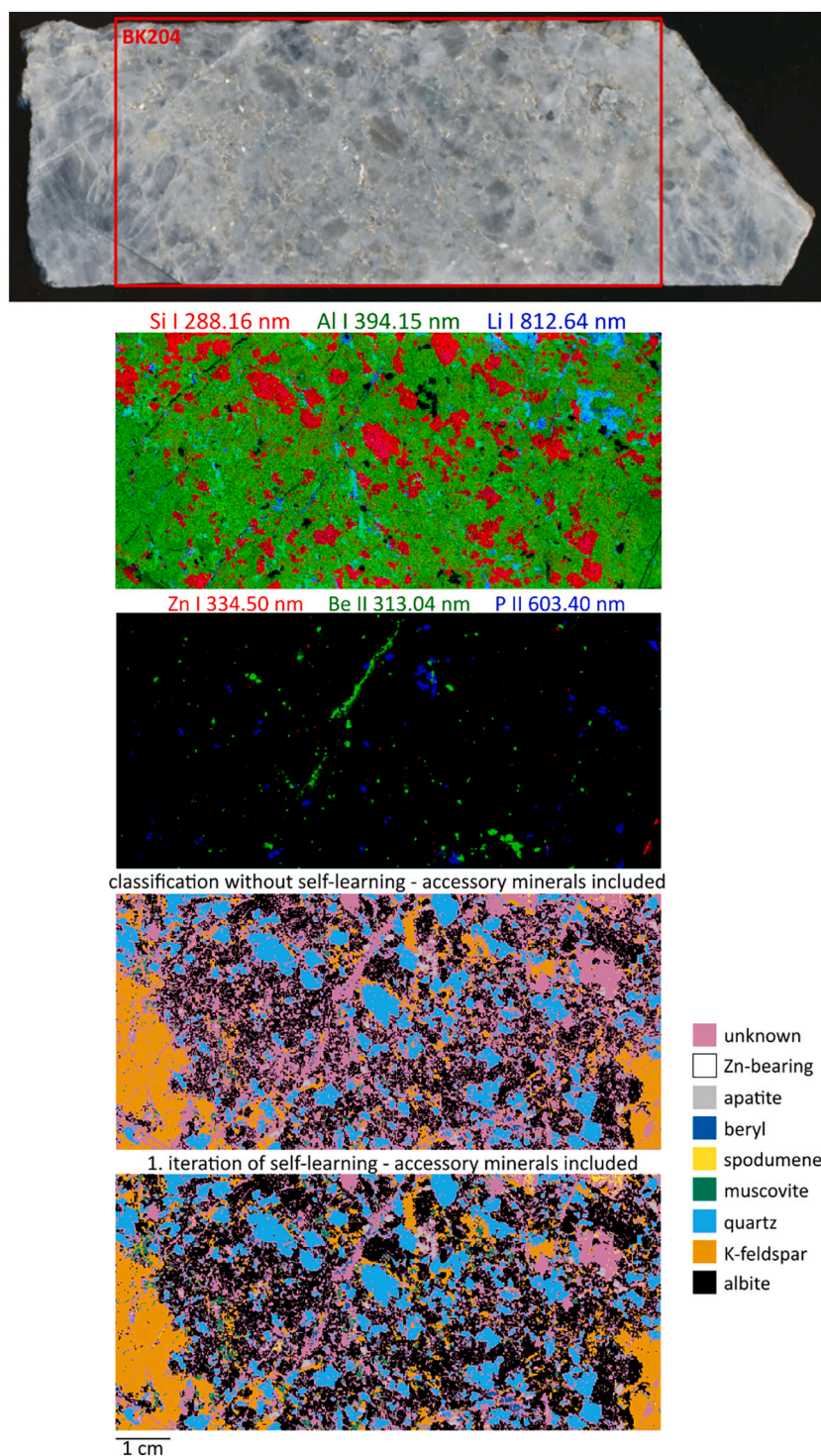


Fig. 14. Muscovite pegmatite mapping BK204 showing the optical image, two LIBS-based RGB images, and the classification results without- and after the first iteration of self-learning.

LDA-space and predictions are made based on mineral boundaries calculated with OC-SVM. To adjust the mineral boundary to the observed LIBS intensity variations, self-learning was applied.

The SSL classification model achieved high classification accuracies for a prepared test set, which included an artificially added class of Metagreywacke, unknown to the train set. Separating the main minerals from each other worked perfectly, whereas two single measurement points of quartz and K-feldspar, as well as a single measurement point of muscovite were classified as unknown due to physical matrix effects.

The Metagreywacke test data were indeed recognized as unknown.

To provide validation results for real life applications, large, spatially detailed LIBS mappings and ten drill core profiles of the same deposit were analysed with the SSL classification model with self-learning. The model achieved reliable classification results for LIBS measurements of the investigated geological drill cores, and its ability to detect known minerals as well as unknown material that is not represented by the train set was proven.

Three different categories of measurement points classified as

**Table 5**

Classification results for every lithology available in the drill cores using the updated classification model without (in brackets) and after the first iteration of self-learning. Numbers represent area-%.

	Spodumene pegmatite	Muscovite pegmatite	Metagreywacke
Albite	20 (14.8)	27 (19.5)	0.2 (0.1)
K-feldspar	16.2 (14.8)	20.1 (18.6)	0 (0)
Quartz	23.3 (22)	17.8 (17.2)	0.3 (0.2)
Muscovite	2.4 (1.7)	1.9 (1.2)	0 (0)
Spodumene	12.5 (10.6)	2.9 (2.2)	0 (0)
Beryl	0.7 (0.4)	0.2 (0.1)	0 (0)
Apatite	0.1 (0.1)	0.1 (0.1)	0 (0)
Unknown	24.8 (35.6)	30 (41.1)	99.5 (99.7)

unknown could be identified: (1) Single pixel inside of large mineral crystals can be wrongly classified as unknown due to physical matrix effects. Their number significantly decreased with self-learning. (2) Mixed spectra at transition zones between two or more different minerals were correctly classified as unknown. Their number decreased with self-learning. (3) Holes, macro porosities, and minerals not represented by the train set were correctly classified as unknown in LIBS mappings and drill core profiles. Their numbers did not change with self-learning.

Self-learning was validated with a pixel-matched reference image of a large LIBS mapping, revealing contradicting behaviour of recall and precision for main minerals and the unknown class. For the investigated material, the best combination of recall and precision was achieved with one iteration of self-learning. The main advantage of self-learning was its ability to overcome physical matrix effects with a limited number of training samples.

## Funding

This research was funded by EIT RawMaterials (T-REX, Nr. 19122) and the German Federal Ministry for Economic Affairs and Energy (Grant Nr. ZF4441001SA7). It contributes to the BGR research project RoSTRaMet.

## Declaration of Competing Interest

The authors declare that they have no known competing financial interests or personal relationships that could have appeared to influence the work reported in this paper.

## Acknowledgements

We thank Dr. Pentti Grönholm from Keliber Oy for providing the drill core material. We thank Dieter Rammlair (BGR) for the mineralogical, lithological and instrumental discussions, as well as Lutz Pfeifer and Sven Merk (both LTB Lasertechnik Berlin) for fruitful discussions on the LIBS technology. Furthermore, we thank Dominic Göricke (BGR) for his support with the LIBS measurements, Khulan Berkh (BGR) for Raman measurements, and the T-REX consortium for the regular exchange.

## References

- C. Fabre, Advances in laser-induced breakdown spectroscopy analysis for geology: a critical review, *Spectrochim. Acta B At. Spectrosc.* 166 (2020), 105799, <https://doi.org/10.1016/j.sab.2020.105799>.
- G. Galbács, A critical review of recent progress in analytical laser-induced breakdown spectroscopy, *Anal. Bioanal. Chem.* 407 (2015) 7537–7562, <https://doi.org/10.1007/s00216-015-8855-3>.
- R.S. Harmon, G.S. Senesi, Laser-induced breakdown spectroscopy – a geochemical tool for the 21st century, *Appl. Geochem.* 128 (2021), 104929, <https://doi.org/10.1016/j.apgeochem.2021.104929>.
- A. Limbeck, L. Brunnbauer, H. Lohninger, P. Pořízka, P. Modlitbová, J. Kaiser, P. Janovszky, A. Kéri, G. Galbács, Methodology and applications of elemental mapping by laser induced breakdown spectroscopy, *Anal. Chim. Acta* 1147 (2021) 72–98, <https://doi.org/10.1016/j.aca.2020.12.054>.
- J. Rakovský, P. Cermák, O. Musset, P. Veis, A review of the development of portable laser induced breakdown spectroscopy and its applications, *Spectrochim. Acta B At. Spectrosc.* 101 (2014) 269–287, <https://doi.org/10.1016/j.sab.2014.09.015>.
- D.W. Hahn, N. Omenetto, Laser-induced breakdown spectroscopy (LIBS), part II: review of instrumental and methodological approaches to material analysis and applications to different fields, *Appl. Spectrosc.* 66 (2012) 347–419, <https://doi.org/10.1366/11-06574>.
- D.W. Hahn, N. Omenetto, Laser-induced breakdown spectroscopy (LIBS), part I: review of basic diagnostics and plasma–particle interactions: still-challenging issues within the analytical plasma community, *Appl. Spectrosc.* 64 (2010) 335A–336A, <https://doi.org/10.1366/000370210793561691>.
- K. Kuhn, J.A. Meima, D. Rammlair, C. Ohlendorf, Chemical mapping of mine waste drill cores with laser-induced breakdown spectroscopy (LIBS) and energy dispersive X-ray fluorescence (EDXRF) for mineral resource exploration, *J. Geochem. Explor.* 161 (2016) 72–84, <https://doi.org/10.1016/j.gexplo.2015.11.005>.
- J.A. Meima, D. Rammlair, Investigation of compositional variations in chromitite ore with imaging laser induced breakdown spectroscopy and spectral angle mapper classification algorithm, *Chem. Geol.* 532 (2020), 119376, <https://doi.org/10.1016/j.chemgeo.2019.119376>.
- S. Müller, J.A. Meima, D. Rammlair, Detecting REE-rich areas in heterogeneous drill cores from Storkwitz using LIBS and a combination of k-means clustering and spatial raster analysis, *J. Geochem. Explor.* 221 (2021), 106697, <https://doi.org/10.1016/j.gexplo.2020.106697>.
- W. Nikonow, D. Rammlair, J.A. Meima, M.C. Schodlok, Advanced mineral characterization and petrographic analysis by  $\mu$ -EDXRF, LIBS, HSI and hyperspectral data merging, *Mineral. Petrol.* 113 (2019) 417–431, <https://doi.org/10.1007/s00710-019-00657-z>.
- S. Rosenwasser, G. Asimellis, B. Bromley, R. Hazlett, J. Martin, T. Pearce, A. Zigler, Development of a method for automated quantitative analysis of ores using LIBS, *At. Spectrosc.* 8 (2001).
- J.-B. Sirven, B. Sallé, P. Mauchien, J.-L. Lacour, S. Maurice, G. Manhès, Feasibility study of rock identification at the surface of Mars by remote laser-induced breakdown spectroscopy and three chemometric methods, *J. Anal. At. Spectrom.* 22 (2007) 1471, <https://doi.org/10.1039/b704868h>.
- J.M. Tucker, M.D. Dyar, M.W. Schaefer, S.M. Clegg, R.C. Wiens, Optimization of laser-induced breakdown spectroscopy for rapid geochemical analysis, *Chem. Geol.* 277 (2010) 137–148, <https://doi.org/10.1016/j.chemgeo.2010.07.016>.
- A. Nardecchia, C. Fabre, J. Cauzid, F. Pelascini, V. Motto-Ros, L. Duponchel, Detection of minor compounds in complex mineral samples from millions of spectra: a new data analysis strategy in LIBS imaging, *Anal. Chim. Acta* 1114 (2020) 66–73, <https://doi.org/10.1016/j.aca.2020.04.005>.
- C. Fabre, M.-C. Boiron, J. Dubessy, A. Chabiron, B. Charoy, T. Martin Crespo, Advances in lithium analysis in solids by means of laser-induced breakdown spectroscopy: an exploratory study, *Geochim. Cosmochim. Acta* 66 (2002) 1401–1407, [https://doi.org/10.1016/S0016-7037\(01\)00858-4](https://doi.org/10.1016/S0016-7037(01)00858-4).
- S. Romppanen, I. Pölonen, H. Häkkinen, S. Kaski, Optimization of spodumene identification by statistical approach for laser-induced breakdown spectroscopy data of lithium pegmatite ores, *Appl. Spectrosc. Rev.* (2021) 1–21, <https://doi.org/10.1080/05704928.2021.1963977>.
- M.T. Sweetapple, S. Tassios, Laser-induced breakdown spectroscopy (LIBS) as a tool for in situ mapping and textural interpretation of lithium in pegmatite minerals, *Am. Mineral.* 100 (2015) 2141–2151, <https://doi.org/10.2138/am-2015-5165>.
- D. Cremers, L. Radziemski, Handbook of Laser-Induced Breakdown Spectroscopy: Second Edition, *Handbook of Laser-Induced Breakdown Spectroscopy: Second Edition*, 2013, <https://doi.org/10.1002/9781118567371>.
- A.W. Miziolek, V. Palleschi, I. Schechter (Eds.), *Laser Induced Breakdown Spectroscopy*, Cambridge University Press, Cambridge, 2006, <https://doi.org/10.1017/CBO9780511541261>.
- T. Takahashi, B. Thornton, Quantitative methods for compensation of matrix effects and self-absorption in laser induced breakdown spectroscopy signals of solids, *Spectrochim. Acta B At. Spectrosc.* 138 (2017) 31–42, <https://doi.org/10.1016/j.sab.2017.09.010>.
- J.M. Anzano, M.A. Villoria, A. Ruíz-Medina, R.J. Lasheras, Laser-induced breakdown spectroscopy for quantitative spectrochemical analysis of geological materials: effects of the matrix and simultaneous determination, *Anal. Chim. Acta* 575 (2006) 230–235, <https://doi.org/10.1016/j.aca.2006.05.077>.
- I. Lopez-Quintas, V. Piñon, M.P. Mateo, G. Nicolas, Effect of surface topography in the generation of chemical maps by laser-induced plasma spectroscopy, *Appl. Surf. Sci.* 258 (2012) 9432–9436, <https://doi.org/10.1016/j.apsusc.2012.04.026>.
- A. Popov, S. Zaytsev, I.V. Seliverstova, A.S. Zakuskin, T.A. Labutin, Matrix effects on laser-induced plasma parameters for soils and ores, *Spectrochim. Acta B At. Spectrosc.* 148 (2018) 205–210.
- J. El Haddad, E.S. de Lima Filho, F. Vanier, A. Harhira, C. Padioleau, M. Sabsabi, G. Wilkie, A. Blouin, Multiphase mineral identification and quantification by laser-induced breakdown spectroscopy, *Miner. Eng.* 134 (2019) 281–290, <https://doi.org/10.1016/j.mineng.2019.02.025>.
- J.A. Bolger, Semi-quantitative laser-induced breakdown spectroscopy for analysis of mineral drill core, *Appl. Spectrosc.* 54 (2000) 181–189.
- D.L. Death, A.P. Cunningham, L.J. Pollard, Multi-element and mineralogical analysis of mineral ores using laser induced breakdown spectroscopy and chemometric analysis, *Spectrochim. Acta B At. Spectrosc.* 64 (2009) 1048–1058, <https://doi.org/10.1016/j.sab.2009.07.017>.
- O. Haavisto, T. Kauppinen, H. Häkkinen, Laser-induced breakdown spectroscopy for rapid elemental analysis of Drillcore, *IFAC Proc. Vol.* 46 (2013) 87–91, <https://doi.org/10.3182/20130825-4-US-2038.00047>.

- [29] K. Kuhn, J.A. Meima, Characterization and economic potential of historic tailings from gravity separation: implications from a mine waste dump (Pb-Ag) in the Harz Mountains Mining District, Germany, *Minerals* 9 (2019) 303, <https://doi.org/10.3390/min9050303>.
- [30] K. Rifai, F. Doucet, L. Özcan, F. Vidal, LIBS core imaging at kHz speed: paving the way for real-time geochemical applications, *Spectrochim. Acta B At. Spectrosc.* 150 (2018) 43–48, <https://doi.org/10.1016/j.sab.2018.10.007>.
- [31] P. Pořízka, A. Demidov, J. Kaiser, J. Keivanian, I. Gornushkin, U. Panne, J. Riedel, Laser-induced breakdown spectroscopy for in situ qualitative and quantitative analysis of mineral ores, *Spectrochim. Acta B At. Spectrosc.* 101 (2014) 155–163, <https://doi.org/10.1016/j.sab.2014.08.027>.
- [32] P. Pořízka, J. Klus, E. Képeš, D. Prochazka, D.W. Hahn, J. Kaiser, On the utilization of principal component analysis in laser-induced breakdown spectroscopy data analysis, a review, *Spectrochim. Acta B At. Spectrosc.* 148 (2018) 65–82, <https://doi.org/10.1016/j.sab.2018.05.030>.
- [33] O. Chapelle, B. Schölkopf, A. Zien, *Semi-Supervised Learning*, MIT Press, Cambridge, Mass. [u.a.], 2010.
- [34] A. Carlson, J. Betteridge, R.C. Wang, E.R. Hruschka, T.M. Mitchell, Coupled semi-supervised learning for information extraction, in: *Proceedings of the Third ACM International Conference on Web Search and Data Mining - WSDM '10*, ACM Press, New York, New York, USA, 2010, p. 101, <https://doi.org/10.1145/1718487.1718501>.
- [35] A. Hussain, E. Cambria, Semi-supervised learning for big social data analysis, *Neurocomputing*. 275 (2018) 1662–1673, <https://doi.org/10.1016/j.neucom.2017.10.010>.
- [36] L. Käll, J.D. Canterbury, J. Weston, W.S. Noble, M.J. MacCoss, Semi-supervised learning for peptide identification from shotgun proteomics datasets, *Nat. Methods* 4 (2007) 923–925, <https://doi.org/10.1038/nmeth1113>.
- [37] K. Yu, T.R. Lin, H. Ma, X. Li, X. Li, A multi-stage semi-supervised learning approach for intelligent fault diagnosis of rolling bearing using data augmentation and metric learning, *Mech. Syst. Signal Process.* 146 (2021), 107043, <https://doi.org/10.1016/j.ymssp.2020.107043>.
- [38] Z. Zhang, E. Pasolli, M.M. Crawford, J.C. Tilton, An active learning framework for hyperspectral image classification using hierarchical segmentation, *IEEE J. Sel. Top. Appl. Earth Observ. Rem. Sens.* 9 (2016) 640–654, <https://doi.org/10.1109/JSTARS.2015.2493887>.
- [39] P. Janovszky, K. Jancsek, D.J. Palásti, J. Kopniczky, B. Hopp, T.M. Tóth, G. Galbács, Classification of minerals and the assessment of lithium and beryllium content in granitoid rocks by laser-induced breakdown spectroscopy, *J. Anal. At. Spectrom.* 36 (2021) 813–823, <https://doi.org/10.1039/D1JA00032B>.
- [40] W.T. Li, Y.N. Zhu, X. Li, Z.Q. Hao, L.B. Guo, X.Y. Li, X.Y. Zeng, Y.F. Lu, *In situ* classification of rocks using stand-off laser-induced breakdown spectroscopy with a compact spectrometer, *J. Anal. At. Spectrom.* 33 (2018) 461–467, <https://doi.org/10.1039/C8JA00001H>.
- [41] D.J. Palásti, A. Metzinger, T. Ajtai, Z. Bozóki, B. Hopp, É. Kovács-Széles, G. Galbács, Qualitative discrimination of coal aerosols by using the statistical evaluation of laser-induced breakdown spectroscopy data, *Spectrochim. Acta B At. Spectrosc.* 153 (2019) 34–41, <https://doi.org/10.1016/j.sab.2019.01.009>.
- [42] G. Vítková, L. Prokeš, K. Novotný, P. Pořízka, J. Novotný, D. Všianský, L. Čelko, J. Kaiser, Comparative study on fast classification of brick samples by combination of principal component analysis and linear discriminant analysis using stand-off and table-top laser-induced breakdown spectroscopy, *Spectrochim. Acta B At. Spectrosc.* 101 (2014) 191–199, <https://doi.org/10.1016/j.sab.2014.08.036>.
- [43] J. Vrábel, E. Képeš, L. Duponchel, V. Motto-Ros, C. Fabre, S. Connemann, F. Schreckenberger, P. Prasse, D. Riebe, R. Junjuri, M.K. Gundawar, X. Tan, P. Pořízka, J. Kaiser, Classification of challenging laser-induced breakdown spectroscopy soil sample data - EMSLIBS contest, *Spectrochim. Acta B At. Spectrosc.* 169 (2020), 105872, <https://doi.org/10.1016/j.sab.2020.105872>.
- [44] G. Bilgin, S. Erturk, T. Yildirim, Segmentation of hyperspectral images via subtractive clustering and cluster validation using one-class support vector machines, *IEEE Trans. Geosci. Remote Sens.* 49 (2011) 2936–2944, <https://doi.org/10.1109/TGRS.2011.2113186>.
- [45] J. Muñoz-Marí, F. Bovolo, L. Gómez-Chova, L. Bruzzone, G. Camp-Valls, Semisupervised one-class support vector Machines for Classification of remote sensing data, *IEEE Trans. Geosci. Remote Sens.* 48 (2010) 3188–3197, <https://doi.org/10.1109/TGRS.2010.2045764>.
- [46] J. Muñoz-Marí, L. Gómez-Chova, G. Camps-Valls, J. Calpe-Maravilla, Image Classification with Semi-Supervised One-Class Support Vector Machine, in: L. Bruzzone, C. Notarnicola, F. Posa (Eds.), Cardiff, Wales, United Kingdom, 2008, p. 71090B, <https://doi.org/10.1117/12.801738>.
- [47] J. Kuusela, T. Ahtola, E. Koistinen, H. Seppänen, T. Hatakka, J. Lohva, *Report of Investigations on the Rapasaaret Lithium Pegmatite Deposit in Kaustinen-Kokkola, Western Finland*, 2011, p. 65.
- [48] T. Ahtola, *Overview of Lithium Pegmatite Exploration in the Kaustinen Area in 2003–2012*, 2015, p. 30.
- [49] J. Rasilainen, P. Eilu, T. Ahtola, T. Halkoaho, N. Kärkkäinen, J. Kuusela, P. Lintinen, T. Törmänen, Quantitative Assessment of Undiscovered Resources in Lithium–Caesium–Tantalum Pegmatite-Hosted Deposits in Finland, 406th ed., Geological Survey of Finland, FI, 2018 <https://doi.org/10.30440/bt406> (Accessed May 3, 2021).
- [50] T. Naes, B.-H. Mevik, Understanding the collinearity problem in regression and discriminant analysis, *Aust. J. Chem.* 15 (2001) 413–426, <https://doi.org/10.1002/cem.676>.
- [51] R.W. Kennard, L.A. Stone, Computer aided design of experiments, *Technometrics*. 11 (1969) 137–148, <https://doi.org/10.1080/00401706.1969.10490666>.
- [52] A. Stevens, L. Ramirez-Lopez, *An Introduction to the Prospector Package*, 2020.
- [53] R Core Team, R: A Language and Environment for Statistical Computing, R Foundation for Statistical Computing, Vienna, Austria, 2018. <https://www.R-project.org/>.
- [54] W.N. Venables, B.D. Ripley, *Modern Applied Statistics with S*, Springer New York, New York, NY, 2002, <https://doi.org/10.1007/978-0-387-21706-2>.
- [55] B.D. Ripley, *Pattern Recognition and Neural Networks*, Cambridge University Press, Cambridge, 1996, <https://doi.org/10.1017/CBO9780511812651>.
- [56] B. Schölkopf, R. Williamson, A. Smola, J. Shawe-Taylor, J. Platt, Support vector method for novelty detection, *Adv. Neural Inf. Process. Syst.* (2000) 582–588.
- [57] D. Meyer, E. Dimitriadou, K. Hornik, A. Weingessel, F. Leisch, e1071: *Misc Functions of the Department of Statistics, Probability Theory Group (Formerly: E1071)*, TU Wien, 2019.
- [58] J. Aramendia, L. Gómez-Nubla, S. Fdez-Ortiz de Vallejuelo, K. Castro, G. Arana, J. M. Madariaga, The combination of Raman imaging and LIBS for quantification of original and degradation materials in cultural heritage, *J. Raman Spectrosc.* 50 (2019) 193–201, <https://doi.org/10.1002/jrs.5546>.
- [59] D. Prochazka, M. Mazura, O. Samek, K. Rebrošová, P. Pořízka, J. Klus, P. Prochazková, J. Novotný, K. Novotný, J. Kaiser, Combination of laser-induced breakdown spectroscopy and Raman spectroscopy for multivariate classification of bacteria, *Spectrochim. Acta B At. Spectrosc.* 139 (2018) 6–12, <https://doi.org/10.1016/j.sab.2017.11.004>.
- [60] K.M.M. Shameem, K.S. Choudhari, A. Bankapur, S.D. Kulkarni, V.K. Unnikrishnan, S.D. George, V.B. Kartha, C. Santhosh, A hybrid LIBS–Raman system combined with chemometrics: an efficient tool for plastic identification and sorting, *Anal. Bioanal. Chem.* 409 (2017) 3299–3308, <https://doi.org/10.1007/s00216-017-0268-z>.
- [61] T. Kauppinen, N. Khajehzadeh, O. Haavisto, Laser-induced fluorescence images and Raman spectroscopy studies on rapid scanning of rock drillcore samples, *Int. J. Miner. Process.* 132 (2014) 26–33, <https://doi.org/10.1016/j.minpro.2014.09.003>.
- [62] M.A. Wells, E.R. Ramanaidou, Raman spectroscopic core scanning for iron ore and BIF characterization, in: F. Dong (Ed.), *Proceedings of the 11th International Congress for Applied Mineralogy (ICAM)*, Springer International Publishing, Cham, 2015, pp. 387–396, [https://doi.org/10.1007/978-3-319-13948-7\\_39](https://doi.org/10.1007/978-3-319-13948-7_39).

Manuscript submitted to Journal of Geochemical Exploration - under review

#### 4. Improving spatially-resolved Lithium quantification in drill core samples of spodumene pegmatite by using laser-induced breakdown spectroscopy and pixel-matched reference samples

**Simon Müller<sup>1,2\*</sup>, Jeannet A. Meima<sup>1</sup>, Hans-Eike Gäbler<sup>1</sup>**

<sup>1</sup>Federal Institute for Geosciences and Natural Resources, Stilleweg 2, 30655 Hannover, Germany

<sup>2</sup>Leibniz Universität Hannover, Welfengarten 1, 30167 Hannover, Germany

\*Corresponding author. E-mail address: [SimonArne.Mueller@bgr.de](mailto:SimonArne.Mueller@bgr.de)

#### KEYWORDS

Laser-Induced Breakdown Spectroscopy (LIBS), laser ablation-inductively coupled plasma-time of flight mass spectrometry (LA-ICP-TOFMS), Least-Square Support Vector Machines (LS-SVM), core scanner, spatial quantification, Li-bearing Spodumene Pegmatite



## Abstract

Lithium is a crucial element for today's technology but difficult to detect with many micro-analytical methods and its quantification during geological exploration is so far mostly performed with bulk analysis on whole rock samples of complete drill core meters. However, quantified spatial Li distributions in drill core samples would support the assessment of local potentials in Li exploration projects. Laser-induced breakdown spectroscopy (LIBS) can be used to detect the spatial distribution of traces of Li in e.g. pegmatitic samples, but physical and chemical matrix effects influence the LIBS spectra, so that especially spatial quantification in samples with varying matrices remains challenging.

To overcome this problem, LIBS datasets were calibrated by quantified laser ablation-inductively coupled plasma-time of flight mass spectrometry (LA-ICP-TOFMS) data. For calibration, both methods were applied on the same sample area and aligned pixel-by-pixel. Different machine learning algorithms were used to calculate multivariate calibration models. As a result, quantified spatial distributions of  $\text{Li}_2\text{O}$ ,  $\text{SiO}_2$ ,  $\text{Al}_2\text{O}_3$ ,  $\text{Na}_2\text{O}$ , and  $\text{K}_2\text{O}$  from LIBS measurements are obtained for spodumene pegmatite drill core samples from the Rapasaari complex in Finland.

A linear Partial Least Square Regression (PLSR) quantification model and a non-linear Least Square Support Vector Machines (LS-SVM) quantification model were built and the results were compared. Root mean square error and  $R^2$  showed improved values for the LS-SVM quantification model for  $\text{Li}_2\text{O}$ ,  $\text{SiO}_2$ ,  $\text{Al}_2\text{O}_3$ ,  $\text{Na}_2\text{O}$  and  $\text{K}_2\text{O}$  and for a varying number of training  $\text{pixel}$  from the pixel-matched reference sample. The LS-SVM model was further validated with an additional test area of the reference sample, showing excellent spatially-resolved quantification results. The calibrated LS-SVM model was then validated with a distinct area of a drill core sample from a different part of the same deposit, which was measured with LA-ICP-TOFMS as well. The spatially-resolved LIBS based concentrations of the independent validation sample show reliable results for  $\text{Li}_2\text{O}$ ,  $\text{SiO}_2$ ,  $\text{Al}_2\text{O}_3$  and  $\text{Na}_2\text{O}$ . Only minor differences were observed for  $\text{Li}_2\text{O}$  and  $\text{Na}_2\text{O}$ , since the reference sample did not cover the complete concentration range of the sample for these elements. Special attention is required for LIBS and its experimental set-up in order to obtain spectra with high signal-to-noise ratios on all relevant lines but no saturation on the K emission lines. In general, it was shown that the combination of LA-ICP-TOFMS and LIBS yields a comprehensive dataset for robust multivariate calibration for spatially-resolved LIBS-based quantification of pegmatite samples that are subject to significant physical and chemical matrix effects.

**Keywords:** Laser-Induced Breakdown Spectroscopy (LIBS); laser ablation-inductively coupled plasma-time of flight mass spectrometry (LA-ICP-TOFMS); Least-Square Support Vector Machines (LS-SVM); core scanner; spatial quantification; Li-bearing Spodumene Pegmatite

## 4.1 Introduction

Lithium is important for modern battery production and the world's demand for Li increased drastically during the last decades (Martin et al., 2017; Maxwell, 2014). Several studies predict continuously rising demands in the future due to ongoing efforts towards electric motorization and increasing consumption of electronic gadgets (Kushnir and Sandén, 2012; Xu et al., 2020). Economically interesting Li-deposits are either bound to brines, magmatic formations or a combination of both (Kesler et al., 2012). Concerning the magmatic ore deposits, pegmatites are the most important rock type, with Li bound to a variety of different Li-bearing minerals, e.g. spodumene, lepidolite, petalite or zinnwaldite (Kesler et al., 2012; Martin et al., 2017). Various Li-bearing minerals may occur in the same deposit, often showing different stages of paragenesis and/or alteration. Together with the large variety of possible mineral assemblages in pegmatites, significant variations in the Li distribution may arise (examples in Sweetapple and Tassios, 2015).

Nevertheless, detecting or quantifying these variations directly on the sample surface is difficult for most analytical techniques like XRF (e.g. in Reed, 2005). As a result, Li concentrations of pegmatites are mostly presented based on bulk analysis of whole rock samples. Due to the variability of Li in pegmatite rock, its spatial quantification would allow the precise identification of Li-rich regions and monitor changes in concentration in drill cores samples. Several analytical techniques can already provide Li distributions in 2D for small samples, but the sample size is limited through the sample chamber and the associated instruments may be difficult to access or impractical to apply (Sweetapple and Tassios, 2015). A promising technology for fast detection of Li is Laser-induced breakdown spectroscopy (LIBS). It has been shown that LIBS can effectively detect even small traces of Li in geological samples in the laboratory (e.g. Fabre et al., 2002; Janovszky et al., 2021; Müller and Meima, 2022; Romppanen et al., 2021; Sweetapple and Tassios, 2015), as well as in the field (e.g. Fabre et al., 2022; Rammelkamp et al., 2021; Wise et al., 2022).

In LIBS analysis, a highly energetic laser beam is focused onto the samples surface, creating a plasma out of the ablated material. The plasma contains the elemental information in the form of light, which is emitted during cooling and collected with optical instruments (Hahn and Omenetto, 2012). Elements show peak intensities at element specific positions of a spectrum, which allows the detection of multiple elements in a single spectrum (Cremers and Radziemski, 2013). The ability to measure under atmospheric conditions with nearly no sample treatment needed makes LIBS an ideal tool for a wide variety of geochemical applications (Harmon and Senesi, 2021), including the fast measurement of large sample areas and even complete drill core meters with high spatial resolution.

Several approaches for LIBS-based drill core scanner applications already exist (e.g. Bolger, 2000; Haavisto et al., 2013; Khajehzadeh et al., 2016; Kuhn et al., 2016; Meima et al., 2022; Müller et al., 2021; Rifai et al., 2018), but LIBS based quantification of heterogeneous material remains challenging due to chemical and physical matrix effects (e.g. in Takahashi and Thornton, 2017). Multivariate calibration can be applied to overcome these effects to some extent and different algorithms have been employed for the quantification of specific elements in geological material with LIBS (e.g. Pagnotta et al., 2020; Rethfeldt et al., 2021). Matrix effects are also very relevant for Li-bearing pegmatites, since severe physical matrix effects exist if different minerals interact with the same laser light (Müller and Meima, 2022). Additionally, the ablation of areas consisting of different minerals and hence the mixing of different chemical matrix effects leads to mixed spectra, which complicate reliable quantification at mineral borders (El Haddad et al., 2019; Meima and Rammlair, 2020). Fabre et al., 2002 were able to quantify Li in single LIBS shots on small spodumene crystals using synthetic glasses. Recently, Fabre et al., 2022 quantified averaged spectra of specific Li-bearing minerals and Rifai et al., 2022 quantified the Li content of crushed spodumene ore with LIBS. Nevertheless Sweetapple and Tassios, 2015 encountered problems for the quantification of spatially detailed LIBS measurements of Li in spodumene pegmatite mappings. Semi-quantitative analysis could still be provided, but the two different reference samples – fused synthetic glass discs and pressed powder pellets – were not compatible with the original rock crystals regarding their matrix effects. A calibration model based on whole rock analysis of homogenized powder samples can be used to quantify homogeneous geological material with similar matrices with LIBS, but the accurate quantification of pure minerals is difficult using this method (Anderson et al., 2011). Therefore, the spatial LIBS-based quantification of pure minerals present in a pegmatitic rock needs a different approach to overcome the spatially resolved variations in physical and chemical matrix effects.

During the last decade, laser ablation-inductively coupled plasma-time of flight mass spectrometry (LA-ICP-TOFMS) has enabled the acquisition of quantitative compositional maps that include all elements with high resolution (Chew et al., 2021) and different geological applications have been published (e.g. Burger et al., 2015; Neff et al., 2020; Rubatto et al., 2020; Stanković et al., 2022; Ubide et al., 2019).

For LA-ICP-TOFMS measurements, sample size is restricted to the sample chamber of the instrument. So far, in several papers, LA-ICP-MS mappings were used to validate LIBS imaging results of geological samples optically (e.g. Chirinos et al., 2014; Novotný et al., 2008), but to our knowledge, no study used LA-ICP-TOFMS mappings as a pixel-matched reference standard for LIBS quantification yet.

The goal of this paper was to develop a LIBS application for the accurate quantification of Li and other rock-forming elements in different main minerals of spodumene pegmatite drill core samples. In order to deal with the severe matrix effects in the pegmatite material, LIBS and LA-ICP-TOFMS measurements were superimposed to create a pixel-matched reference sample, which was used for the spatial quantification of Li and other rock-forming elements by applying a linear Partial-Least-Square Regression (PLSR) and a non-linear Least-Square Support Vector Machine (LS-SVM) model. The LS-SVM calibration model was further validated with another 2D scan of a sample from the same deposit from a different part of the drill core.

## 4.2 Material and Methods

### 4.2.1 Sample material

The investigated samples cover spodumene pegmatite from a 10 m long drill core from the Rapasaari lithium deposit, which is part of the Kaustinen lithium pegmatite province in Finland. They are part of the drill cores investigated in Müller and Meima, 2022, where detailed information can be found. The Li-bearing spodumene pegmatite shows average  $\text{Li}_2\text{O}$  concentrations of 1.18 wt.%, mainly bound to spodumene minerals ( $\text{LiAlSi}_2\text{O}_6$ ) with average  $\text{Li}_2\text{O}$  concentrations of 7.21 wt.% (Kuusela et al., 2011). Additional main minerals of the spodumene pegmatite are albite ( $\text{Na}[\text{AlSi}_3\text{O}_8]$ ), K-feldspar ( $\text{K}[\text{AlSi}_3\text{O}_8]$ ), quartz ( $\text{SiO}_2$ ), and muscovite ( $\text{KAl}_2[(\text{OH}, \text{F})_2|\text{AlSi}_3\text{O}_{10}]$ ), as well as the accessory minerals apatite, zinnwaldite, Nb-Ta-oxides, beryl, garnet (grossular), arsenopyrite, and sphalerite (Ahtola, 2015; Kuusela et al., 2011; Rasilainen et al., 2018). Crystal sizes range from 0.5 cm to several centimetres and especially spodumene and albite show large crystals with lengths of up to 10 cm (Ahtola, 2015; Kuusela et al., 2011; Rasilainen et al., 2018).

The measured area of the reference sample BK203\_S12 covers 1.0 x 2.5 cm in size and was extracted from a representative part of the drill core. It contains four of the five main minerals, i.e. albite, muscovite, quartz, and spodumene with varying distributions. K-feldspar is missing in this particular area of the sample. Additionally, two small crystals of the accessory mineral apatite were found. This sample was used as the pixel-matched reference sample as described in sections 2.2 – 2.4. Thereto, it was mapped with LIBS (first) and LA-ICP-TOFMS (second). The LIBS mapping covers a larger area of the sample, fully including the surface that was measured with LA-ICP-TOFMS afterwards.

Sample BK200 is an independent piece from a different location of the spodumene pegmatite drill core. It covers 4.8 x 5.3 cm in size and shows a similar mineral distribution as sample BK203\_S12. However, at specific positions of BK200 the main mineral K-feldspar and the two accessory minerals beryl and apatite appear. The whole sample surface was mapped with LIBS and a reference area of 0.76 x 4.3 cm was measured with LA-ICP-TOFMS as well. The measurements of sample BK200 represent an independent sample from a different part of the drill core and were thereby used to analyse and validate the developed quantitative LIBS-based mapping tool applied on an unknown drill core sample of the same deposit.

### 4.2.2 LA-ICP-TOFMS measurements and pre-processing

Quantified element distribution maps were obtained by laser ablation-inductively coupled plasma-time of flight mass spectrometry (LA-ICP-TOFMS) from rock samples previously analysed by LIBS. The applied LA-ICP-TOFMS system is described in Stanković et al., 2022. It uses the 193 nm laser ablation system IRIDIA (Teledyne CETAC Technologies, Omaha, USA), which is equipped with a fast washout Cobalt Sample Cell and an Aerosol Rapid Introduction System (ARIS). The laser ablation system is

coupled to an icpTOF 2R inductively coupled plasma-time of flight mass spectrometer from TOFWERK AG, Thun, Switzerland. The laser ablation system is controlled by the software Chromium 2.7 (Teledyne CETAC Technologies, Omaha, USA) while the mass spectrometer is controlled by the software TOFpilot (TOFWERK AG, Thun, Switzerland). Helium is used for the transport of the ablated material into the torch of the mass spectrometer. The ICP-TOFMS was operated with a tune setting that covers the mass range from 7 to about 90 amu. A square 10  $\mu\text{m}$  or 20  $\mu\text{m}$  spot was used for ablation of sample material at a fluence of 6.0, 7.2, or 9.0  $\text{J}/\text{cm}^2$  with a repetition rate of 50, 80, or 120 Hz and a dosage of 1 pulse/spot resulting in a scan speed of 1.0, 1.2, or 1.6 mm/s. In this way 475-900 lines of about 25 to 43 mm in length were gapless ablated for a single map. Ten to 25 gas blanks and 10-25 lines on a calibration material (CM) were recorded at equally distributed time intervals together with the sample. The reference material GSE-1G (United States Geological Survey, Denver, USA) was used as CM.

The HDIP software (Teledyne CETAC Technologies, Omaha, USA) was used to process the raw data of the TOF instrument. Based on the recorded gas blanks, background correction was performed and element distribution maps in counts per seconds (cps) were calculated. The records of the CM were used to calculate calibration functions, which were applied on the sample data to obtain concentration-related element distribution maps. Sum normalisation of the previously external calibrated concentrations was applied to account for different ablation yields of sample and CM. In the sum normalisation step the sum of  $\text{Li}_2\text{O}$ ,  $\text{Na}_2\text{O}$ ,  $\text{MgO}$ ,  $\text{Al}_2\text{O}_3$ ,  $\text{SiO}_2$ ,  $\text{K}_2\text{O}$ ,  $\text{MnO}$ , and  $\text{Fe}_2\text{O}_3$  was normalised to 100%.

Only very little material is ablated from quartz crystals during the LA-ICP-TOFM ablation process. As a result, background correction and sum normalisation can lead to unrealistic concentrations of specific quartz pixel. This problem was mainly solved during the image registration process described in section 2.4.

### 4.2.3 LIBS measurements and spectral processing

The LIBS measurements were performed with a drill core scanner prototype developed by Lasertechnik Berlin (LTB) in 2011. It operates with a Q-switch Nd:YAG laser (20 Hz repetition rate, 11 ns pulse duration, 1064 nm excitation wavelength, 35 mJ laser energy and 200  $\mu\text{m}$  spot size), an Echelle spectrometer (285-964 nm spectral range and 0.029-0.096 nm resolution) and a charge coupled device (CCD). Spectrometer and CCD are held at a constant temperature of 27  $^\circ\text{C}$  to avoid spectral shifts during longer measurements. The laser can move up to 100 cm in X and 2.5 cm in Y direction. To prevent cross-crater contamination and the ionization of small dust particles between laser head and focus point, an exhaust system moves alongside the laser. Parameter optimization for all samples was based on signal-to-noise ratio of the major rock forming elements present in the main minerals of the Rapasaari complex. More details can be found in Müller and Meima, 2022.

For the detailed 2D-scans, gapless point measurements (200  $\mu\text{m}$ ) were performed shot-by-shot, accumulating three shots at each position. A 1 s pause is necessary to save the data, before the laser moves to the next measurement position. This results in a scan speed of 0.2 mm/s. Both samples BK203\_S12 and BK200 were mapped with LIBS in detail. Figure 1 shows selected spectra for pure phases of four main minerals found in sample BK203\_S12, i.e. spodumene, albite, quartz, and muscovite. Mineral specific element peaks are highlighted in the spectra. For further analysis, 37 element specific emission lines were extracted from every spectrum using peak integration with an integration window of 0.1 nm for wavelengths below 600 nm and 0.15 nm for wavelengths above 600 nm, respectively. The selection is shown in Table 1 and based on the stoichiometry of the main minerals (section 2.1) and potential accessory minerals. To minimize shot-to-shot variations, all emission lines were normalised using the total intensity of the corresponding spectrum.



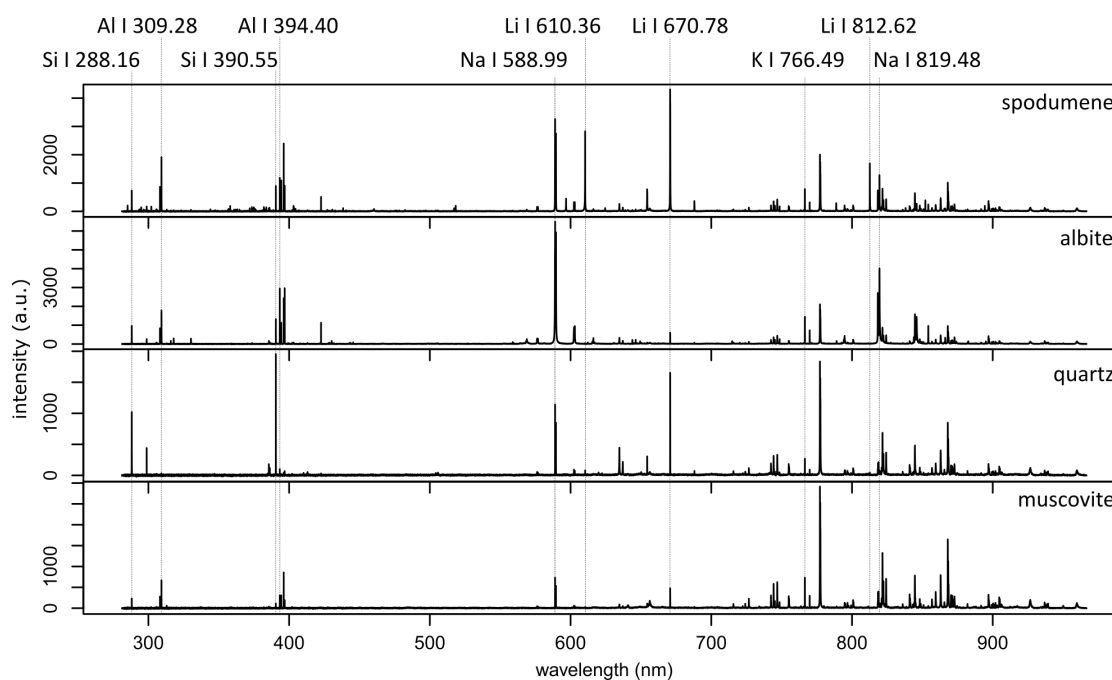


Figure 1: Selected spectra of spodumene, albite, quartz, and muscovite, taken from sample BK203\_S12.

Table 1: Extracted emission lines used for the quantification models.

Element	Spectral line (nm)
Al I	309.28, 394.40, 396.15
Be II	313.04, 313.11
Ca I	430.25
Ca II	315.89, 396.85
F I	685.60
Fe I	358.12, 371.99, 373.49
K I	766.49, 769.90
Li I	610.36, 670.78, 812.62
Mg I	285.21, 517.27, 518.36
Mn I	403.08, 403.31
Mn II	294.92
Na I	588.99, 818.33, 819.48
P II	603.40, 604.31
Si I	288.16, 390.55
Si II	634.71
Ti II	308.80, 336.12, 337.28
Zn I	330.25, 334.50, 472.22

#### 4.2.4 Image registration workflow

LIBS and LA-ICP-TOFMS datasets were obtained from the same sample areas, but due to the use of different instruments with different sample stages the datasets have to be superimposed to obtain pixel-matched datasets. This process is called image registration. Thereto, hyperspectral data cubes of both datasets were generated. In the data cubes, each pixel represents a single measurement point and each image gives the concentration distribution of a specific element (LA-ICP-TOFMS) or the normalised intensity distribution of the target emission line (LIBS), respectively. This allows straightforward visualization using the ENVI image analysis software (version 5.5). LIBS and LA-ICP-TOFMS measurements show offsets to various degrees, and lateral shifts and rotation were necessary to overlap both datasets pixel by pixel. Thereto, the following steps were executed in ENVI:

- (1) The resolution of all LA-ICP-TOFMS images was adjusted to the LIBS pixel size of 200  $\mu\text{m}$ . Thereto, the median concentration of 10 x 10 (20  $\mu\text{m}$  square) or 20 x 20 (10  $\mu\text{m}$  square) LA-ICP-TOFMS pixels was determined and used as the representative concentration for all involved pixels. By using the median concentration, unrealistic LA-ICP-TOFMS concentrations of specific quartz pixel (see section 2.2) were mostly avoided.
- (2) The LIBS images were cut to match the area covered by the LA-ICP-TOFMS measurement as close as possible.
- (3) Three tie points were selected for image registration of sample BK203\_S12 and sample BK200 for ENVI's built-in image registration tool. Every tie point covers an identical pixel in LA-ICP-TOFMS and LIBS images.
- (4) Using ENVI's rotation, scaling and translation (RST) algorithm, overlapping areas of the LA-ICP-TOFMS data cube were warped onto the LIBS images based on the tie points selected in (3).
- (5) After image registration, a moving window with a 3 x 3 kernel was applied to both datasets. Thereto, the intensity/concentration values of the central pixel were averaged using all nine pixels of the window. Padding was used to prevent size reduction at the edges. This filter smooths the images and reduces the possibility of miss-fitted pixel at mineral borders.

LA-ICP-TOFMS calibration was performed on silicates only. Since small areas of the samples BK203\_S12 and BK200 appear to consist of apatite, these pixels were removed from both pixel-matched datasets. Thereto, all pixels with  $\text{P}_2\text{O}_5$  concentrations above 10 wt.% were discarded. Additionally, 82 quartz pixels of sample BK200 still showed unrealistic LA-ICP-TOFMS concentrations after step (1) of the image registration process. These pixels were discarded as well.

#### 4.2.5 LIBS-based quantification models and the creation of train- and test sets

Two different sets of test data were provided for validation. Thereto, the pixel-matched datasets of BK203\_S12 were spatially divided according to Figure 2. The larger area (BK203\_S12a, covering 4416 pixels) was used to build train- and test sets for model creation. The smaller area (BK203\_S12b, covering 1900 pixels) provides an additional independent test area for model validation purposes.

To investigate the influence of varying numbers of train pixels on the quantification model, ten different train sets were created from BK203\_S12a, covering 100, 150, 200, 250, 500, 750, 1000, 1250, 1500 and 2000 pixels, respectively. Thereto, the predefined number of pixels was selected with the Kennard-Stone algorithm (Kennard and Stone, 1969), included in the 'prospector' package in R (Stevens and Ramirez-Lopez, 2020). It was applied to the normalised LIBS intensities and ensures that the complete intensity range is covered in every train set. The 2416 pixels that were not included in the 2000 pixels train set were used as the test set for all studied train sets of different sizes. Afterwards, the final pixel-matched model was applied to all 1900 pixels of BK203\_S12b for additional validation.

BK203\_S12a and BK203\_S12b both include the same minerals, as displayed in the classified image in Figure 2.

The two algorithms PLSR and LS-SVM regression were compared to evaluate the performance of a linear (PLSR) and a non-linear (LS-SVM) quantification model based on the pixel-matched reference sample. The open-source software R, version 3.6.3 (R Core Team, 2018), was applied for all calculations.

PLSR is a multivariate method widely used to quantify a variety of geological materials with LIBS (e.g. Clegg et al., 2009; Tucker et al., 2010; Ytsma and Dyar, 2019). It models the relationship and structure of the two matrices  $X$  (matrix of predictors) and  $Y$  (matrix of responses), extending the traditional multiple regression approach. This enables good quantification results, even if noisy or collinear variables are used as input. For further information on the method itself, we refer to Wold et al. (2001). We applied the PLS2 algorithm in the R package pls (Mevik and Wehrens, 2021). The PLSR-model was tuned by hand for every train set independently, and 5 latent variables were applied for every train set. The data was scaled and centred; cross validation was used to fit the PLSR model.

LS-SVM is an extension of the conventional SVM algorithm, but linear equations are used to solve the optimization problem, instead of quadratic programming. It was introduced by Suykens and Vandewalle (1999) and we refer to their paper for a detailed explanation. We used the algorithm included in the R package liquidSVM (Steinwart and Thomann, 2017) to create the quantification model for the scaled data. This LS-SVM algorithm uses the Radial Basis Kernel and tunes its parameters gamma and lambda for each element automatically, using a two-dimensional grid with a range of 0.1677 to 6.3357 and 0.000001250 to 0.01 for gamma and lambda, respectively.

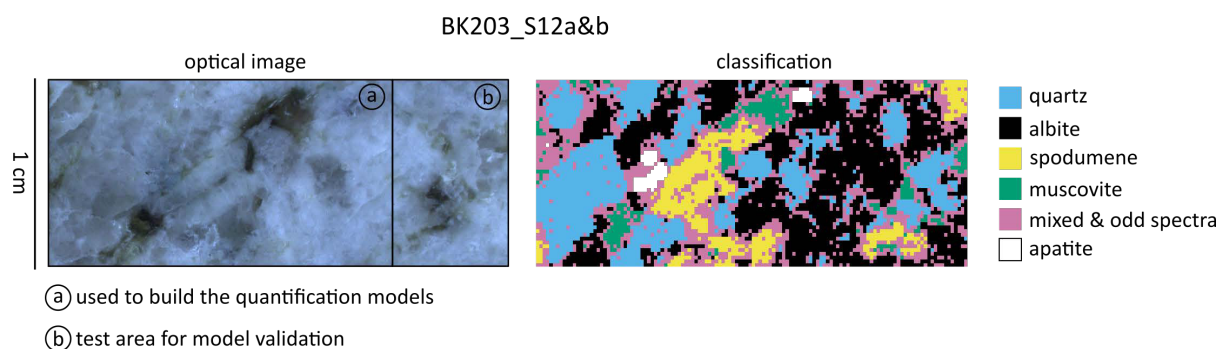


Figure 2: Optical image and classification result for sample BK203\_S12. The optical image shows two areas, used for model creation (BK203\_S12a) and additional validation (BK203\_S12b). The classification results were obtained using the SSL classification model presented in Müller et al. 2022.

## 4.3 Results and Discussion

### 4.3.1 Comparing LA-ICP-TOFMS and LIBS datasets of reference sample BK203\_S12

To evaluate the image registration process for reference sample BK203\_S12 presented in section 2.4, the LA-ICP-TOFMS dataset was compared to the LIBS dataset in terms of pixel-matching. Figure 3 shows the pixel-matched images for normalised LIBS intensities of selected emission lines (left) and corresponding LA-ICP-TOFMS oxide concentrations (right) of the same element. The pixel-matched images of Si, Li and Na display high similarities for all minerals, where areas with high normalised LIBS intensities overlap with high concentrations of  $\text{SiO}_2$ ,  $\text{Li}_2\text{O}$  and  $\text{Na}_2\text{O}$ , respectively.  $\text{K}_2\text{O}$  displays a good correlation for most parts of the image, although some pixels show elevated normalised LIBS intensities, while the correlated concentrations are low. Contrary behaviour is seen for  $\text{Al}_2\text{O}_3$ . While areas with small and medium concentrations of  $\text{Al}_2\text{O}_3$  overlap with low normalised LIBS intensities of Al I 394.40 nm, several muscovite crystals (see classification in Figure 2) show the anticipated, high

concentrations of  $\text{Al}_2\text{O}_3$ , but no increase in the normalised LIBS intensity of Al I 394.60 nm can be observed. This is true for all extracted Al lines. Since  $\text{Al}_2\text{O}_3$  concentrations of albite, quartz-, and spodumene crystals are correlated with their corresponding normalised LIBS intensities, it is assumed that different optical properties of muscovite can result in matrix effects. This is supported by Figure 2, in which muscovite crystals of sample BK203\_S12 are associated with a dark brown colour, whereas spodumene, quartz and albite appear grey.

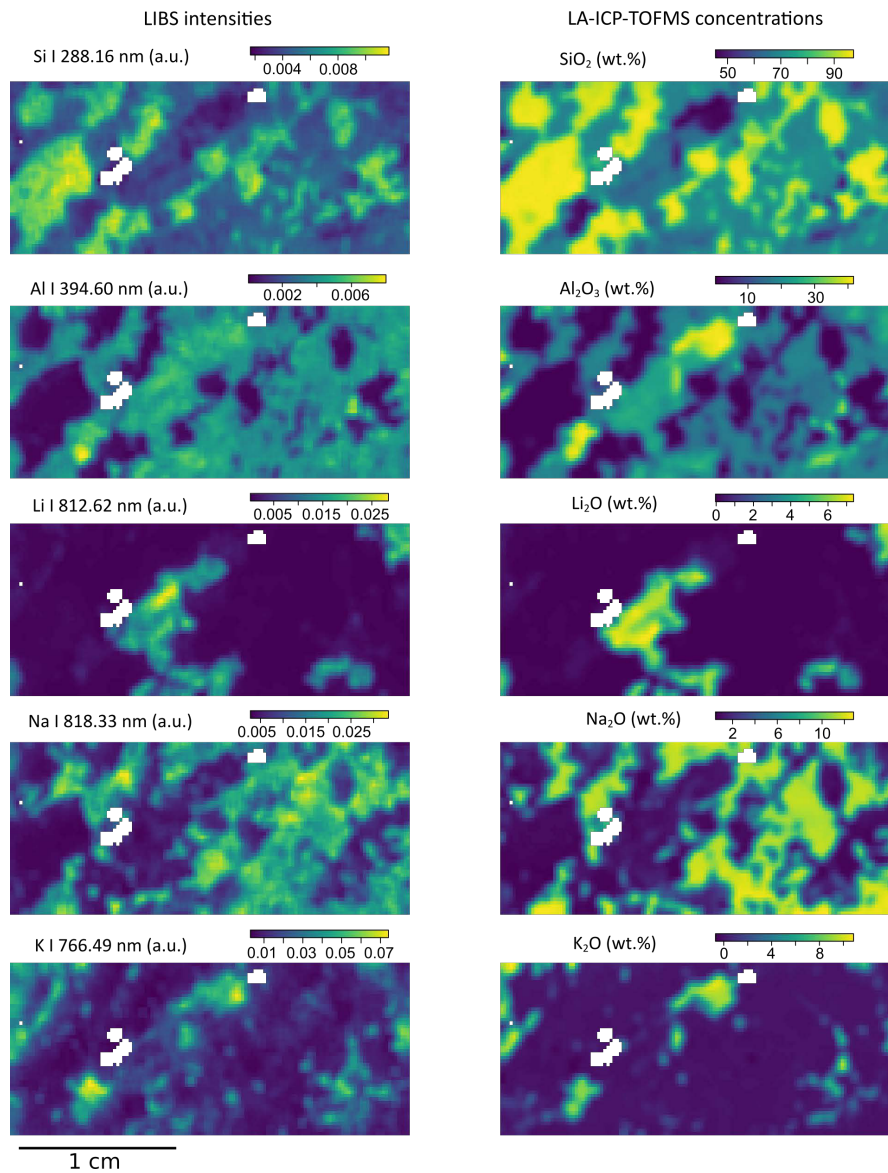


Figure 3: Comparison of different elements of the LIBS and the LA-ICP-TOFMS dataset for sample BK203\_S12 after the image registration process described in section 2.4. The left images show normalised LIBS intensities, the right images show oxide concentrations of the same elements, measured with LA-ICP-TOFMS. The missing white pixel correspond to apatite crystals, which were excluded from the calibration model.

To evaluate the degree of pixel matching, correspondence factors between normalised LIBS intensities and LA-ICP-TOFMS concentrations were calculated for Si and Li pixel by pixel after Hoekzema et al., 1998. A correspondence factor of 1 indicates a perfect positive correlation of every pixel of the two datasets and with correspondence factors of 0.91 for Si and 0.97 for Li, both elements display a high degree of correlation. This indicates a successful image registration of LIBS and LA-ICP-TOFMS measurement. The pixel-matched datasets were therefore used to build the quantification models.

### 4.3.2 Comparing PLSR and LS-SVM results for sample BK203\_S12a for varying numbers of train pixels

The root mean square error (RMSE) and the coefficient of determination  $R^2$  are measures that describe the deviation of modelled values from reference values and the accuracy of the linear fitting, respectively. In combination, both figures of merit indicate how well model results fit to observed values (Takahashi and Thornton, 2017). Based on these indices, different models can be compared if RMSE and  $R^2$  are calculated for an identical test set. As the number of train pixels obviously influences model quality, this parameter is evaluated as well. Figure 4 displays the development of RMSE and  $R^2$  with increasing numbers of train pixels based on the identical test set. Results are shown for  $\text{Li}_2\text{O}$ ,  $\text{SiO}_2$ ,  $\text{Al}_2\text{O}_3$ ,  $\text{Na}_2\text{O}$  and  $\text{K}_2\text{O}$  for the PLSR and LS-SVM models that have been developed as described in section 2.5. For interpretation purposes, the LA-ICP-TOFMS concentration range of every element is shown at the top. For LS-SVM,  $R^2$  values are continuously increasing and RMSE values are continuously decreasing with an increasing number of train samples. Especially  $\text{Na}_2\text{O}$  and  $\text{K}_2\text{O}$  show significant improvements using a larger number of train samples.

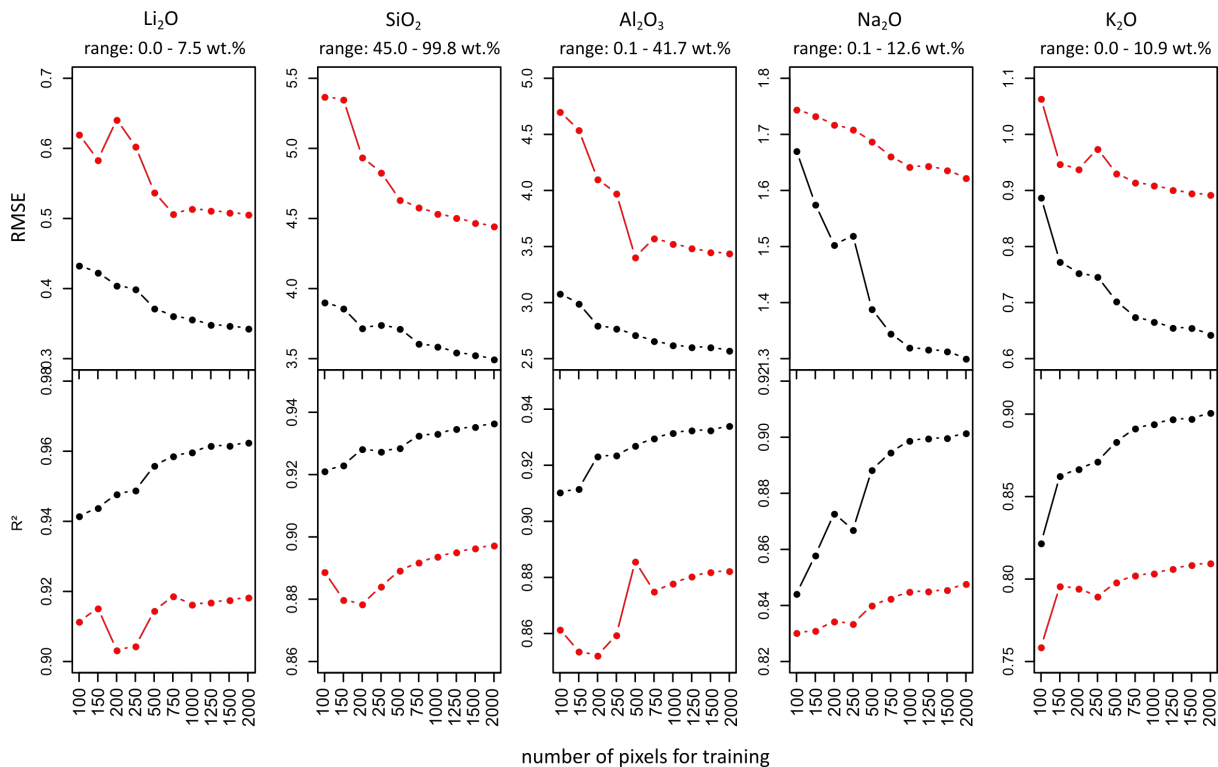


Figure 4: Development of RMSE (top) and  $R^2$  (bottom) with increasing numbers of train pixels for  $\text{Li}_2\text{O}$ ,  $\text{SiO}_2$ ,  $\text{Al}_2\text{O}_3$ ,  $\text{Na}_2\text{O}$  and  $\text{K}_2\text{O}$  for LS-SVM (black) and PLSR (red). Results are based on an identical set of test pixels extracted from sample BK203\_S12a (Figure 2), as explained in section 2.5.

Figure 4 shows that the non-linear LS-SVM algorithm outperforms linear PLSR for every train set and every element. Increasing the number of PLS components for the PLSR model did not change this observation. For PLSR, RMSE values do not continuously decrease and/or  $R^2$  continuously increase with an increasing number of train pixel for  $\text{Li}_2\text{O}$ ,  $\text{Al}_2\text{O}_3$  and  $\text{K}_2\text{O}$ . This may be explained by the fixed number of 5 PLS components that was applied throughout the tests, since the optimal number of PLS components may vary from element to element and from experiment to experiment. Overall, the non-linear function build by LS-SVM is able to model the relationship of LIBS intensities of the different minerals and their concentrations significantly better than PLSR, which results in the improved RMSE and  $R^2$  values. In the presented example, a single LS-SVM or PLSR model was used for the complete concentration range. Further enhancements for PLSR, therefore, could probably be achieved, if



different models would be created for different concentration ranges (Anderson et al., 2017). Here, the non-linear function is clearly advantageous in the presented example, because it needs only one model for the whole concentration range.

Due to the numerous possible physical matrix effects and different transition zones between minerals, a large number of train pixel can result in better RMSE and  $R^2$  values. For most elements, lowest RMSE and highest  $R^2$  are received using the maximum applied number of 2000 train pixels. Compared to the train sets with 100 to 250 train pixel, the 500 train pixel LS-SVM model shows significant improvements especially for  $\text{Na}_2\text{O}$  and  $\text{K}_2\text{O}$ , slowly improving further until only minor changes are displayed for more than 1000 pixels. To provide a generalizable model, the smallest number of necessary train samples should be used for future applications. Here, 1000 train pixel show very good results and only small improvements are made using even more pixel for training. Therefore, the quantification model with 1000 train pixel was used for further investigations.

#### 4.3.3 Quantification results of the LS-SVM model for sample BK203\_S12b

To evaluate the LS-SVM model for an adjacent test area not involved in model creation, LIBS-based concentrations of sample BK203\_S12b (Figure 2) were determined and compared to the LA-ICP-TOFMS results. Figure 5 shows the LIBS-based concentration images and reference mappings for  $\text{Li}_2\text{O}$ ,  $\text{SiO}_2$ ,  $\text{Al}_2\text{O}_3$ ,  $\text{Na}_2\text{O}$  and  $\text{K}_2\text{O}$ . Overall, good agreement is observed, and areas with high LA-ICP-TOFMS concentrations display similarly high LIBS-based concentrations for all investigated elements. Especially the observed drop of the normalised LIBS intensity on muscovite crystals (see section 3.1) does not have any significant effect on the LS-SVM calibrated  $\text{Al}_2\text{O}_3$  concentrations obtained by LIBS anymore. This demonstrates one advantage of a multivariate calibration approach.

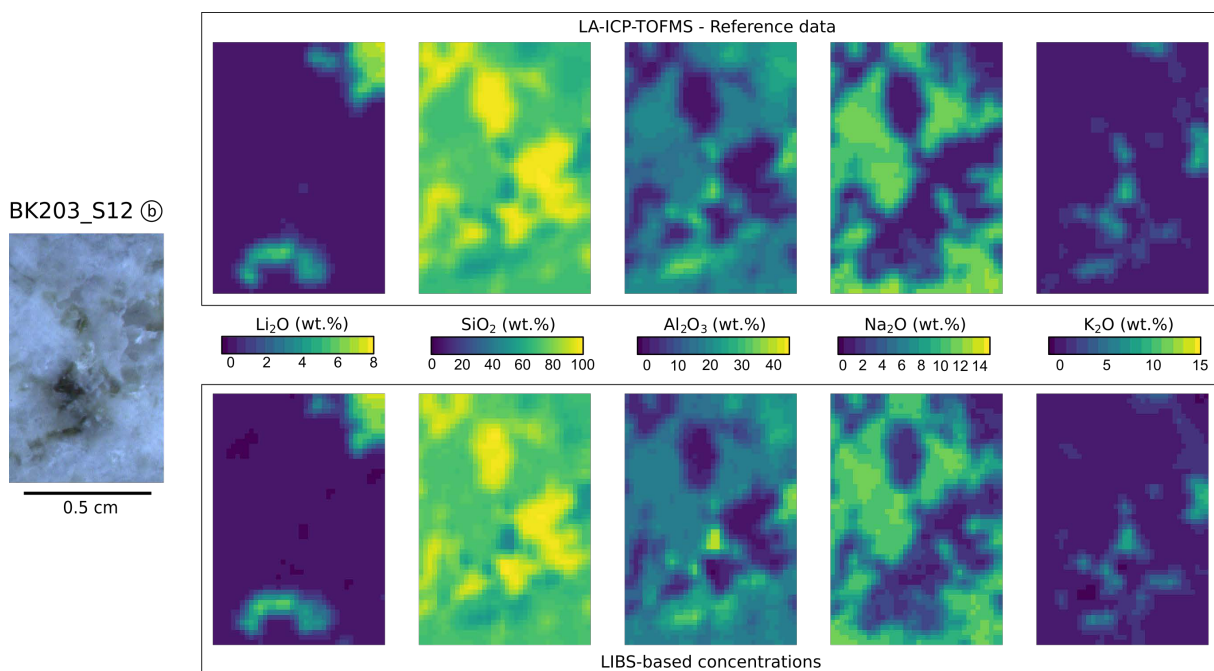


Figure 5: Modelled LIBS-based concentrations of  $\text{Li}_2\text{O}$ ,  $\text{SiO}_2$ ,  $\text{Al}_2\text{O}_3$ ,  $\text{Na}_2\text{O}$  and  $\text{K}_2\text{O}$  for sample BK203\_S12b (bottom), compared to LA-ICP-TOFMS reference concentrations of the same area (top). The optical image is shown on the left for comparison.

The promising results of Figure 5 are supported by the scatterplots shown in Figure 6, which display the LIBS-based concentrations and the corresponding LA-ICP-TOFMS reference values for every individual pixel of sample BK203\_S12b. Every pixel is coloured according to the classification result shown in Figure 2. According to their associated class, quartz pixels show high  $\text{SiO}_2$  values, spodumene pixel high  $\text{Li}_2\text{O}$  concentrations. Muscovite pixels are high in  $\text{K}_2\text{O}$ , whereas albite shows highest  $\text{Na}_2\text{O}$  values. Most pixels that are classified as pure minerals show results that fit well to their stoichiometric

element concentrations. Nevertheless, several points classified as spodumene show  $\text{Li}_2\text{O}$  concentrations below 6 wt.%, although microprobe point measurements of spodumene from the same deposit only yielded values above 6 wt.%  $\text{Li}_2\text{O}$  (Kuusela et al., 2011). Due to the moving window applied in section 2.4, concentrations of formerly pure spodumene pixels are mixed with their surrounding material at mineral borders. Therefore, some pixel classified as spodumene show  $\text{Li}_2\text{O}$  concentrations below 6 wt.%.

A clear correlation between the LIBS-based concentrations and the LA-ICP-TOFMS reference values is observed for pure minerals and all elements. Especially  $\text{Li}_2\text{O}$ ,  $\text{SiO}_2$  and  $\text{Al}_2\text{O}_3$  follow the regression line closely.

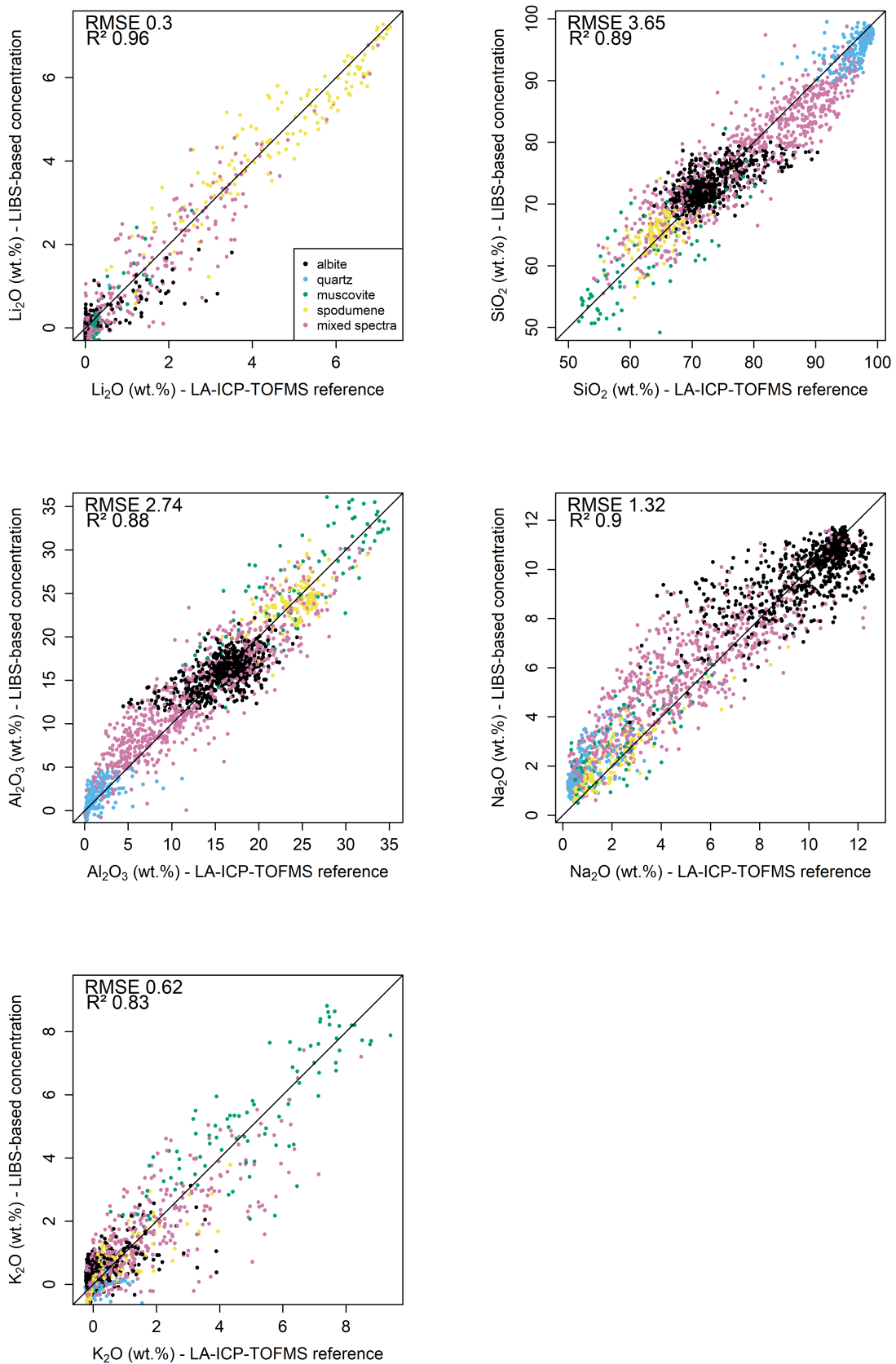


Figure 6: LIBS-based concentrations and reference values for every pixel of the independent test area of sample BK203\_S12b. The pixels are coloured according to the classification result shown in Figure 2.

#### 4.3.4 Transferability of the LIBS LS-SVM calibration model onto sample BK200

The LS-SVM calibration model was applied to the drill core sample BK200 to test its performance on a different sample of the same deposit. A rectangular area of this sample (Figure 7) was mapped by LA-ICP-TOFMS for validation.

Sample BK200 contains small crystals of K-Feldspar. To account for this mineral in the train set, additional areas from the original hand specimen of sample BK203\_S12 covering only K-Feldspar were selected. These areas were measured with LIBS and LA-ICP-TOFMS (using the same instrument settings as described in sections 2.2 and 2.3), pixel-matched, and added to the train set. An updated LS-SVM calibration model was calculated and applied on the LIBS data for sample BK200. Figure 7 displays an optical image of sample BK200, highlighting the area that was measured with LA-ICP-TOFMS for validation purposes. Modelled LIBS-based and LA-ICP-TOFMS distribution maps for  $\text{Li}_2\text{O}$ ,  $\text{SiO}_2$ ,  $\text{Al}_2\text{O}_3$ ,  $\text{Na}_2\text{O}$  and  $\text{K}_2\text{O}$  are shown and compared as well.

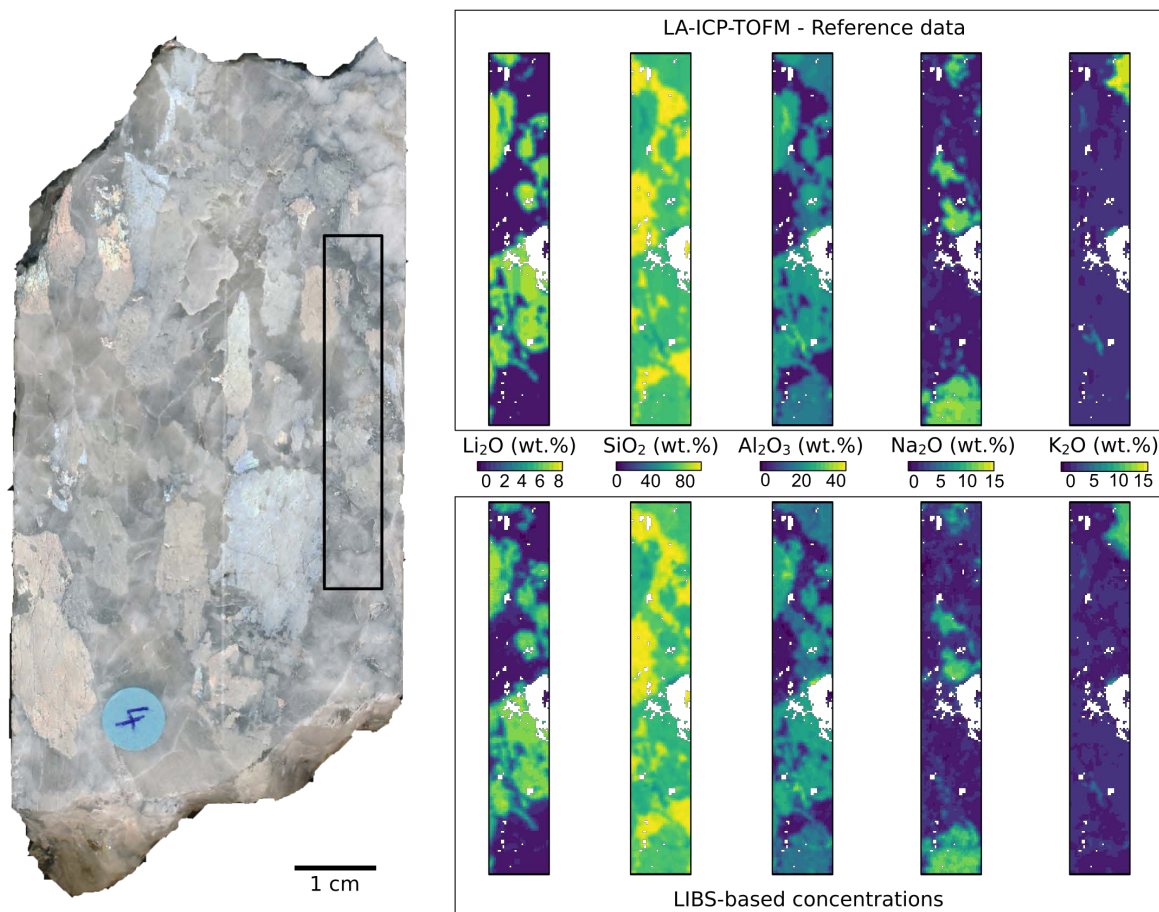


Figure 7: Optical image of sample BK200, LIBS-based concentrations, as well as LA-ICP-TOFMS reference values for the highlighted rectangle. The missing values correspond to apatite and unrealistic LA-ICP-TOFMS concentrations for quartz pixels (see section 2.4).

LIBS-based and LA-ICP-TOFMS concentrations of  $\text{SiO}_2$  and  $\text{Al}_2\text{O}_3$  are in excellent agreement, and only minor deviations between the calibrated LS-SVM model and the LA-ICP-TOFMS reference data can be observed for  $\text{Li}_2\text{O}$  and  $\text{Na}_2\text{O}$ . LIBS-based  $\text{Li}_2\text{O}$  concentrations of specific spodumene crystals (areas with high  $\text{Li}_2\text{O}$  concentrations) are underestimated by 0.8 – 1.0 wt.%. Main reason are the particularly high  $\text{Li}_2\text{O}$  values of these spodumene crystals in sample BK200. They show average LA-ICP-TOFMS

concentrations of 7.8 wt.%  $\text{Li}_2\text{O}$ , whereas the spodumene minerals of the reference sample BK203\_S12 display average LA-ICP-TOFMS values of 6.8 wt.%  $\text{Li}_2\text{O}$ . Similarly,  $\text{Na}_2\text{O}$  is underestimated by 1.0-2.0 wt.% in several albite crystals (areas with high  $\text{Na}_2\text{O}$  concentrations). LA-ICP-TOFMS  $\text{Na}_2\text{O}$  values of albite crystals in reference sample BK203\_S12 average at 11.0 wt.%, whereas  $\text{Na}_2\text{O}$  concentrations of albite minerals in the measured area of sample BK200 average at 12.0 wt.%. Since the non-linear LS-SVM function models new concentrations very close to its trained concentration range (Valyon and Horváth, 2005), LIBS-based concentrations of  $\text{Li}_2\text{O}$  and  $\text{Na}_2\text{O}$  are slightly underestimated in the affected spodumene and albite crystals of sample BK200.

Although the large K-feldspar crystal in the upper right corner (area with high  $\text{K}_2\text{O}$  concentrations) shows elevated LIBS-based  $\text{K}_2\text{O}$  concentrations averaging at 10.4 wt.%, LA-ICP-TOFMS measurements of the same crystal display average  $\text{K}_2\text{O}$  values of 14.5 wt.%. Inspecting the corresponding LIBS spectra revealed a saturation for K I 766.49 nm and K I 769.90 nm in BK200 and the additional reference area, which was not observed for spectra of spodumene, albite, quartz or muscovite. Since saturation can affect the LIBS-based quantification accuracy (Takahashi and Thornton, 2017), this is likely the reason for the underestimated  $\text{K}_2\text{O}$  concentrations of the K-feldspar crystal. No other reliable K lines are present in the spectral range covered by our spectrometer and, therefore, special attention is required for LIBS instrumentation and experimental set-up in order to obtain spectra with high signal-to-noise ratios on all relevant lines but no saturation on the K target emission lines for all minerals present in pegmatitic samples. Nevertheless, LIBS-based  $\text{K}_2\text{O}$  concentrations of BK203\_S12b show that the developed quantification model is reliable for concentrations of up to 9.0 wt.% (Figure 6).

The developed multivariate quantification approach can therefore be applied onto drill core samples of the same deposit for  $\text{Li}_2\text{O}$ ,  $\text{SiO}_2$ ,  $\text{Al}_2\text{O}_3$ ,  $\text{Na}_2\text{O}$ , as well as areas with  $\text{K}_2\text{O}$  concentrations up to at least 9.0 wt.%. Multivariate calibration successfully overcomes severe physical matrix effects in crystals of pure minerals and chemical matrix effects between different minerals with one calibration model. The multivariate approach facilitates the description of the multidimensional nature of the data (i.e. the different minerals), as well as the collinearity in the LIBS data. The resulting function recognizes each mineral based on its normalised LIBS intensities and converts the intensities 'mineral specific' into element concentrations.

## 4.4 Conclusion

This paper demonstrates the use of LA-ICP-TOFMS to calibrate LIBS to obtain quantified, spatially resolved maps of Li and other major rock forming elements for heterogeneous spodumene pegmatites showing severe matrix effects. Based on a pixel-matched reference sample a multivariate calibration model can be trained that recognizes different types of minerals which show a large variety of matrix effects. The developed model is able to apply a calibration function on normalised LIBS intensity data to convert these data into element concentrations for heterogeneous spodumene pegmatite drill core samples.

Investigating the number of training pixel necessary to achieve good results with the pixel-matched approach showed increasing accuracies with an increasing number of training pixel. Good results were already obtained with 500 train pixel, and only minor changes were observed with more than 1000 pixel used for training. The non-linear LS-SVM algorithm outperforms the PLSR approach for the calibration model in terms of model accuracy, which is reflected in the RMSE and  $R^2$  values.

The developed LIBS calibration approach was successfully validated by applying it on an adjacent test area of the reference sample and on an independent spodumene pegmatite sample from another part of the drill core. Representative samples of the target deposit are needed for the multivariate calibration approach, which should cover all target minerals, their concentrations ranges and physical



and chemical matrix effects. However, the calibration model can easily be extended by including additional pixel-matched reference samples if new matrices (minerals) occur in the target material, e.g. during an exploration campaign.

Combining LA-ICP-TOFMS with LIBS enables the creation of a pixel-matched quantification model that allows fast and accurate spatial quantification of Li and other major rock forming elements in heterogeneous geological samples. The developed method provides a LIBS-based quantitative drill core scanner application for pegmatitic material.

## Acknowledgements

We thank Dr. Pentti Grönholm from Keliber Oy for providing the drill core material. We thank Dieter Rammelmair (BGR) for the mineralogical discussions, as well as Lutz Pfeifer and Sven Merk (both LTB Lasertechnik Berlin) for fruitful discussions on the LIBS technology. Furthermore, we thank Dominic Göricke (BGR) and Christopher Specht (BGR) for their support with the LIBS measurements and the T-REX consortium for the regular exchange.

## Funding

This work was funded by EIT RawMaterials (Grant Nr. 19122); the Federal Ministry for Economic Affairs and Energy (Grant Nr. ZF4441001SA7); the BGR research project RoStraMet

## References

- Ahtola, T., 2015. Overview of lithium pegmatite exploration in the Kaustinen area in 2003–2012 30.
- Anderson, R.B., Clegg, S.M., Frydenvang, J., Wiens, R.C., McLennan, S., Morris, R.V., Ehlmann, B., Dyar, M.D., 2017. Improved accuracy in quantitative laser-induced breakdown spectroscopy using sub-models. *Spectrochimica Acta Part B: Atomic Spectroscopy* 129, 49–57. <https://doi.org/10.1016/j.sab.2016.12.002>
- Anderson, R.B., Morris, R.V., Clegg, S.M., Bell, J.F., Wiens, R.C., Humphries, S.D., Mertzman, S.A., Graff, T.G., McInroy, R., 2011. The influence of multivariate analysis methods and target grain size on the accuracy of remote quantitative chemical analysis of rocks using laser induced breakdown spectroscopy. *Icarus* 215, 608–627. <https://doi.org/10.1016/j.icarus.2011.07.034>
- Bolger, J.A., 2000. Semi-quantitative Laser-Induced Breakdown Spectroscopy for Analysis of Mineral Drill Core. *Applied Spectroscopy* 54, 181–189.
- Burger, M., Gundlach-Graham, A., Allner, S., Schwarz, G., Wang, H.A.O., Gyr, L., Burgener, S., Hattendorf, B., Grolimund, D., Günther, D., 2015. High-Speed, High-Resolution, Multielemental LA-ICP-TOFMS Imaging: Part II. Critical Evaluation of Quantitative Three-Dimensional Imaging of Major, Minor, and Trace Elements in Geological Samples. *Anal. Chem.* 87, 8259–8267. <https://doi.org/10.1021/acs.analchem.5b01977>
- Chew, D., Drost, K., Marsh, J.H., Petrus, J.A., 2021. LA-ICP-MS imaging in the geosciences and its applications to geochronology. *Chemical Geology* 559, 119917. <https://doi.org/10.1016/j.chemgeo.2020.119917>
- Chirinos, J.R., Oropeza, D.D., Gonzalez, J.J., Hou, H., Morey, M., Zorba, V., Russo, R.E., 2014. Simultaneous 3-dimensional elemental imaging with LIBS and LA-ICP-MS. *J. Anal. At. Spectrom.* 29, 1292–1298. <https://doi.org/10.1039/C4JA00066H>
- Clegg, S.M., Sklute, E., Dyar, M.D., Barefield, J.E., Wiens, R.C., 2009. Multivariate analysis of remote laser-induced breakdown spectroscopy spectra using partial least squares, principal component analysis, and related techniques. *Spectrochimica Acta Part B: Atomic Spectroscopy* 64, 79–88. <https://doi.org/10.1016/j.sab.2008.10.045>

- Cremers, D., Radziemski, L., 2013. Handbook of Laser-Induced Breakdown Spectroscopy: Second Edition. Handbook of Laser-Induced Breakdown Spectroscopy: Second Edition. <https://doi.org/10.1002/9781118567371>
- El Haddad, J., de Lima Filho, E.S., Vanier, F., Harhira, A., Padioleau, C., Sabsabi, M., Wilkie, G., Blouin, A., 2019. Multiphase mineral identification and quantification by laser-induced breakdown spectroscopy. Minerals Engineering 134, 281–290. <https://doi.org/10.1016/j.mineng.2019.02.025>
- Fabre, C., Boiron, M.-C., Dubessy, J., Chabiron, A., Charoy, B., Martin Crespo, T., 2002. Advances in lithium analysis in solids by means of laser-induced breakdown spectroscopy: an exploratory study. Geochimica et Cosmochimica Acta 66, 1401–1407. [https://doi.org/10.1016/S0016-7037\(01\)00858-4](https://doi.org/10.1016/S0016-7037(01)00858-4)
- Fabre, C., Ourti, N.E., Ballouard, C., Mercadier, J., Cauzid, J., 2022. Handheld LIBS analysis for in situ quantification of Li and detection of the trace elements (Be, Rb and Cs). Journal of Geochemical Exploration 236, 106979. <https://doi.org/10.1016/j.gexplo.2022.106979>
- Haavisto, O., Kauppinen, T., Häkkänen, H., 2013. Laser-Induced Breakdown Spectroscopy for Rapid Elemental Analysis of Drillcore. IFAC Proceedings Volumes 46, 87–91. <https://doi.org/10.3182/20130825-4-US-2038.00047>
- Hahn, D.W., Omenetto, N., 2012. Laser-Induced Breakdown Spectroscopy (LIBS), Part II: Review of Instrumental and Methodological Approaches to Material Analysis and Applications to Different Fields. Applied Spectroscopy 66, 347–419. <https://doi.org/10.1366/11-06574>
- Harmon, R.S., Senesi, G.S., 2021. Laser-Induced Breakdown Spectroscopy – A geochemical tool for the 21st century. Applied Geochemistry 128, 104929. <https://doi.org/10.1016/j.apgeochem.2021.104929>
- Hoekzema, N.M., Rutten, R.J., Brandt, P.N., Shine, R.A., 1998. Small-scale topology of solar atmosphere dynamics I. Wave sources and wave diffraction. Astronomy and Astrophysics 329, 276–290.
- Janovszky, P., Jancsek, K., Palásti, D.J., Kopniczky, J., Hopp, B., M. Tóth, T., Galbács, G., 2021. Classification of minerals and the assessment of lithium and beryllium content in granitoid rocks by laser-induced breakdown spectroscopy. J. Anal. At. Spectrom. 36, 813–823. <https://doi.org/10.1039/D1JA00032B>
- Kennard, R.W., Stone, L.A., 1969. Computer Aided Design of Experiments. null 11, 137–148. <https://doi.org/10.1080/00401706.1969.10490666>
- Kesler, S.E., Gruber, P.W., Medina, P.A., Keoleian, G.A., Everson, M.P., Wallington, T.J., 2012. Global lithium resources: Relative importance of pegmatite, brine and other deposits. Ore Geology Reviews 48, 55–69. <https://doi.org/10.1016/j.oregeorev.2012.05.006>
- Khajehzadeh, N., Haavisto, O., Koresaar, L., 2016. On-stream and quantitative mineral identification of tailing slurries using LIBS technique. Minerals Engineering 98, 101–109. <https://doi.org/10.1016/j.mineng.2016.08.002>
- Kuhn, K., Meima, J.A., Rammlmair, D., Ohlendorf, C., 2016. Chemical mapping of mine waste drill cores with laser-induced breakdown spectroscopy (LIBS) and energy dispersive X-ray fluorescence (EDXRF) for mineral resource exploration. Journal of Geochemical Exploration 161, 72–84. <https://doi.org/10.1016/j.gexplo.2015.11.005>
- Kushnir, D., Sandén, B.A., 2012. The time dimension and lithium resource constraints for electric vehicles. Resources Policy 37, 93–103. <https://doi.org/10.1016/j.resourpol.2011.11.003>
- Kuusela, J., Ahtola, T., Koistinen, E., Seppänen, H., Hatakka, T., Lohva, J., 2011. Report of investigations on the Rapasaaret lithium pegmatite deposit in Kaustinen-Kokkola, Western Finland 65.

- Martin, G., Rentsch, L., Höck, M., Bertau, M., 2017. Lithium market research – global supply, future demand and price development. *Energy Storage Materials* 6, 171–179. <https://doi.org/10.1016/j.ensm.2016.11.004>
- Maxwell, P., 2014. Analysing the lithium industry: Demand, supply, and emerging developments. *Miner Econ* 26, 97–106. <https://doi.org/10.1007/s13563-013-0041-5>
- Meima, J.A., Rammlmair, D., 2020. Investigation of compositional variations in chromitite ore with imaging Laser Induced Breakdown Spectroscopy and Spectral Angle Mapper classification algorithm. *Chemical Geology* 532, 119376. <https://doi.org/10.1016/j.chemgeo.2019.119376>
- Meima, J.A., Rammlmair, D., Junge, M., 2022. The use of Laser Induced Breakdown Spectroscopy for the mineral chemistry of chromite, orthopyroxene and plagioclase from Merensky Reef and UG-2 chromitite, Bushveld Complex, South Africa. *Chemical Geology* 589, 120686. <https://doi.org/10.1016/j.chemgeo.2021.120686>
- Mevik, B.-H., Wehrens, R., 2021. Introduction to the pls Package.
- Müller, S., Meima, J.A., 2022. Mineral classification of lithium-bearing pegmatites based on laser-induced breakdown spectroscopy: Application of semi-supervised learning to detect known minerals and unknown material. *Spectrochimica Acta Part B: Atomic Spectroscopy* 189, 106370. <https://doi.org/10.1016/j.sab.2022.106370>
- Müller, S., Meima, J.A., Rammlmair, D., 2021. Detecting REE-rich areas in heterogeneous drill cores from Storkwitz using LIBS and a combination of k-means clustering and spatial raster analysis. *Journal of Geochemical Exploration* 221, 106697. <https://doi.org/10.1016/j.gexplo.2020.106697>
- Neff, C., Keresztes Schmidt, P., Garofalo, P.S., Schwarz, G., Günther, D., 2020. Capabilities of automated LA-ICP-TOFMS imaging of geological samples. *J. Anal. At. Spectrom.* 35, 2255–2266. <https://doi.org/10.1039/D0JA00238K>
- Novotný, K., Kaiser, J., Galiová, M., Konečná, V., Novotný, J., Malina, R., Liška, M., Kanický, V., Otruba, V., 2008. Mapping of different structures on large area of granite sample using laser-ablation based analytical techniques, an exploratory study. *Spectrochimica Acta Part B: Atomic Spectroscopy* 63, 1139–1144. <https://doi.org/10.1016/j.sab.2008.06.011>
- Pagnotta, S., Lezzerini, M., Campanella, B., Legnaioli, S., Poggialini, F., Palleschi, V., 2020. A new approach to non-linear multivariate calibration in laser-induced breakdown spectroscopy analysis of silicate rocks. *Spectrochimica Acta Part B: Atomic Spectroscopy* 166, 105804. <https://doi.org/10.1016/j.sab.2020.105804>
- R Core Team, 2018. R: A Language and Environment for Statistical Computing. R Foundation for Statistical Computing, Vienna, Austria.
- Rammelkamp, K., Schröder, S., Ortenzi, G., Pisello, A., Stephan, K., Baqué, M., Hübers, H.-W., Forni, O., Sohl, F., Thomsen, L., Unnithan, V., 2021. Field investigation of volcanic deposits on Vulcano, Italy using a handheld laser-induced breakdown spectroscopy instrument. *Spectrochimica Acta Part B: Atomic Spectroscopy* 177, 106067. <https://doi.org/10.1016/j.sab.2021.106067>
- Rasilainen, K., Eilu, P., Ahtola, T., Halkoaho, T., Kärkkäinen, N., Kuusela, J., Lintinen, P., Törmänen, T., 2018. Quantitative assessment of undiscovered resources in lithium–caesium–tantalum pegmatite-hosted deposits in Finland, 406th ed. Geological Survey of Finland, FI.
- Reed, S.J.B., 2005. *Electron Microprobe Analysis and Scanning Electron Microscopy in Geology*, 2nd ed. Cambridge University Press, Cambridge. <https://doi.org/10.1017/CBO9780511610561>
- Rethfeldt, N., Brinkmann, P., Riebe, D., Beitz, T., Köllner, N., Altenberger, U., Löhmannsröben, H.-G., 2021. Detection of Rare Earth Elements in Minerals and Soils by Laser-Induced Breakdown

- Spectroscopy (LIBS) Using Interval PLS. *Minerals* 11, 1379. <https://doi.org/10.3390/min11121379>
- Rifai, K., Constantin, M., Yilmaz, A., Özcan, L.Ç., Doucet, F.R., Azami, N., 2022. Quantification of Lithium and Mineralogical Mapping in Crushed Ore Samples Using Laser Induced Breakdown Spectroscopy. *Minerals* 12, 253. <https://doi.org/10.3390/min12020253>
- Rifai, K., Doucet, F., Özcan, L., Vidal, F., 2018. LIBS core imaging at kHz speed: Paving the way for real-time geochemical applications. *Spectrochimica Acta Part B: Atomic Spectroscopy* 150, 43–48. <https://doi.org/10.1016/j.sab.2018.10.007>
- Romppanen, S., Pölönen, I., Häkkänen, H., Kaski, S., 2021. Optimization of spodumene identification by statistical approach for laser-induced breakdown spectroscopy data of lithium pegmatite ores. null 1–21. <https://doi.org/10.1080/05704928.2021.1963977>
- Rubatto, D., Burger, M., Lanari, P., Hattendorf, B., Schwarz, G., Neff, C., Keresztes Schmidt, P., Hermann, J., Vho, A., Günther, D., 2020. Identification of growth mechanisms in metamorphic garnet by high-resolution trace element mapping with LA-ICP-TOFMS. *Contrib Mineral Petrol* 175, 61. <https://doi.org/10.1007/s00410-020-01700-5>
- Stanković, S., Martin, M., Goldmann, S., Gäbler, H.-E., Ufer, K., Haubrich, F., Moutinho, V.F., Giese, E.C., Neumann, R., Stropper, J.L., Stummeyer, J., Kaufhold, S., Dohrmann, R., Oxley, A., Marbler, H., Schippers, A., 2022. Effect of mineralogy on Co and Ni extraction from Brazilian limonitic laterites via bioleaching and chemical leaching. *Minerals Engineering* 184, 107604. <https://doi.org/10.1016/j.mineng.2022.107604>
- Steinwart, I., Thomann, P., 2017. liquidSVM: A Fast and Versatile SVM package. ArXiv e-prints 1702.06899.
- Stevens, A., Ramirez-Lopez, L., 2020. An Introduction to the prospectr package.
- Suykens, J.A.K., Vandewalle, J., 1999. Least Squares Support Vector Machine Classifiers. *Neural Processing Letters* 9, 293–300. <https://doi.org/10.1023/A:1018628609742>
- Sweetapple, M.T., Tassios, S., 2015. Laser-induced breakdown spectroscopy (LIBS) as a tool for in situ mapping and textural interpretation of lithium in pegmatite minerals. *American Mineralogist* 100, 2141–2151. <https://doi.org/10.2138/am-2015-5165>
- Takahashi, T., Thornton, B., 2017. Quantitative methods for compensation of matrix effects and self-absorption in Laser Induced Breakdown Spectroscopy signals of solids. *Spectrochimica Acta Part B: Atomic Spectroscopy* 138, 31–42. <https://doi.org/10.1016/j.sab.2017.09.010>
- Tucker, J.M., Dyar, M.D., Schaefer, M.W., Clegg, S.M., Wiens, R.C., 2010. Optimization of laser-induced breakdown spectroscopy for rapid geochemical analysis. *Chemical Geology* 277, 137–148. <https://doi.org/10.1016/j.chemgeo.2010.07.016>
- Ubide, T., Caulfield, J., Brandt, C., Bussweiler, Y., Mollo, S., Di Stefano, F., Nazzari, M., Scarlato, P., 2019. Deep Magma Storage Revealed by Multi-Method Elemental Mapping of Clinopyroxene Megacrysts at Stromboli Volcano. *Frontiers in Earth Science* 7. <https://doi.org/10.3389/feart.2019.00239>
- Valyon, J., Horváth, G., 2005. A Robust LS-SVM Regression, in: Ardil, C. (Ed.), International Enformatika Conference, IEC'05, August 26-28, 2005, Prague, Czech Republic, CDROM. Enformatika, Çanakkale, Turkey, pp. 148–153.
- Wise, M.A., Harmon, R.S., Curry, A., Jennings, M., Grimaç, Z., Khashchevskaya, D., 2022. Handheld LIBS for Li Exploration: An Example from the Carolina Tin-Spodumene Belt, USA. *Minerals* 12, 77. <https://doi.org/10.3390/min12010077>

- Wold, S., Sjöström, M., Eriksson, L., 2001. PLS-regression: a basic tool of chemometrics. *Chemometrics and Intelligent Laboratory Systems* 58, 109–130. [https://doi.org/10.1016/S0169-7439\(01\)00155-1](https://doi.org/10.1016/S0169-7439(01)00155-1)
- Xu, C., Dai, Q., Gaines, L., Hu, M., Tukker, A., Steubing, B., 2020. Future material demand for automotive lithium-based batteries. *Commun Mater* 1, 99. <https://doi.org/10.1038/s43246-020-00095-x>
- Ytsma, C.R., Dyar, M.D., 2019. Accuracies of lithium, boron, carbon, and sulfur quantification in geological samples with laser-induced breakdown spectroscopy in Mars, Earth, and vacuum conditions. *Spectrochimica Acta Part B: Atomic Spectroscopy* 162, 105715. <https://doi.org/10.1016/j.sab.2019.105715>



## 5. Summary and Outlook

### 5.1 Developed applications and their combination

The presented publications extend the existing applications of LIBS in geology by spatially detailed LIBS measurements of highly heterogeneous drill core samples of different deposits. Each application addresses an important aspect of the spatial analysis of heterogeneous LIBS measurements, although especially the wide variety of physical and chemical matrix effects are of specific importance in every investigated application. Due to the large number of existing minerals, matrix effects are always present in large geological mappings of heterogeneous material, preventing the straightforward analysis of LIBS drill core measurements.

The minimization of matrix effects is explained in detail for brecciated material with mineral crystals smaller than the laser spot size (chapter 2), as well as pegmatitic material with large minerals up to 10 cm in size (chapter 3 and 4). A variety of different machine learning algorithms and chemometric methods were applied to overcome these matrix effects, and LIBS could be used for spatially resolved detection of REE enrichments in brecciated carbonatite, as well as mineral classification and pixel specific quantification of Li and other major rock forming elements in spodumene pegmatite.

Chapter 2 describes the use of k-means clustering and image analysis to establish instrument specific intensity limit for La, which can be used to detect areas enriched in REEs in spatially detailed LIBS mappings. The intensity limit was used to find all pixels with high La contents, and, based on this information, REE concentrations were estimated by using electron microprobe information of distinct REE minerals of the same deposit as a reference.

A novel classification algorithm was developed in chapter 3, which allows the classification of minerals and the detection of unknown LIBS spectra that are not covered by the train set. These spectra either belong to macro porosities, new minerals, or mineral borders, indicating a new LIBS matrix that needs further investigation. This is especially important for spatially resolved LIBS analysis of drill cores, where the occurrence of new minerals is common.

Chapter 4 describes the preparation of matrix-matched reference samples for pixel-specific quantification. These samples are mapped with LA-ICP-TOFMS as well as LIBS, before both data sets are matched pixel-by-pixel and used to train a LS-SVM quantification model that is able to convert LIBS intensities into element concentrations. This allows pixel-specific quantification of LIBS mappings of Li-bearing drill core samples.

While every chapter itself covers different applications and methodologies, the developed algorithms can be combined to enable a workflow that allows a classification of minerals, the identification of new minerals not covered by the train set, the selection of mineral borders, and the pixel specific quantification of all minerals that are covered by a pixel-matched reference sample.

LIBS-based quantification and classification of geological samples are only possible for minerals that are also covered by reference samples, and both can be especially problematic for measurement points at mineral borders. The developed classification algorithm (chapter 3) is able to identify minerals that are not present in a reference sample, and the combination of cluster- and image analysis presented in chapter 2 can be employed to detect mineral borders automatically. By combining these

methods, problematic LIBS spectra can be identified, and only trustworthy quantification and classification results are provided.

## 5.2 Instrument specific challenges

Employing LIBS based drill core scanners for the investigation of complete drill holes can drastically reduce the time of geochemical analysis, displaying highly detailed information of large samples or even complete drill core meters rapidly. The drill core scanner that was used for the measurements presented in this work was still at a prototype level, and therefore revealed different instrument specific challenges with room for improvement:

- 1) Laser spot size. The REE bearing minerals of the brecciated carbonatite showed high concentrations of Ce and Nd, but no emission could be detected with the instrument used. Under atmospheric conditions, their detection with LIBS is generally difficult (Bhatt et al., 2018; Gaft et al., 2019), and since the REE-bearing minerals in the brecciated rock matrix were significantly smaller than the laser spot size, the elemental information measured with LIBS displayed a mixture of REE-bearing- and other minerals of the rocks matrix. Therefore, the concentrations of Ce and Nd were diluted by the surrounding material, which increased the difficulty to accurately detect them even further. Using a smaller laser spot size would have increased the concentrations of Ce and Nd in the resulting spectrum, and, as a result, both elements might have become detectable. Although, the emission lines of Li are very sensitive (Fabre, 2020), the LIBS-based quantification of spodumene pegmatite revealed difficulties to predict concentrations at mineral transition zones. These transition zones could be minimized by using a smaller laser spot size, and, therefore, this could also be advantageous for the analysis of pegmatitic ore.
- 2) Measurement time. Smaller laser spot sizes lead to higher resolutions, and, in turn, more shots are needed to cover the same area of the sample. Especially the measurement of large surfaces in high resolution can easily include over a million single measurement points (Nardecchia et al., 2020). This increases the measurement time accordingly, and while a spectrum itself is formed and detected in micro-seconds, saving the data can take significantly longer. With the drill core scanner prototype used in this work, a scan speed of roughly 1 measurement per second could not be exceeded.
- 3) Spatial restrictions. The drill core scanner prototype allowed consecutive measurements of up to 2.5 cm in Y-direction. Larger samples had to be moved by hand parallel to the stage, leaving a potential risk to produce man-made offsets in mappings of samples broader than 2.5 cm. Although this problem can be minimized through precise movements of the sample, small offsets were difficult to avoid and therefore not uncommon.
- 4) Spectral comparability. Due to the extensive throughput, different parts of the LIBS instrument had to be replaced at some point during the work on this thesis. It was therefore essential to monitor the comparability of the LIBS spectra taken from similar material but at different times frequently. Thereto, a monitoring system was developed, which ensured comparable spectra and enabled a reliable classification and quantification throughout each measuring campaign.

The successor of the drill core scanner prototype is already in use, and the aforementioned challenges have been solved. It has a highly increased scanning speed, no significant spatial restriction in the Y-direction, and a smaller laser spot size. Additionally, the durability of all components is increased.

### 5.3 Software and algorithm specific challenges

Different software and various machine learning models were essential to quickly analyse the large amount of data that was acquired in a short amount of time. Thereby, different algorithm specific challenges were observed:

- 1) Semi-supervised learning. Incomplete trainsets for quantification and classification can lead to wrong predictions of element concentrations or mineral labels. This problem became especially apparent while working with highly heterogeneous drill core material from different deposits. Chapter 3 displays one example on how to solve this problem. The developed workflow is based on semi-supervised learning, which is an emerging field in machine learning. Although it is already used in other geoscientific communities like remote sensing (e.g. Tan et al., 2014), room for improvement still exists, and new and potentially more effective algorithms may emerge in the future.
- 2) Image registration. Pixel-specific quantifications of complex geological material are still difficult with LIBS due to the severe matrix effects observed in heterogeneous samples. Therefore, many publications could only provide semi-quantitative analysis for LIBS mappings and drill core samples (e.g. J. A. Bolger, 2000; Lefebvre et al., 2016; Sweetapple and Tassios, 2015). In chapter 4, the use of a pixel-matched reference sample allows pixel-specific predictions with high accuracy. The necessary image registration of LA-ICP-TOFMS reference data and LIBS measurements had to be done by hand, which can be time consuming if many reference samples are necessary. Future developments will probably provide easy applications of already existing algorithms that are able to pixel-match datasets measured with different instruments, different angles, and different resolution automatically. This would reduce time and could potentially further enhance accuracy of the following quantification.
- 3) Necessary resolution of the reference data. To pixel-match the LA-ICP-TOFMS measurements in chapter 4 with LIBS, the data had to be rescaled to match the LIBS resolution. This was done using the median value and depending on the spot size of the LA-ICP-TOFMS measurement, between 100 and 400 single points were considered during this process. Since only a single value was used to produce the rescaled image, fewer measurement points could have yielded an identical result. Especially for material with large mineral crystals, a larger distance between each measurement line and/or row is potentially sufficient, reducing the LA-ICP-TOFMS measurement time drastically.
- 4) Spectral comparability. The spectral comparability of different LIBS instruments and settings is difficult because the detected spectral response depends on the deployed hardware (laser-, detector- or spectrometer-type), as well as their individual measurement settings. Nevertheless, future research might provide algorithmic solutions for this problem. If measurements performed with different settings, different instruments and on different material are comparable, an expandable mineral database could be created. This database could then be used to classify newly measured geological samples across different LIBS instruments.

The world of machine learning is evolving fast, and it is difficult to keep up with the different developments that are made day by day. It is therefore important to monitor potential improvements concerning data fusion, data assimilation and transfer learning regularly.

### 5.4 Future potential of LIBS for geological applications

This thesis highlights the potential of LIBS to measure and analyse high-resolution mappings of large geological drill core samples. Additionally, drill core scanners can also be employed for single profile

measurements of complete drill core meters (Kuhn and Meima, 2019; Meima et al., 2022), which is significantly faster than spatially detailed 2D-measurements. By analysing complete drill holes with multiple profiles in a short amount of time – potentially even in-situ on the mining site – important geochemical information can be revealed to the prospectors in real time. Based on this information, promising areas for the spatially detailed but also more time-consuming LIBS analysis can be selected.

The increasing success of LIBS as an analytical tool for a variety of geological applications in the last two decades is undeniable and reflected in the increasing number of publications. Nevertheless, LIBS is still unknown to many geoscientific researchers and mining companies, and, as a result, often ignored in favour of more established techniques. A continuously growing number of relevant geological publications that are based on LIBS can attract the attention of a larger audience. Enormous improvements in laser, spectrometer and detector quality, size and costs have already been made, and this trend will most likely continue in the future. Similarly, computational power is expected to increase as well, and new machine learning models are developed constantly. With updated hard- and software, the many advantages of LIBS could increase its popularity in analytical geology.

Irrespective of future development, LIBS cannot be used to solve every geoscientific problem. Luckily, it is possible to combine LIBS with a variety of analytical instruments. It is especially easy to combine LIBS with other laser-dependant techniques, e.g. Raman or LA-ICP-(TOF)MS, and a number of publications already exist for various applications in- and outside the field of geology (e.g. Chirinos et al., 2014; Dong et al., 2020; Shameem et al., 2017). First multi-sensor systems are planned, and it is likely that new multi-sensor core logging systems will include LIBS and see increasing use in the field of geological exploration and mining in the future. This might lead to the establishment of benchmark datasets that can improve mineral classification or LIBS-based quantification.

The extensive work with LIBS that was performed during this work underlined its great potential for various geological applications. I sincerely hope that the published articles demonstrate some of the many advantages and possibilities of LIBS and thereby help to establish LIBS-based analytics in geochemistry.

## References

- Bhatt, C.R., Jain, J.C., Goueguel, C.L., McIntyre, D.L., Singh, J.P., 2018. Determination of Rare Earth Elements in Geological Samples Using Laser-Induced Breakdown Spectroscopy (LIBS). *Appl Spectrosc* 72, 114–121. <https://doi.org/10.1177/0003702817734854>
- Bolger, J.A., 2000. Semi-Quantitative Laser-Induced Breakdown Spectroscopy for Analysis of Mineral Drill Core. *Appl Spectrosc* 54, 181–189. <https://doi.org/10.1366/0003702001949375>
- Chirinos, J.R., Oropeza, D.D., Gonzalez, J.J., Hou, H., Morey, M., Zorba, V., Russo, R.E., 2014. Simultaneous 3-dimensional elemental imaging with LIBS and LA-ICP-MS. *J. Anal. At. Spectrom.* 29, 1292–1298. <https://doi.org/10.1039/C4JA00066H>
- Dong, M., Wei, L., González, J.J., Oropeza, D., Chirinos, J., Mao, X., Lu, J., Russo, R.E., 2020. Coal Discrimination Analysis Using Tandem Laser-Induced Breakdown Spectroscopy and Laser Ablation Inductively Coupled Plasma Time-of-Flight Mass Spectrometry. *Anal. Chem.* 92, 7003–7010. <https://doi.org/10.1021/acs.analchem.0c00188>

Fabre, C., 2020. Advances in Laser-Induced Breakdown Spectroscopy analysis for geology: A critical review. *Spectrochimica Acta Part B: Atomic Spectroscopy* 166, 105799. <https://doi.org/10.1016/j.sab.2020.105799>

Gaft, M., Raichlin, Y., Pelascini, F., Panzer, G., Motto Ros, V., 2019. Imaging rare-earth elements in minerals by laser-induced plasma spectroscopy: Molecular emission and plasma-induced luminescence. *Spectrochimica Acta Part B: Atomic Spectroscopy* 151, 12–19. <https://doi.org/10.1016/j.sab.2018.11.003>

Kuhn, K., Meima, J.A., 2019. Characterization and Economic Potential of Historic Tailings from Gravity Separation: Implications from a Mine Waste Dump (Pb-Ag) in the Harz Mountains Mining District, Germany. *Minerals* 9, 303. <https://doi.org/10.3390/min9050303>

Lefebvre, C., Catalá-Espí, A., Sobron, P., Koujelev, A., Léveillé, R., 2016. Depth-resolved chemical mapping of rock coatings using Laser-Induced Breakdown Spectroscopy: Implications for geochemical investigations on Mars. *Planetary and Space Science* 126, 24–33. <https://doi.org/10.1016/j.pss.2016.04.003>

Meima, J.A., Rammlmair, D., Junge, M., 2022. The use of Laser Induced Breakdown Spectroscopy for the mineral chemistry of chromite, orthopyroxene and plagioclase from Merensky Reef and UG-2 chromitite, Bushveld Complex, South Africa. *Chemical Geology* 589, 120686. <https://doi.org/10.1016/j.chemgeo.2021.120686>

Nardecchia, A., Fabre, C., Cauzid, J., Pelascini, F., Motto-Ros, V., Duponchel, L., 2020. Detection of minor compounds in complex mineral samples from millions of spectra: A new data analysis strategy in LIBS imaging. *Analytica Chimica Acta* 1114, 66–73. <https://doi.org/10.1016/j.aca.2020.04.005>

Shameem, K.M.M., Choudhari, K.S., Bankapur, A., Kulkarni, S.D., Unnikrishnan, V.K., George, S.D., Kartha, V.B., Santhosh, C., 2017. A hybrid LIBS–Raman system combined with chemometrics: an efficient tool for plastic identification and sorting. *Anal Bioanal Chem* 409, 3299–3308. <https://doi.org/10.1007/s00216-017-0268-z>

Sweetapple, M.T., Tassios, S., 2015. Laser-induced breakdown spectroscopy (LIBS) as a tool for in situ mapping and textural interpretation of lithium in pegmatite minerals. *American Mineralogist* 100, 2141–2151. <https://doi.org/10.2138/am-2015-5165>

Tan, K., Li, E., Du, Q., Du, P., 2014. An efficient semi-supervised classification approach for hyperspectral imagery. *ISPRS Journal of Photogrammetry and Remote Sensing* 97, 36–45. <https://doi.org/10.1016/j.isprsjprs.2014.08.003>



# Curriculum Vitae

Name: Simon Müller  
Geburtstag: 23.02.1993  
Geburtsort: Moosburg a.d. Isar  
Staatsangehörigkeit: Deutsch

07/2011 **Abitur**  
Karl-Ritter-von-Frisch Gymnasium Moosburg

10/2012 - 07/2015 **Bachelor of Science: Geowissenschaften**  
Friedrich-Alexander-Universität Erlangen-Nürnberg

10/2015 – 03/2018 **Master of Science: Geowissenschaften**  
Friedrich-Alexander-Universität Erlangen-Nürnberg

07/2018 – 10/2021 **Wissenschaftlicher Mitarbeiter: Projekt GeoLIBScanner**  
Bundesanstalt für Geowissenschaften und Rohstoffe

11/2021 – 10/2022 **Wissenschaftlicher Mitarbeiter: Projekt T-REX**  
Bundesanstalt für Geowissenschaften und Rohstoffe

08/2021 – 05/2023 **Promotionsstudent**  
Leibniz Universität Hannover

## Publications

### Peer-Reviewed Paper

**Müller, S.**, Meima, J.A., Gäbler, H-E., 2023. Improving spatially-resolved Lithium quantification in drill core samples of spodumene pegmatite by using laser-induced breakdown spectroscopy and pixel-matched reference areas, *Journal of Geochemical Exploration* 250, 107235. <https://doi.org/10.1016/j.gexplo.2023.107235>.

**Müller, S.**, Meima, J.A., 2022. Mineral classification of lithium-bearing pegmatites based on laser-induced breakdown spectroscopy: Application of semi-supervised learning to detect known minerals and unknown material, *Spectrochimica Acta Part B: Atomic Spectroscopy*. <https://doi.org/10.1016/j.sab.2022.106370>.

**Müller, S.**, Meima, J.A., Rammlmair, D., 2021. Detecting REE-rich areas in heterogeneous drill cores from Storkwitz using LIBS and a combination of k-means clustering and spatial raster analysis, *Journal of Geochemical Exploration* 221, 106697. <https://doi.org/10.1016/j.gexplo.2020.106697>.

### Conference Contributions

**Müller, S.**, Meima, 2021. Large-scale quantification of Li in spodumene pegmatite using Laser Induced Breakdown Spectroscopy, GeoKarlsruhe, 19-24 September 2021, Karlsruhe, Germany, Virtual Conference.

**Müller, S.**, Meima, J., Havisto, J., Lindström, H., Uusitalo, S., Heilala, B., García-Piña, C., Bernabé, P., Grönholm, P., 2021. Lithium quantification in spodumene pegmatite drill cores from Finland using LIBS and other core scanning technologies, 3rd European Mineralogical Conference, 29 August - 02 September 2021, Warsaw, Polen, Virtual Conference.

**Müller, S.**, Meima, J., Rammlmair, D., 2020. Detecting REE-carbonates in heterogeneous drill cores from Storkwitz using LIBS and a combination of k-measn clustering and spatial raster analysis, 11th International Conference on Laser-Induced Breakdown Spectroscopy, 20-25 September 2020, Kyoto, Japan, Virtual Conference.

**Müller, S.**, Meima, J., Rammlmair, D., 2020. Einsatz von LIBS zur Erkennung von REE-reichen Abschnitten in Bohrkernen von Storkwitz – Eine neue Methode zur schnellen und räumlich detaillierten Analyse geologischer Proben, Jahressitzung des GDMB-Fachausschusses Lagerstätten /Rohstoffwirtschaft, 14. Mai 2020, Virtual Conference, Oral Presentation.

**Müller, S.**, Meima, J., Rammlmair, D. Künker, M., 2019. Using LIBS to detect REE-rich areas in Storkwitz drill cores: a new method for rapid and spatially detailed analysis of geological samples, GeoMünster, 22-25 September 2019, Münster, Germany, Oral Presentation.

**Müller, S.**, Meima, J., Rammlmair, D., Künker, M., 2019. Detection of REE rich areas in Storkwitz drillcores using LIBS and a combination of normalization, clustering and spatial raster analysis, 10th Euro-Mediterranean Symposium on Laser-Induced Breakdown Spectroscopy EMSLIBS 2019, 8-13 September 2019, Brno, Czech Republic, Oral Present